A dissertation submitted to the Graduate Program of Electrical and Electronics Engineering in partial fulfillment of the requirements for the degree of Doctor in Engineering with emphasis in Electronics Engineering

Physical principles of memory and logic devices based on nanostructured Dirac materials

By

Juan Manuel Marmolejo-Tejada, MS.

Advisor

Jaime Velasco-Medina, PhD. – Universidad del Valle, Cali, Colombia

Universidad del Valle

Faculty of Engineering

Cali, Colombia

2017

Acknowledgements

I thank God for showing me His love and faithfulness all the time. This work could not have been done without His uncountable blessings.

Moreover, I would like to express my special gratitude to Prof. Jaime Velasco-Medina and Prof. Branislav K. Nikolić for their invaluable advice and support during my studies. I have learnt a lot from them and really thank the opportunity of doing research together.

Thanks to Claudia Rentería, Duverney Corrales, Po-Hao Chang, Xianlei Cheng and Kapildeb Dolui for the insightful research discussions and help both in Cali and Delaware. Sharing office with you and sharing thoughts and experiences really made these years go by quickly and pleasantly.

Finally, thanks to my lovely wife Katherine Cifuentes and our family for all their love and patience during this time. All your sacrifices are really meaningful to me and I do not think I could have gone this far without your encouragement and support.

Contents

Abstract

During the las decades, the silicon-based semiconductor industry has enabled higher performance per cost of integrated circuits due to the ability of nearly doubling the amount of transistors per chip every two years, however, this has resulted in overheating issues and fundamental manufacturing problems that are very difficult to solve. Therefore, Dirac materials (DMs), such as graphene and topological insulators (TIs), are being extensively investigated as possible candidates for replacing silicon-channel devices in the next-generation integrated circuits, due to their attractive ultrahigh carrier mobility and possibility of quantum effects that may be useful for electronic applications. This requires to study the physical principles of such nanostructures to effectively predict the quantum transport behavior of possible devices. The aim of this work is to explore the physical properties of Dirac material-based nanostructures that could be used for novel memory and logic devices, by using tight-binding (TB) and density function theory (DFT) methods combined with the non-equilibrium function (NEGF) formulation.

Outline of the Thesis

The general background of the materials that could be used in nanoelectronic devices is introduced in chapter 1. Then, chapter 2 presents the NEGF tools that are required for performing charge and spin transport calculations, while chapter 3 reviews the different approaches found in the literature for traditional charge transport devices based on graphene channels, as the initial approach for possible succesors of traditional integrated circuits technologies. Finally, applications of the studied physical principles and simulation results are covered in the subsequent chapters, as follows:

1. **Spin Hall Effect and Nonlocal Resistance in Adatom-Decorated Graphene**

   Recent experiments reporting unexpectedly large spin Hall effect (SHE) in graphene decorated with adatoms have raised a fierce controversy. We apply numerically exact Kubo and Landauer-Büttiker formulas to realistic models of gold-decorated disordered graphene (including adatom clustering) to obtain the spin Hall conductivity and spin Hall angle, as well as the nonlocal resistance as a quantity accessible to experiments. Large spin Hall angles of ~ 0.1 are obtained at zero-temperature, but their dependence on adatom clustering differs from the pre-

dictions of semiclassical transport theories. Furthermore, we find multiple background contributions to the nonlocal resistance, some of which are unrelated to the SHE or any other spin-dependent origin, as well as a strong suppression of the SHE at room temperature. This motivates us to design a multiterminal graphene geometry which suppresses these background contributions and could, therefore, quantify the upper limit for spin current generation in two-dimensional materials.

2. **Valley Hall Effect and Nonlocal Resistance in gapped Graphene**

   The recent observation [1] of nonlocal resistance $R_{\rm NL}$ near the Dirac point (DP) of multiterminal graphene, aligned on a hexagonal boron nitride (hBN) substrate, has been interpreted as the consequence of topological valley Hall currents carried by the Fermi sea states just beneath the bulk gap E_g in the energy spectrum of graphene opened by the inversion symmetry breaking due to hBN. However, the valley Hall conductivity σ^v_{xy}, quantized inside E_g, is not directly measurable. Conversely, the Landauer-Büttiker formula, as the numerically exact approach to modeling of nonlocal transport measurements, yields $R_{\rm NL} \equiv 0$ near the DP for the same simplistic Hamiltonian of gapped graphene which generates $\sigma^v_{xy} \neq 0$. We combine *ab initio* with quantum transport calculations to demonstrate that graphene-on-hBN wires with zigzag edges host edge states near the DP that were previously missed in theories based on too simplistic Hamiltonians. Although such peculiar edge states, whose local density of states never vanishes in the bulk, exist also in isolated zigzag graphene wires, only in the presence of hBN their dispersion is modified to generate $R_{\rm NL} \neq 0$. Concurrently, they resolve the long-standing puzzle of why the highly insulating state of graphene on hBN is rarely observed. *Thus, we conclude that the observed $R_{\rm NL}$ is unrelated to any nontrivial topology of gapped Dirac spectra.*

3. **Tunneling anisotropic magnetoresistance in topological-insulator/metal interfaces**

   The control of recently observed spintronic effects [2, 3, 4, 5, 6, 7, 8, 9, 10, 11] in topological-insulator/ferromagnetic-metal (TI/FM) heterostructures is thwarted by the lack of understanding of band structure and spin texture around their interfaces. Here we combine density functional theory with Green's function techniques to obtain the spectral function at any plane passing through atoms of Bi_2Se_3 and Co or Cu layers comprising the interface. In contrast to widely assumed [12, 13] but thinly tested Dirac cone gapped by the proximity exchange field spectral function, we find that the Rashba ferromagnetic model describes the spectral function on the surface of Bi_2Se_3 in contact with Co near the Fermi level E_F^0, where circular and snowflake-like constant energy contours coexist around which spin locks to momentum. The remnant of the Dirac cone is hybridized with evanescent wave functions injected by metallic layers and pushed, due to charge

transfer from Co or Cu layers, few tenths of eV below E_F^0 for both Bi_2Se_3/Co and Bi_2Se_3/Cu interfaces while hosting distorted helical spin texture wounding around a single circle. These features explain recent observation [11] of sensitivity of spin-to-charge conversion signal at TI/Cu interface to tuning of E_F^0. Crucially for topological spintronics [2, 3, 4, 5, 6, 7, 8, 9, 10, 11], four monolayers of Co adjacent to Bi_2Se_3 host spectral functions very different from the bulk metal, as well as in-plane spin textures (despite Co magnetization being out of plane) due to proximity spin-orbit coupling injected from Bi_2Se_3 into Co. We predict that out-of-plane tunneling anisotropic magnetoresistance in vertical heterostructure Cu/Bi_2Se_3/Co, where current flowing perpendicular to its interfaces is modulated by rotating magnetization from parallel to orthogonal to current flow, can serve as a sensitive probe of the type of spin texture residing at E_F^0.

List of Publications related to this work

1. J. M. Marmolejo-Tejada, J. Velasco-Medina, "Review on graphene nanoribbon devices for logic applications". Microelectronics Journal. Volume 48, February 2016, Pages 18–38.
2. D. V. Tuan, J. M. Marmolejo-Tejada, X. Waintal, B. K. Nikolić, and S. Roche, "Spin Hall effect and origins of nonlocal resistance in adatom-decorated graphene", Phys. Rev. Lett. 117, 176602 (2016).
3. J. M. Marmolejo-Tejada, K. Dolui, P. Lazić, P.-H. Chang, S. Smidstrup, D. Stradi, K. Stokbro, and B. K. Nikolić, "Proximity band structure and spin textures on both sides of topological-insulator/ferromagnetic-metal interface and their transport probes", Nano Lett. 17, 5626 (2017).
4. J. M. Marmolejo-Tejada, J. H. Garcia, P.-H. Chang, X.-L. Sheng, A. Cresti, S. Roche, and B. K. Nikolić, "Origin of nonlocal resistance in multiterminal graphene on hexagonal-boron-nitride: Fermi surface edge states or Fermi sea topological valley currents", arXiv:1706.09361.

1 Introduction

1.1 Overview

Complementary metal–oxide–semiconductor (CMOS) is the most widely used technology for manufacturing integrated circuits (ICs) and systems. The development of silicon-based CMOS has allowed significant improvements in the performance of the electronic circuits within the gadgets and appliances we use every day; however, the most recent reports of the International Technology Guide for Semiconductors (ITRS) warn that typical horizontal dimensional scaling of CMOS technology is reaching fundamental limits [14]. This means it will be impossible to continue decreasing the size of the transistors using the same technological approaches that have been used in the industry for decades, which allowed to roughly double the number of transistors per chip every two years (see Figure 1.1) [15]. Therefore, researchers are looking for alternatives to silicon-based CMOS technology that could enable the production of smaller and faster circuits. This should make it possible to design electronic devices with more integrated functions and higher capabilities.

The ITRS suggests extending the functionality of CMOS integrating heterogeneous material technologies, such as germanium compounds, III-V semiconductor materials and carbon materials; implementing low-power transistors with new operating principles, such as tunneling or spin; and implementing vertical interconnections for 3D integration. This may partially or completely replace silicon in the long term (15-20 years) [16] for improving electronic systems, whose cost and performance are strongly correlated to dimensional and functional scaling (ability to improve size, power, speed or cost without loosing functionality); thus, this is likely to continue driving the semiconductor industry [14], even though there is no obvious succesor to silicon-based technology nowadays [15].

In this context, nanotechnology (manipulation of matter in nanometer dimensions) is especially interesting for scientists around the world because of its unlimited potential. This has encouraged enterprises, universities, research centers, military and national governments to increase their investments in the development of highly-technological tools and products that may solve the difficulties and limitations that current technologies have. Particularly, one of the hot topics for research in nanoelectronics is to identify alternatives to silicon-based devices that may become the new generation of ICs.

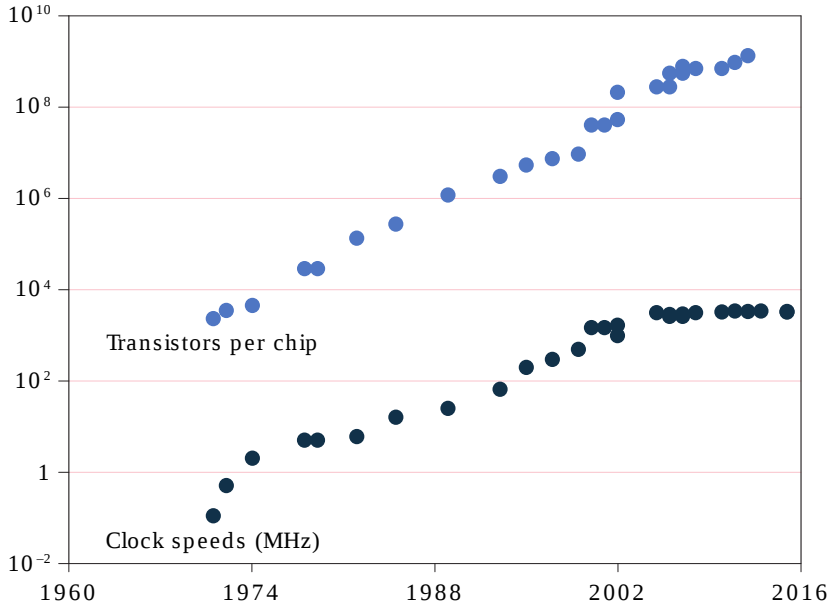

Figure 1.1: Number of transistors per chip and clock speed. Adapted from [15].

The physical properties of graphene and other Dirac materials (DMs) are making them more attractive to the research community, creating big speculations among scientist, but favoring an increasing progress in the field. Therefore, nanostructured devices based on DMs are being studied, modeled and simulated in order to find out the viability of building complex digital circuits that may outperform or improve current silicon-based technologies. For instance, logic circuits with carbon nanotubes were proposed as an alternative to silicon CMOS due to the possibility of obtaining higher performance devices with significantly improved energy efficiency and operation frequency.

Shulaker and co-workers implemented a programmable computer whose logic circuits used carbon nanotube (CNT) transistors and has the capability to concurrently run programs stored in memory; however, its instruction and data memories are outside the chip and their circuits are not made with carbon nanotubes [17]. Moreover, Pei and colleagues demonstrated a modular unit that can perform 16 different logic functions and an 8-bit bidirectional constructed with 6 individualized semiconducting CNTs [18]. Even though their performance is still not comparable to state-of-the-art ICs, these are the most complex and robust carbon-based computational systems up to date. For this reason it is important to consider other nanostructures that could be used to develop reliable systems with this complexity, such as graphene and other DMs.

1.2 Dirac Materials

DMs are characterized by a linear energy band dispersion ($E_{\pm}$) in the momentum space ($\boldsymbol{k}$) close to a Dirac point, as in Equation 1.1, where $\hbar$ is the reduced Planck constant and $\hbar v_F$ is the Fermi velocity. Near such Dirac points, low-energy fermionic excitations behave as massless Dirac particles, allowing ultrahigh carrier mobility and Quantum Hall effects [19, 20]. Figure 1.2 shows typical Dirac cones obtained from this linear band dispersion, which can result from different symmetries, according to the type of material: time-reversal symmetry in topological insulators (TIs) and sublattice symmetry in graphene [19].

$$E_{\pm}\left(\delta\mathbf{k}\right) = \pm\hbar v_F|\delta\mathbf{k}| \tag{1.1}$$

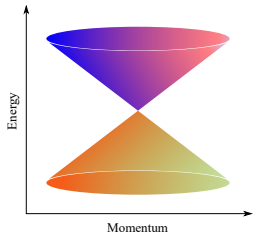

Figure 1.2: Typical linear band dispersion in Dirac materials showing Dirac cones.

1.2.1 Graphene

Graphene is a two-dimensional (2D) atomic-scale honeycomb lattice made of carbon atoms that has higher carrier mobilities than Si and other semiconducting materials (up to 10^6 $\mathrm{cm^2V^{-1}s^{-1}}$ in suspended graphene [21]). It is considered the basis structure of graphitic materials since it can be used to form structures of zero, one, or three dimensions (0D , 1D and 3D), depending on whether these are greater or less than 100 nm (see Figure 1.3). Therefore, graphene can be wrapped to form fullerenes (0D structures), rolled to form nanotubes (1D structures) or vertically stacked to form graphite (3D structure) [22].

Due to its remarkable electrical and mechanical properties, such as high carrier mobility, large conductivity, high chemical and thermal stability, high transparency and flexibility, graphene may be suitable for the next-generation electronic devices [22, 23]. The energy-momentum dispersion of graphene (see Figure 1.4) exemplifies the general characteristics observed in Figure 1.2, showing that π and $\pi*$ bands are totally filled and empty, respectively, and touch at the K and K' points, also referred as Dirac

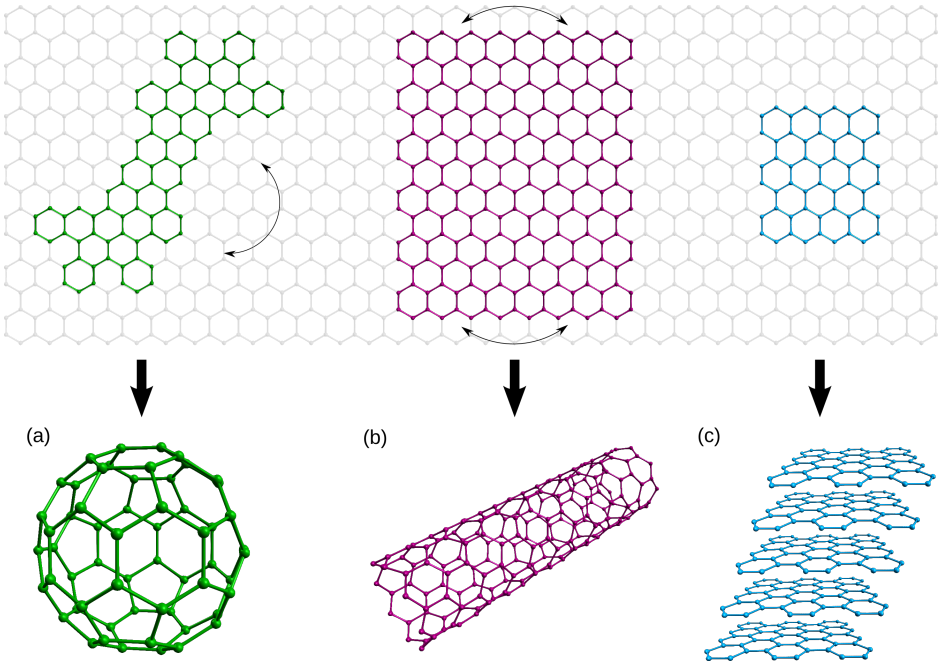

Figure 1.3: Graphene as a building block for graphitic materials. (a) Buckminsterfullerene (bucky-ball). (b) Carbon nanotube. (c) Graphite. Adapted from [22].

points. Near these points, both bands are approximately linear and form two Dirac cones [24, 25].

As seen in Figure 1.4, large-area graphene is a semi-metal with zero bandgap. This causes very low on/off current ratios (I_{on}/I_{off}) when it is used as a transistor channel material in typical field-effect transistors (FETs) because the device cannot be switched off. This represents a major drawback in digital applications, since it is expected that commercial digital devices have very low leakage current when being in off state, similar to that of CMOS technology. Consequently, one of the challenges of graphene-based devices is to reduce the off-state leakage current and improve the I_{on}/I_{off} ratios achieved so far (typically 1 or 2 orders of magnitude) for realistic applications [26].

Nonetheless, graphene can be treated to open up a useful bandgap; thus, researchers have reported the following approaches for bandgap engineering:

1. Forming graphene nanoribbons (GNRs) by constraining large-area graphene in one dimension [27],
2. Biasing bilayer graphene [28, 29],
3. Patterning graphene nanomeshes (GNMs) [30, 31, 32, 33, 34],
4. Applying strain [35, 36],
5. Applying chemical modifications to graphene [37, 38].

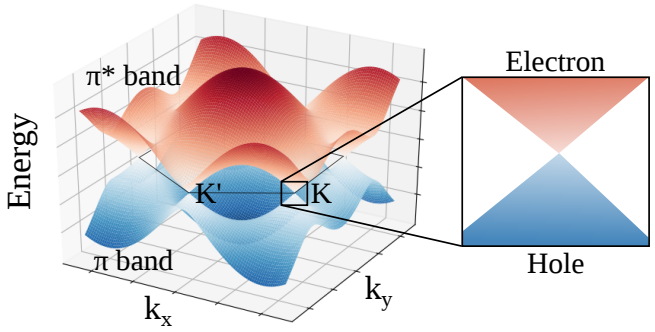

Figure 1.4: Energy-momentum dispersion of infinite graphene. The valence and conduction bands touch at six discrete points, often referred as Dirac points.

These approaches for tuning the electronic properties of graphene and bandgap engineering have been extensively discussed in [39], [26] and [40].

1.2.1.1 Graphene nanoribbons

The properties of GNRs highly depend on their size and edge shape, which can be zigzag (ZGNR) or armchair (AGNR) [27]. Since GNRs are considered periodic across their length, they are usually labeled as N-AGNR and N-ZGNR, where N is the number of carbon atoms along its width. Figure 1.5 shows the atomic structure of a 10-AGNR and a 5-ZGNR.

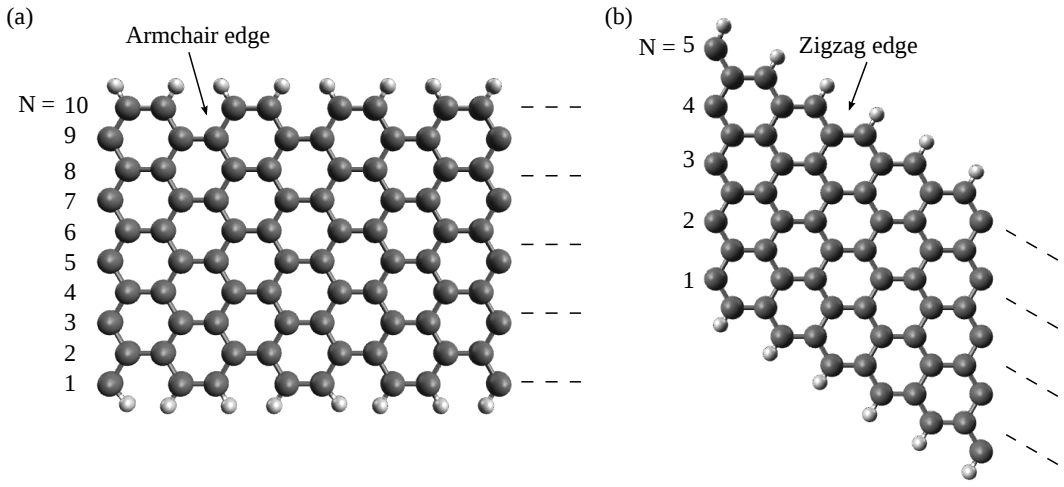

Figure 1.5: Atomic structure of armchair and zigzag GNRs. (a) 10-AGNR. (b) 5-ZGNR.

Tight-binding (TB) calculations without spin degree of freedom show that ZGNRs and

AGNRs with $N = 3p + 2$, where p is an integer number, are metallic, while AGNRs with $N = 3p$ or $N = 3p + 1$ exhibit semiconducting characteristics and might be used as the channel region in FET devices [41]. However, when spin degree of freedom is included in calculations, ZGNRs have a bandgap inversely proportional to the width due to energy splitting from spin-polarized edge states [42, 43]. Moreover, *ab-initio* calculations of AGNRs show that all families are semiconducting, but $N = 3p + 2$ has the smallest bandgap [39].

Experiments at room temperature have shown that narrow ZGNRs (less than 7-nm-wide) are antiferromagnetic semiconductors with bandgaps of ~200-300 meV, while wider ZGNRs have ferromagnetic (metallic) behavior with parallel-aligned spin states at both edges [44]. Furthermore, different processes have been used to fabricate narrow GNRs (with widths below 20 nm and down to 1.4 nm) with semiconductor properties in all cases [45, 46, 47, 48, 49], where GNRs with predominant zigzag edges have smaller bandgap than GNRs with similar width, but predominant armchair edges [50]. Also, researchers have probed the inverse relation between the width of the GNR and its bandgap, that is larger than 0.5 eV for the narrowest ribbons [48] and independent of crystallographic direction [45].

Similar to conventional semiconductors, it has been demonstrated that GNRs with bigger bandgaps have smaller carrier mobilities [23]. There is evidence that devices with bandgaps around 0.2-0.3 eV would require nanoribbons whose widths are less than 5 nm [41]. This constitutes a notorious disadvantage of opening a bandgap in graphene, since the carrier mobility can be reduced in more than two orders of magnitude when reaching bandgaps larger than 0.5 eV, which is required to obtain I_{on}/I_{off} ratios in the order of 10^4-10^7 [23, 51]. Carrier mobility of graphene is frequently stated as its best advantage, and recent studies have demonstrated that the mobility and performance of a GNRFET device can be improved by uniformly doping the GNR, as stated in [52].

Several reviews present comprehensive summaries of graphene and GNR fabrication techniques, defects, electronic, magnetic, mechanical and optical properties, and simulation frameworks for modeling nanoelectronic devices [39, 26, 40, 53, 16] and, from the applications point of view, we summarize in Tab. Table 3.2 both top-down and bottom-up techniques that have been used for manufacturing large area graphene and GNRs with their advantages and disadvantages. Usually, the manufacturing strategies are based on simple and cost-effective methods, but the challenge is to effectively implement the laboratory procedures in the large-scale [54, 40] and prepare GNRs with high aspect ratios (length/width) for device fabrication [55]. The problem of graphene-based applications is that the remarkable properties of graphene have been observed mostly in research laboratories, but realistic applications require industrial large-scale production of samples with performance as good as the obtained on the highest-quality samples [56]. Structurally perfect GNRs could also allow testing of novel physical and device concepts by the production of clean quantum wires, as presented in [57]. Furthermore, graphene for nanoelectronic devices requires the highest quality grade (high

crystallinity and low defect density), which is expected to need more developing time for achieving significant progress [16].

1.2.1.2 Graphene nanomeshes

As previously discussed, GNRs are more difficult to fabricate and are very sensitive to impurities, edge definition (different width among the ribbon) and orientation (armchair or zigzag). The challenge is to be able to fabricate these structures with controlled precision and obtain devices with reproducible properties under ambient conditions [22].

GNMs are basically large graphene sheets patterned with 2D periodical nanoholes that can be seen as a network of GNRs (see Figure 1.6) [31]. The structure and its electronic properties vary according to the size and shape of the nanohole, neck width (shortest edge-to-edge distance between two neighboring nanoholes) and periodicity (centre-to-centre distance between two neighboring nanoholes)[31]. Researchers have demonstrated the viability of bandgap engineering by controlling these parameters [30, 32, 33, 34]. Moreover, GNM structures with square-shaped holes are usually described by N_z (the number of carbon atoms in the zigzag-edge side) and N_a (the number of carbon atoms in the armchair-edge side). These structures are considered to be easier to fabricate and handle with current technologies; then, researchers have demonstrated the formation of GNMs with neck width down to 7 nm using nanoimprint lithography [30]. Additionally, block copolymer templates could be used to create GNMs with features down to 10 nm and higher throughput [58].

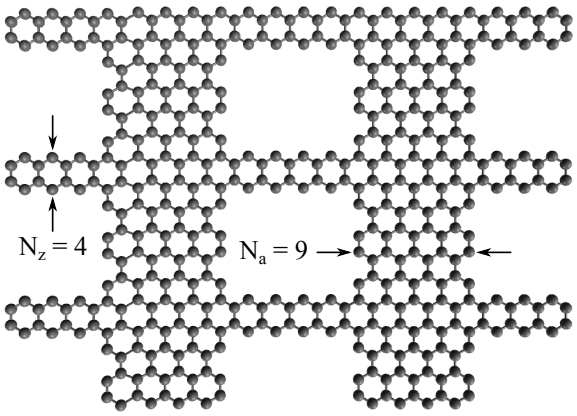

Figure 1.6: Atomic structure of a graphene nanomesh with $N_a = 9$ and $N_z = 4$.

It is desirable to control the periodicity and neck width of the nanoholes independently. For instance, the nanosphere lithography process described in [59] uses commercial or self-assembled colloidal microspheres to pattern GNMs, where the periodicity and neck

width are controlled by the size of the microspheres and the etching time. Narrower necks are expected to have higher on/off ratios. Increased periodicity (with same neck width) reduces the opened bandgap, i.e. there is a direct relation between the bandgap and the number of removed atoms over total atoms, $N_{removed}/N_{total}$ [60].

GNM structures may be formed using different hole shapes, which vary according to the manufacturing techniques under use, but result in similar semiconductor characteristics. For this reason, researchers have focused on modeling and fabrication of GNMs with circular [61, 30, 31, 62, 63, 58, 64, 65], squared [33], triangular [66, 67], rhomboid [67, 32], hexagonal [60, 66] and irregular [64, 34] hole shapes.

Hossain and colleagues studied the electronic transport properties of GNRs with single nanopores [68]. In their study, the authors use AGNRs with a nanopore in its center, varying the width of the nanopore while fixing the width of the GNR. Their simulations indicate better figure of merit ZT ($ZT = S^2\sigma T/k$, where S is the Seebeck coefficient, σ is the electrical conductance, k is the thermal conductance and T is temperature) for $3p + 1$ AGNRs, particularly for wider nanopores that result in narrower GNRs in the center of the device.

Nanopores in graphene have also been used for sensing applications. For instance, BLG with a nanopore was used in [69] for DNA sequencing. By measuring electrical current directly, the proposed method monitors changes in the I-V characteristics of the device when different nucleobases are located inside the nanopore; then, by measuring the changes in the conductance of the device with and without a nucleobase, it is possible to sequence DNA strands.

1.2.1.3 Chemically-modified graphene

An alternative to fabricate GNRs with well defined edges is to apply chemical modifications to graphene for bandgap engineering. According to Seol and Guo, chemical modifications, such as hydrogenation and fluorination, alter the sp^2 hybridization to sp^3, allowing a bandgap induction of few eV (comparable to GNRs) [37]. They propose chemically modified nanorods that are formed by hydrogenation or fluorination and can open a considerable bandgap for the groups $N_g = 3p + 1$ and $3p$, where N_g is the number of graphene lines (N_a is the number chemically modified graphene lines) and p is an integer number (see Figure 1.7). This structure can deliver large on-currents (comparable or larger than silicon devices) because the nanorods form a continuous 2D atomistic layer with uniform edge orientation that can be packed in parallel arrays to obtain larger currents per width; however, the structure needs to be carefully patterned and properly selected to outperform silicon devices.

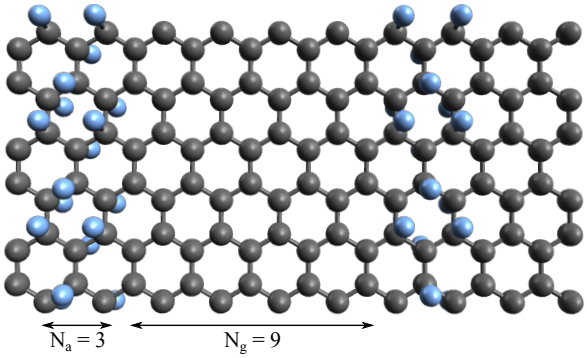

Figure 1.7: Atomic structure of a fluorinated graphene nanorod with $N_g = 9$ and $N_a = 3$ [37].

In order to increase the I_{on}/I_{off} ratio of GNR devices, researchers have also explored hybrid nanoribbons, such as the graphene-hBN device presented in [38] (see Figure 3.1(r)). In this case, the authors use a hBN channel sandwiched by two GNRs and connected to metallic AGNR leads. By applying a transverse electric field F_0 to this channel, the bandgap is significantly reduced and it is possible to switch the channel from semiconducting to conducting, resulting in an I_{on}/I_{off} ratio up to 1.42 $\times$ 10^4.

1.2.2 Topological insulators

A topological insulator (TI) is characterized by an insulating gap in the bulk and gapless edge or surface states (in 2D or 3D objects, respectively) that are protected by time-reversal symmetry, meaning they can insulate on the inside and conduct on the outside without being destroyed by impurities or imperfections (see Figure 1.8) [70, 71, 13, 19].

Interestingly, electrons with inverse spin orientation travel in opposite directions, generating an effective spin current in which the spin direction is locked to the direction of propagation [72]. The Bi_2Se_3 family of materials (Bi_2Se_3, Bi_2Te_3 and Sb_2Te_3) has demonstrated topological surface states theoretically and experimentally. Figure 1.9(a) shows the Local Density of States (LDOS) calculated on the surface of Bi_2Se_3 (111), where the topological surface states form a single Dirac cone at the Γ point [70]. The spin texture has left-handed helicity in the conduction band and right-handed helicity in the valence band, as observed in Figure 1.9(b) for the conduction band of the surface states in momentum space, where the arrows represent the x-y planar spin polarization and the colors represent the z component for the spin polarization as red and blue for spin-up and spin-down, respectively [71]. Moreover, these Dirac cones

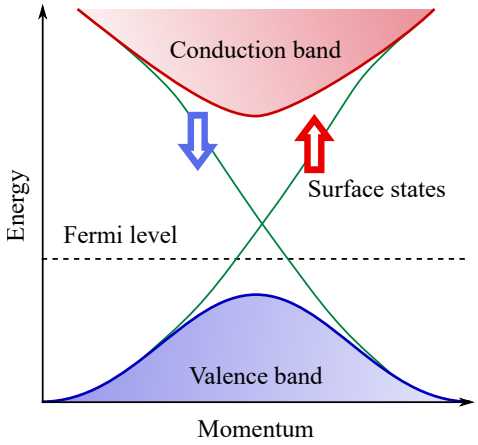

Figure 1.8: Band structure of a typical topological insulator.

have also been demonstrated experimentally, such as the case of Bi_2Se_3 in [73] using high-momentum-resolution angle-resolved photoemission spectroscopy (ARPES) measurements (see Figure 1.9(c)).

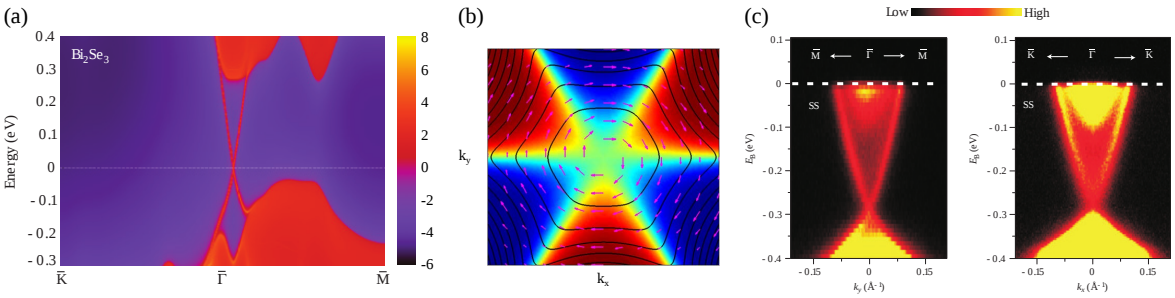

Figure 1.9: (a) Local Density of States on the surface of Bi_2Se_3 (111). (b) Spin texture of the conduction band of the surface states in momentum space for the Bi_2Se_3 TI family of materials. (c) High-resolution ARPES measurements of surface electronic band dispersion on Bi_2Se_3 (111). Adapted from [70], [71] and [73].

Due to their protected edge or surface states that avoid backscattering and strong SO interaction, spintronic or quantum computation applications may be possible with TIs [72] . This could yield to very low-power-consumption devices based on their dissipationless edge or surface channels [13].

2 Introduction to Non-Equilibrium Green's Functions

Compact simulation models for GNR-based devices are required to investigate the technological viability of complex ICs before reaching mass production. It is required to accurately calculate the electronic properties of graphene and other materials, depending on their different geometries, dimensions, and defects. According to the size and complexity of the system, first-principle (*ab-initio*), empirical, semi-empirical methods or analytical models can be used for simulating nanoelectronic devices, as illustrated in Table 2.1.

First-principle	Empirical and semi-empirical	Analytical
Use the laws of physics	Use approximations from experiments	Use equivalent RLC circuits
Model hundreds of atoms	Model thousands of atoms	Model complete devices
Useful for novel materials	Useful for well-known materials	Useful for well-known structures
Highly accurate	Moderate accuracy	Moderate accuracy
High computational resources	Moderate computational resources	Moderate computational resources

Table 2.1: Comparison of first-principle, empirical, semi-empirical methods and analytical models for simulation of nanoelectronic devices.

2.1 First-principle, empirical and semi-empirical calculation methods

First-principle or *ab-initio* calculations are used to calculate the properties of materials by means of the interactions between atoms, molecules and groups of molecules, etc. The methods use the laws of physics and do not rely on approximations or fitting to experimental measurements. For this reason, they help to understand the electronic transport behavior of the device and are of particular interest during the early stages of the device development; however, they require high computational resources and are difficult to implement in standard electronic design automation (EDA) tools, especially when considering complete systems with thousands of atoms.

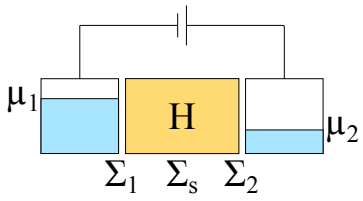

Figure 2.1: General structure used for the simulation of nanoelectronic devices.

In contrast, electronic structure can also be calculated using semi-empirical methods, which are computationally less expensive because the models are fitted with parameters obtained from experiments or first-principles calculations. This produces inaccuracy in the calculations and may yield to different quantitative and qualitative results when they are compared to first-principles calculations. Moreover, some assumptions and approximations, such as a complete or linear potential drop in the channel region or contact interface, can be considered in order to make the calculations easier, but these are not accurate in every supply voltage for very small channels [74].

The nonequlibrium Green's function (NEGF) – Landauer approach is generally used for electronic transport computation. Solving the Green's function $G(E)$ allows the calculation of free charge concentration, transmission coefficients and current through the device.

Self-consistent calculations of $N \times N$ matrices have to be performed, where the matrices are written down depending on the material and the simulation approach (first-principle or semi-empirical), and N depends on the number of basis functions needed to represent the channel of the device [75].

For the particular case of graphene sheets and GNRs, Lewenkopf and Mucciolo presented a complete compilation of the fundamentals and examples for implementing the recursive Green's function method. This method provides the expressions and algorithms for computing conductance, density of states and current density [76]. Furthermore, the roadmap for graphene presented in [16] reviews multiscale modeling techniques and computational tools for understanding and predicting the physical behavior of materials and devices. The basic FET schematic shown in Figure 2.1 is generally used for simulations, and the modeling theory is extended to any nanoelectronic device, considering the following [75]:

- There is an active channel described by a Hamiltonian $[H]$ that also includes any potential U due to other charges:

$$H = H_0 + U([\delta\rho]) \tag{2.1}$$

  This potential may be external (on the electrodes) or internal (within the channel), with $\delta\rho$ being the change in the density matrix $[\rho]$. $[H]$ is Hermitian and

represents conservative dynamical forces. It is constructed using first-principle (with density functional theory (DFT)) or semi-empirical (with tight-binding (TB)) calculations:

- For DFT calculations, the channel is described by the single particle Kohn-Sham Hamiltonian in Equation 2.2, where V_H, V_{xc} and V_{ext} correspond to the Hartree, exchange-correlation and external potential contributions [77]:

$$H_{KS} = -\frac{\hbar^2\nabla^2}{2m} + V_H + V_{xc} + V_{ext} \tag{2.2}$$

- TB Hamiltonians usually provide good qualitative results, however, they can be modified for including edge considerations and correlation effects due to quantum confinement in order to increase accuracy and match first-principle results, as summarized in [39] for the particular case of graphene. Bulk graphene can be modelled by the single electron Hamiltonian in Equation 2.3, where t_{ij} is the hopping from site i to j in the honeycomb lattice (equal to 2.7 eV), and V_i is the on-site potential (equal to zero when no gating nor disorder effects are accounted) [76].

$$H_0 = -\sum_{i \neq j} \left(t_{ij} \left|i\right\rangle \left\langle j\right| + \text{H.c}\right) + \sum V_i \left|i\right\rangle \left\langle i\right| \tag{2.3}$$

- The channel communicates the contacts (typically, source and drain), which are maintained in local equilibrium with specified electrochemical potentials. This is described by the self-energy matrices $[\Sigma_1]$ and $[\Sigma_2]$.
- The interactions of a single electron with its surroundings is described by a self-energy matrix $[\Sigma_s]$ and has to be calculated self-consistently. These self-energy matrices are non-Hermitian and determined by "entropic forces".
- In the ballistic limit, the flow of electrons is determined by the contacts and the interactions within the channel are negligible. The opposite is considered in the diffusive limit, where the flow of electrons is determined by the electron interactions within the channel and the role of the contacts is negligible.

In order to obtain accurate calculations and reduce the computational cost of pure first-principle calculations, researchers propose the combination of first-principle and semi-empirical calculations to perform electronic transport calculations. For this purpose, Bruzzone and colleagues suggest to:

1. Use DFT to calculate the Hamiltonian of the material,
2. Perform a basis set transformation (from Bloch to Wannier) and

3. Solve the Green's function $G(E)$ to obtain the transport characteristics of the device [78].

Furthermore, Faghaninia and colleagues propose a fully first-principle approach to model carrier transport in semiconductor materials that takes fully account of the effects of elastic and inelastic scattering on charge carriers. With this, they compute the electron and phonon band structures and predict the material properties as a function of temperature or carrier concentration [79]. As stated by the authors, the most important advantage of these fully first-principle calculations is that it aims to accurately predict the electronic transport properties of novel materials, avoiding approximations and limitations from unavailability of experimental data; however, this approach is limited to low-field electronic transport in n-type semiconductors.

Once the Hamiltonian and the self-energy matrices are obtained, $G(E)$ is calculated according to Equation 2.4, where E corresponds to the Eigenenergies and I is the identity matrix. Thereafter, the transmission $T(E)$ (probability that an electron is transmitted from one contact to another) is calculated with Equation 2.5, where $\Gamma_{1,2,s}$ are the broadening functions (Equation 2.6) that introduce an imaginary part to the energy [80].

$$G(E) = [EI - H - \Sigma_1 - \Sigma_2 - \Sigma_s]^{-1} \tag{2.4}$$

$$T(E) = \text{trace}\left(\Gamma_1 G \Gamma_2 G^{\dagger}\right)^{-1} \tag{2.5}$$

$$\Gamma_{1,2,s} = i\left[\Sigma_{1,2,s} - \Sigma_{1,2,s}^{\dagger}\right] \tag{2.6}$$

Current is then calculated with Equation 2.7, assuming that all contacts remain in local equilibrium according to specified Fermi functions $f(E)$, given by Equation 2.8.

$$I = -\frac{q}{h}\int T(E)\left(f_1(E) - f_2(E)\right)dE \tag{2.7}$$

$$f_{1,2}(E) = \frac{1}{1 + exp\left(\frac{E-\mu_{1,2}}{k_B T_{1,2}}\right)} \tag{2.8}$$

When finite bias voltage is applied to the leads (required for calculating the complete transfer characteristics of the device), the potential profile has to be determined self-consistently by solving the Poisson equation for the potential U (Equation 2.9, where ε_0 is the permittivity of free space and ε_r is a spatially varying relative permittivity) and updating the Hamiltonian [81]. Figure 2.2 summarizes the self-consistent transport calculation algorithm, where c is the convergence criterion.

$$\vec{\nabla} \cdot \left(\varepsilon_r \vec{\nabla} U \right) = -\frac{q^2}{\varepsilon_0} \delta\rho \tag{2.9}$$

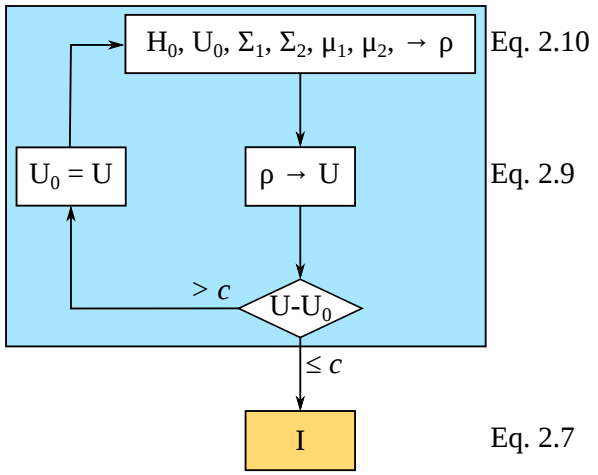

Figure 2.2: Self-consistent transport calculation algorithm based on [81].

Then, $[\rho]$ is obtained from Equation 2.10 using the correlation function $[G^n]$, the spectral functions $[A_{1,2}]$, and the Green's function $[G]$ without electron-phonon interactions given by Equation 2.11, Equation 2.12 and Equation 2.13, respectively [81].

$$\rho = \int_{-\infty}^{+\infty} \left(\frac{dE}{2\pi} \right) \left[G^n \left(E \right) \right] \tag{2.10}$$

$$G^n \left(E \right) = \left[A_1 \left(E \right) \right] f_1 \left(E \right) + \left[A_2 \left(E \right) \right] f_2 \left(E \right) \tag{2.11}$$

$$A_{1,2} \left(E \right) = G \left(E \right) \Gamma_{1,2} \left(E \right) G^{\dagger} \left(E \right) \tag{2.12}$$

$$G \left(E \right) = \left[EI - H - \Sigma_1 - \Sigma_2 \right]^{-1} \tag{2.13}$$

2.2 Landauer-Büttiker formalism

For the multiterminal device shown in Figure 2.3, current at the ith terminal is given by Equation 2.14 [82, 83]:

$$I_i = \frac{q}{h} \sum_j \int \mathrm{d}E \bar{T}_{ij} \left[f_j - f_i \right] \tag{2.14}$$

Where the Fermi function $f\left(E - E_f\right)$, transmission from terminal j to i $\bar{T_{ij}}$, broadening function Γ for each terminal, and Green's function G are given as follows [82, 83].

$$f\left(E - E_f\right) = \frac{1}{1 + exp\left(\frac{E - E_f}{k_B T}\right)} \tag{2.15}$$

$$\bar{T}_{ij} = \mathrm{Tr}\left[\Gamma_i G \Gamma_{,j} G^{\dagger}\right] \tag{2.16}$$

$$\Gamma_j = i\left[\Sigma_j - \Sigma_j^{\dagger}\right] \tag{2.17}$$

$$G = \left[E - H - \Sigma_0 - \Sigma_1 - \Sigma_2 - \Sigma_3\right]^{-1} \tag{2.18}$$

For small bias voltages and finite temperature, the difference in Fermi functions can be expanded into Taylor series; then, the current at the ith terminal is approximated to Equation 2.19:

$$I_i = \frac{q}{h} \sum_j \int \mathrm{d}E \bar{T}_{ij} \left(-\frac{\partial f}{\partial E} \right) \left[\mu_j - \mu_i \right] \tag{2.19}$$

Moreover, I_i can be approximated to Equation 2.20 for the case of zero temperature and small bias voltage:

$$I_i = \frac{q}{h} \sum_j \bar{T}_{ij} \left[\mu_j - \mu_i \right] \tag{2.20}$$

Considering the latter case, it is possible to build the following system of equations to calculate I_0, μ_1 and μ_3, by setting $\mu_0 \neq 0$, $\mu_2 = 0$ and considering $I_1 = I_3 = 0$:

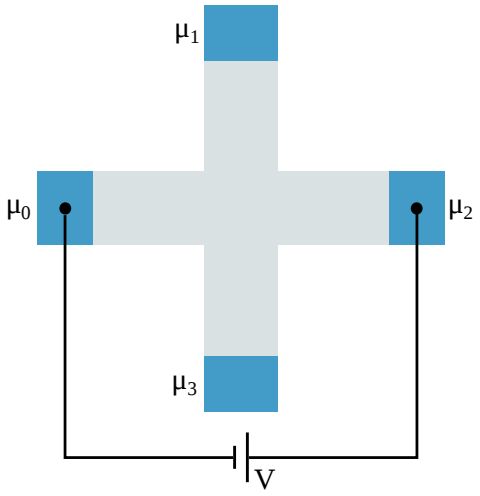

Figure 2.3: Schematic of a four-terminal device.

$$\begin{Bmatrix} I_0 \\ I_1 \\ I_3 \end{Bmatrix} = \frac{q}{h} \begin{bmatrix} \bar{T}_{10} + \bar{T}_{20} + \bar{T}_{30} & -\bar{T}_{10} & -\bar{T}_{30} \\ -\bar{T}_{01} & \bar{T}_{01} + \bar{T}_{21} + \bar{T}_{31} & -\bar{T}_{31} \\ -\bar{T}_{03} & -\bar{T}_{13} & \bar{T}_{03} + \bar{T}_{13} + \bar{T}_{23} \end{bmatrix} \begin{Bmatrix} \mu_0 \\ \mu_1 \\ \mu_3 \end{Bmatrix}$$

2.3 Spin degree of freedom

Spin electronics or spintronics refers to the active manipulation of spin degrees of freedom in solid-state systems [84]. Spintronic devices are possible candidates for replacing CMOS devices due to the expectations of obtaining extremely low-power circuits [85]. Traditionally, spintronic devices aimed to effectively control spin in silicon for integration with current technologies, however, the field is seeking for integration with other materials (all-semiconductor structures rather than hybrid structures with metallic ferromagnets), based on theoretical and experimental observations on device performance [84]. For this purpose, it is necessary to create, transport, manipulate and detect spin populations within the device [85], for which long spin lifetimes and spin control are simultaneously required [16].

Heat generation is the biggest factor that limits CMOS scaling because of the dissipative nature of electron charge transport. In contrast, coherent spin rotation is not dissipative and devices operating under spin transport should enable scaling beyond CMOS [85], given that dissipation energy in spintronic devices is predicted to be smaller than the thermal limit (k_BT) per operation [86].

For conventional electronic circuits, spin-↑ and spin-↓ electrons propagate equally in the same direction, resulting in pure charge current $I = I^{\uparrow} + I^{\downarrow} \neq 0$ that is spin

unpolarized $I^S = \frac{\hbar}{2q}\left(I^{\uparrow} - I^{\downarrow}\right) = 0$ (see Figure 2.4(a)). Spin-↑ and spin-↓ electrons can be polarized in certain systems, such as ferromagnetic elements in metallic devices, in order to obtain unequal spin-↑ and spin-↓ currents (see Figure 2.4(b)) that results in $I \neq 0$ and $I^S \neq 0$. Finally, pure spin current is obtained if the spin-↑ and spin-↓ electrons propagate equally in opposite directions (see Figure 2.4(c)); then, $I = 0$ and $I^S \neq 0$ [87]. The challenge is to find mechanisms for generating and detecting spin currents, both theoretically and experimentally. Moreover, the objective is to efficiently implement spin injection, detection, gating and manipulation for enabling all-spin-based circuits for both conventional electronics and quantum information processing [16].

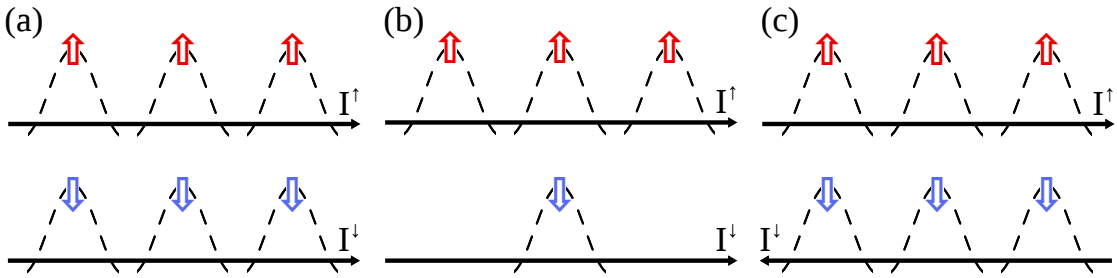

Figure 2.4: Classification of spin I^S and charge I currents in metal and semiconductor spintronic systems [87]. (a) Conventional charge current ($I = I^{\uparrow} + I^{\downarrow} \neq 0$, $I^S = \frac{\hbar}{2q}\left(I^{\uparrow} - I^{\downarrow}\right) = 0$). (b) Spin-polarized charge current ($I \neq 0$, $I^S \neq 0$). (c) Pure spin current ($I = 0$, $I^S \neq 0$).

2.3.1 Spin current

In order to measure the ratio of charge to spin current conversion, the spin current $I_i^{S_\alpha}$ at the ith terminal is calculated from Equation 2.21 [88, 89, 90]:

$$I_i^{S_\alpha} = \frac{q}{h}\sum_j \int \mathrm{d}E \mathrm{Tr}\left[\hat{\sigma_\alpha}\Gamma_i G \Gamma_j G^{\dagger}\right][f_j - f_i] \tag{2.21}$$

Where $\hat{\sigma_\alpha}$ corresponds to the Pauli matrices $\hat{\sigma_x} = \begin{bmatrix} 0 & 1 \\ 1 & 0 \end{bmatrix}$, $\hat{\sigma_y} = \begin{bmatrix} 0 & -i \\ i & 0 \end{bmatrix}$ and $\hat{\sigma_z} = \begin{bmatrix} 1 & 0 \\ 0 & -1 \end{bmatrix}$.

Then, for the cross-bar shown in Figure 2.3, the spin Hall conductance G_{SH} and spin

Hall angle θ_{SH} are calculated according to Equation 2.22 and Equation 2.23, respectively [91].

$$G_{SH} = \frac{I_1^S}{V_1 - V_3} \tag{2.22}$$

$$\theta_{SH} = \frac{I_1^S}{I_0} \tag{2.23}$$

2.3.2 Spin Hall effect

One of the most popular methods to generate pure spin current is the spin Hall effect (SHE). For this, the sample material requires the coupling between the orbital and the spin degree of freedom of electrons, known as Spin-Orbit coupling (SOC). As observed in Figure 2.5(a), spin-orbit (SO) interactions within a sample carrying a longitudinal charge current produce a transverse separation of spin-↑ and spin-↓ electrons. The inverse SHE (iSHE) occurs on a sample with SO interactions carrying longitudinal spin current that generates transverse charge current (see Figure 2.5(b)); therefore, this effect is one of the preferred methods to detect spin currents.

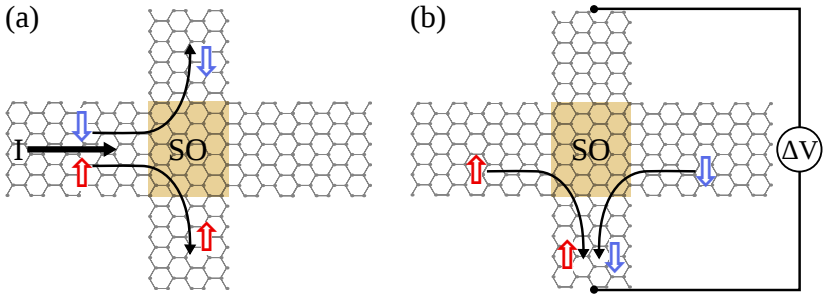

Figure 2.5: (a) Spin current generation due to SHE phenomenology. (b) Spin current detection due to iSHE phenomenology.

The devices shown in Figure 2.6 is used to generate spin current in the central region by driving a charge current (I_{DS}) between the left side terminals due to SHE. This spin current is measured by the right side terminals due to iSHE, which is known as the non-local voltage (V_{NL}). The non-local resistance ($R_{NL} = V_{NL}/I_{DS}$) characterizes devices using different materials that could be more or less effective in converting charge to spin current and vice versa.

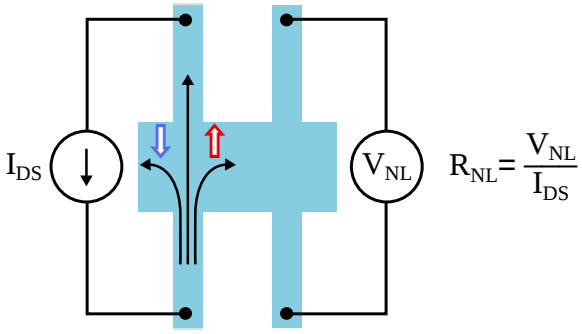

Figure 2.6: Non-local spin Hall measurement.

2.3.3 Spin-Orbit coupling

The magnetic moment of an electron is given by $\vec{\mu}_s = -g\mu_B \vec{S}/\hbar$, where $\vec{S}$ is the spin angular momentum, μ_B is the Bohr magneton ($5.78 \cdot 10^{-5} eV \cdot T^{-1}$) and g is the electron spin g-factor (≈ 2); then, $\vec{\mu}_s$ is always antiparallel to $\vec{S}$, as observed in Figure 2.7. In the laboratory frame (see Figure 2.7(b)), the magnetic moment, moving with velocity $\vec{v}$ generates electric moment $\vec{P}_{lab} = \vec{v}/c^2 \times \vec{\mu}_s$, which, in presence of an electric field $\vec{E}_{lab}$, feels the deflection force $\vec{F} = \left(\vec{P}_{lab} \cdot \nabla\right) \vec{E}_{lab}$. This creates a spin current I^S perpendicular to $\vec{E}_{lab}$.

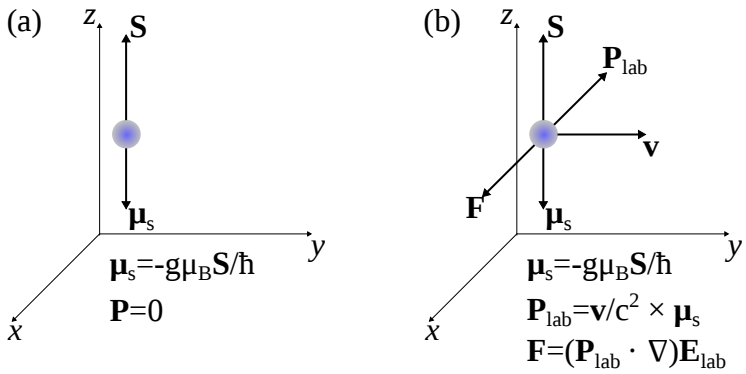

Figure 2.7: Electric moment and Force due to SO coupling. (a) Instantaneous rest frame of an electron. (b) Laboratory frame.

SOC can modify the electronic band structure of a particular system by splitting degenerate bands with finite angular momentum (p, d and f) [92]. The form of such band splitting depends on the system and broken symmetries [93]. For instance, Rashba SOC [94] occurs in systems with broken inversion symmetry at the surface or interface. This results in an electric field that couples to the spin of electrons and produces spin-split bands where spin and momentum degrees of freedom are locked (see Figure 2.8(a)).

Such spin polarization can be used for charge-to-spin and spin-to-charge conversion by means of the Edelstein and inverse Edelstein effects [95].

Similar to Rashba SOC, topological surface states in TIs also exhibit spin-momentum locking in their characteristic Dirac cone (see Figure 2.8(b)) due to the connection of bulk valence and conduction bands, which generally results in a more effective spin-to-charge conversion [92].

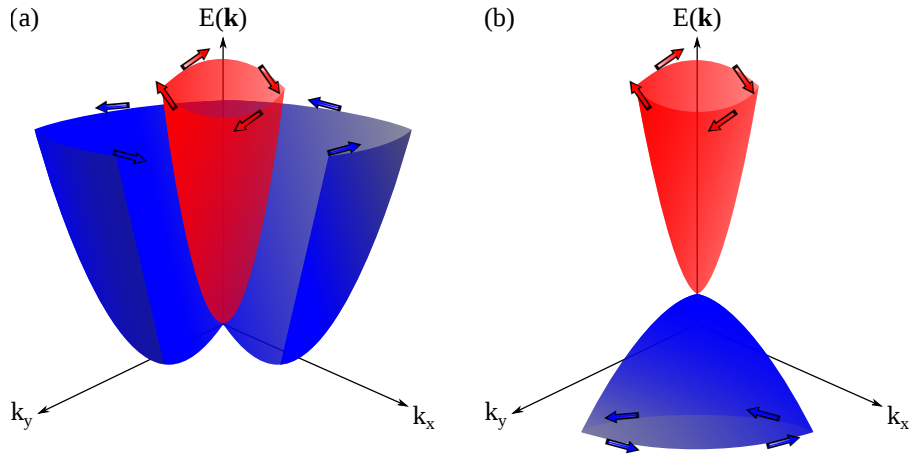

Figure 2.8: Spin-momentum locking in (a) Rashba interfaces and (b) Topological insulators.

2.3.4 Enhancement of Spin-Orbit coupling

According to Kane and Mele, graphene allows SO interaction that results in SHE at low energy, enabling the transport of charge and spin currents in gapless edge states [96]. This effect is very low in pristine graphene; then, researchers have looked for means to enhance the SO coupling in graphene by introducing adatoms.

Generally speaking, small dimensions can improve SOC effects significantly [92]. Moreover, Balakrishnan and colleagues showed that the SO interaction can be improved three orders of magnitude at room temperature by adding small concentrations of covalently bonded hydrogen atoms to graphene [97]. This is achieved by means of out-of-plane deformations that are only possible in materials with high in-plane strength, such as graphene. Starting from pristine graphene, they showed a 400% increase in R_{NL} with only 0.02% hydrogenation, which also decreases mobility when the hydrogen concentration is increased. Also, there is a high dependence on the dimensions of the device (where a higher width/length ratio is more desirable); then, it is required to carefully design these devices and choose a proper impurity concentration to obtain better performance. Finally, other materials, such as nickel and gold, are used to

chemically modify graphene and enhance SO interactions, such as the graphene system decorated with gold adatoms presented in [98].

2.3.5 Edelstein effect

Systems with spin-momentum locking (Rashba SOC interfaces and TIs) can be used to convert charge current to spin current by means of the Edelstein effect [95]. Transverse spin accumulation is obtained when applying an in-plane charge current J_C to the device. For the particular case of TIs, Figure 2.9(a) shows that J_C at the surface shifts the Fermi contour and generates a non-zero spin accumulation. This can diffuse to an adjacent layer and inject a spin current into the material.

Similarly, the inverse Edelstein effect is used for converting spin current to charge current, as seen in Figure 2.9(b), where a spin current is injected into the surface states of a TI, causing a shift in the Fermi contour by overpopulating states on one side and depopulating states on the other that result in an in-plane charge current J_C.

From the application point of view, the Edelstein effect can be observed in the two-terminal device configuration from Figure 2.9(c), consisting on five quintuple layers (QLs) of Bi_2Se_3 connected to two macroscopic reservoirs [99]. When applying an unpolarized charge current along the x axis, a non-zero spin density is generated at the top and bottom surfaces of the TI. Moreover, the inverse Edelstein effect (together with the iSHE) is shown in Figure 2.9(d), where a nanomagnet is connected to a stack of materials with high SOC for generating a charge current J_C along the x ($-x$) axis when a spin current J_S along the z ($-z$) axis appears due to the magnetization of the nanomagnet $\hat{m}$ in the y ($-y$) direction [100]. This combination of spin effects are being considered for developing new logic and memory devices with very low power consumption.

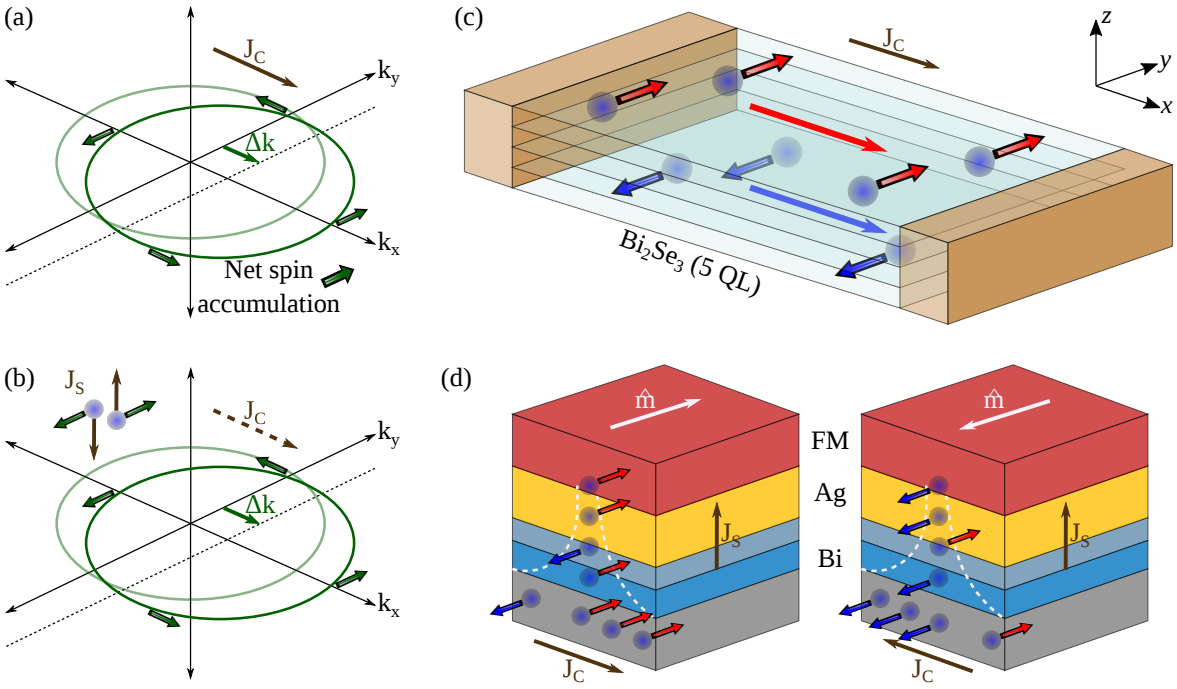

Figure 2.9: (a) Edelstein effect in Topological insulators for charge-to-spin conversion [92]. (b) Inverse Edelstein effect in Topological insulators for spin-to-charge conversion [92]. (c) Two-terminal device configuration where a thin film of a Topological insulator is attached to two macroscopic reservoirs for generating non-zero spin density at the surfaces once an unpolarized charge current is injected along the x axis [99]. (d) Inverse Edelstein and spin Hall effects on a heterostructure with high SOC for spin-to-charge current conversion, where a change of direction in the magnetization of a ferromagnetic layer generates a charge current along the x or -x axis [100].

3 Charge transport devices based on graphene channels

3.1 Introduction

Due to the high carrier mobility in graphene, the initial approach is to directly replace silicon channels with graphene in traditional FETs, however, the zero-gap of large-area graphene results in low I_{on}/I_{off}. In this chapter, we summarize some approaches for charge transport devices using graphene-based channels that work on differetn physical principles, such as field effect, tunneling effect, ambipolar conduction and negative resistance. Table 3.1 summarizes the simulation performance of GNR-based devices found in the literature.

3.2 Field-effect devices

As observed in Figure 3.1(a), the channel in the top/back or double gate FET structures may be a single layer of graphene (SLG) or bilayer graphene (BLG). Normally, the channel is intrinsic, while the source and drain contacts are assumed to be heavily doped BLG or AGNR (MOS-GNRFETs), which dominate the current flow in the device; however, large graphene sheets might be connected to the source and drain contacts to obtain low contact resistance. Also, the channel can be formed by an array of GNRs in order to increase the on-state current and conserve a useful bandgap. By increasing the number of GNRs from 1 to 2, the authors in [101] calculated a duplication in the transmission probability and drain-current of AGNRFETs. The gate insulator is usually SiO_2, but high-k dielectric materials are also being used in order to reduce the leakage current in the gate terminal. The source and drain contacts can also be metallic, producing Schottky barriers at the junctions (SB-GNRFETs), which govern the electronic transport properties of the device. These Schottky barrier devices have better speed and power dissipation than CMOS and MOS-GNRFETs, but present high leakage power and low I_{on}/I_{off} ratio [102].

Moreover, SB-GNRFETs are preferred because no doping in the channel nor the contacts is required, avoiding technical difficulties in fabrication and doping variation

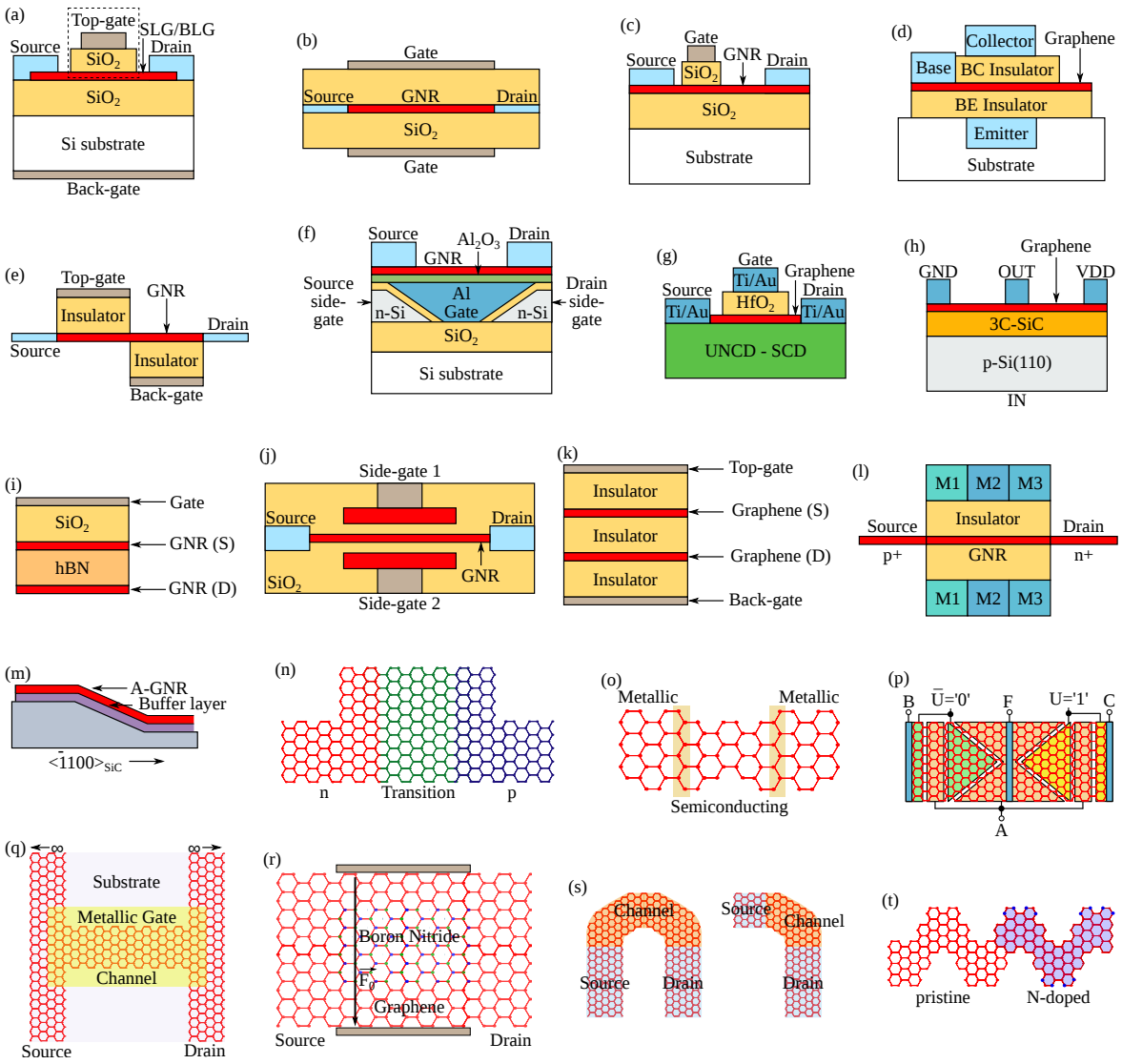

Figure 3.1: Structures for graphene/GNR-based devices. (a) Top/Back-gate FET. (b) Double-gate GNRFET used for a resonant tunneling transistor (RTT) [109]. (c) Asymmetric gate Schottky barrier GNRFET (SB-GNRFET) [110]. (d) Graphene base transistor (GBT) [111]. (e) GNR-based negative resistance device [103]. (f) Buried triple-gate GNR tunneling FET [112, 113]. (g) Graphene on diamond [114]. (h) Logic inverter based on two graphene-on-silicon FET (GOSFET) [115]. (i) Vertical GNR-hBN FET (VTGNRFET) [104]. (j) Side-gate field-effect bandgap modulation (FEBM) GNR transistor [116, 105]. (k) Symmetric tunneling FET (SymFET) [106]. (l) Barrier-controlled tunnel FET (BC-TFET) [117]. (m) All-graphene device [48]. (n) T-shape AGNR PN junction [118]. (o) Multi-junction GNR [119]. (p) Modified MUX-based graphene logic device [120]. (q) Wide-narrow-wide GNRFET [121]. (r) Graphene/BN heterostructure with transverse electric field [38]. (s) Curved GNRs [122]. (t) Chevron-type pristine and nitrogen-doped GNR (p-N-GNR) heterojunction [123].

Device	Subthreshold slope (mV/decade)	I_{on}/I_{off}	Ref.
GNR-based negative differential resistance device		$>10^5$	[103]
Vertical graphene-hexagonal boron nitride FET	170	1.8 x 10^4	[104]
Bandgap modulation with transverse field	37	$\sim 10^3$	[105]
Symmetric tunneling FET		10^2–10^3	[106]
Graphene nanomesh		$>10^2$	[31]
Nitrogen-passivated ZGNRFET with doped channel		~ 12	[107]
Homojunction tunnel FET	60	10^5	[108]
Hydrogenated GNR		$\sim 10^4$	[37]
Graphene/boron nitride nanoribbon device		1.42 × 10^4	[38]

Table 3.1: Simulation performance of GNR-based devices.

issues, but to the expense of lower I_{on}/I_{off} ratios due to ambipolarity of graphene [110]. In order to avoid parasitic tunneling current in the drain contact, Gholipour and colleagues propose asymmetric gate SB-GNRFETs (see Figure 3.1(c)) to improve its I_{on}/I_{off} ratio by reducing I_{off} significantly, in addition to subthreshold swing reduction.

AGNRs have been theoretically predicted to have better carrier transport properties than BLG, n-channel Si MOSFETs and InP-high-electron-mobility transistors (HEMTs) [124, 125], particularly when they are used in GNRFETs with ribbon widths around 3-4 nm; however, recent studies have shown that thermal conductivity decreases around three orders of magnitude in GNRs with widths smaller than 10 nm, indicating a direct relation between the width of the GNR and its diffusive thermal conductivity and effective mean free path [126].

Experimental measurements on GNRFETs are essential to verify theoretical predictions and find out whether the devices are viable or not. Tahy and co-workers present the electronic transport properties of *p-n* junctions formed in a GNRFET that uses a single GNR with width of 30 nm [127]. As expected, the device has very low bandgap, which makes it impossible to completely turn the transistor off; however, it presents current densities comparable to Si-MOSFETs and III-V Nitride HEMTs, ranging between 1-1.5 A/mm.

Low-power electronic devices that fulfill the CMOS technology requirements have not

been demonstrated; thus, novel device architectures (beyond basic GNR devices) need to be explored [16]. Devices with higher performance should be obtained by using conventional FET operation combined with other effects, such as bandgap modulation. This would mean additional gate control to decrease the bandgap in the on-state and keep the original bandgap in the off-state in order to enhance I_{on} and improve the subthreshold swing [105]. The GNR transistor with field-effect bandgap modulation (FEBM) presented in [116] (see Figure 3.1(j)) uses side gates to apply a transverse field to the GNR and reduce its bandgap; therefore, the off-state is obtained by means of the intrinsic bandgap of a narrow GNR, while the on-state is obtained by means of a narrower bandgap that enhances electron transport through the channel, which also results in higher on-currents and better subthreshold swing, compared to a typical FET.

Moreover, the performance of graphene-based devices can significantly differ according to the manufacturing processes that are used, commonly known as top-down or bottom-up techniques. Top-down approaches use deposition and etching procedures for printing or transferring nanomaterials onto the desired substrate, while bottom-up approaches uses the ability to form the nanostructures by spontaneous or directed assembly (see Figure 3.2) [54].

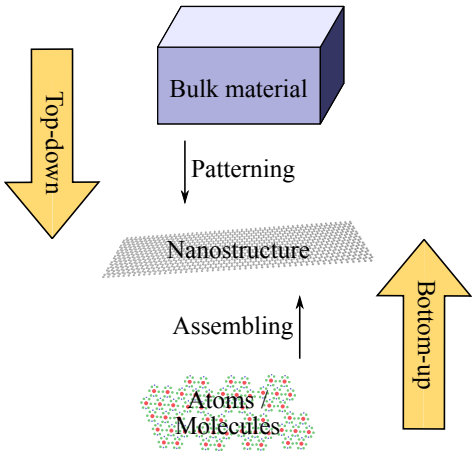

Figure 3.2: Top-down and Bottom-up fabrication [54].

For the particular case of graphene sheets and GNRs, both top-down and bottom-up techniques have several advantages and disadvantages, as shown in Table 3.2. Usually, the manufacturing strategies are based on simple and cost-effective methods, but the challenge is to effectively implement the laboratory procedures in the large-scale [54, 40] and prepare GNRs with high aspect ratios (length/width) for device fabrication [55]. The problem of graphene-based applications is that the remarkable properties of graphene have been observed mostly in research laboratories, but realistic applications require industrial large-scale production of samples with performance as good as the

obtained on the highest-quality samples [56]. Structurally perfect GNRs could also allow testing of novel physical and device concepts by the production of clean quantum wires, as presented in [57]. Furthermore, graphene for nanoelectronic devices requires the highest quality grade (high crystallinity and low defect density), which is expected to need more developing time for achieving significant progress [16].

3.2.1 Top-down manufacturing approaches

Several manufacturing techniques have been proposed to produce high-quality graphene in wafer scale. Epitaxy has allowed the uniform growth of 1-2 layers of graphene on silicon carbide (SiC) wafers in a highly reproducible process [136]. Similarly, chemical vapor deposition (CVD) has been used to produce low-cost graphene in large scale in which the graphene layer is formed on copper and then transferred to another substrate, such as a silicon wafer [136].

Considering the requirements of commercial devices (specially the high on/off current ratio), researchers are extensively working on new fabrication techniques and device structures that could make GNRs suitable for commercial use in logic circuits. The challenge is to be able to fabricate the structures with controlled precision and obtain devices with reproducible properties under ambient conditions [22].

The conventional techniques used to fabricate GNRs are generally difficult to integrate into large-scale processes, in addition to the difficulty to control the width and edge orientation of the ribbon, and the potential damage caused by plasma or oxidizing steps [49]. It is desirable to tune the electronic properties of the prepared GNRs, but there are many technological difficulties that limit the scalability of the processes, making these techniques unpractical to produce very narrow GNRs with clean edges, which are required to open a useful bandgap [131]. Nonetheless, it is possible to pattern GNRs with features down to 10 nm that remain stable at room temperature [45, 22].

Hwang and colleagues report the patterning of GNRs with widths down to 12 nm using electron beam lithography and a CVD process [129]. Li and colleagues present a chemical process to fabricate sub-10-nm smooth-edge GNRs by exfoliating commercial graphite [46]. When using these GNRs as the channel material in FETs, the authors measured I_{on}/I_{off} ratios up to 10^7 at room temperature, however, some of the fabricated GNRs have irregular shapes (different widths across the ribbon, sharpened endings, bending and kinking) that may result in variation of its electrical properties and unreliability of device performance. This process may also result in curved GNRs, whose electronic transport properties are studied in [122] when coupled to straight leads (see Figure 3.1(s)). The authors calculated steady state currents using a time-dependent formalism and found that electron transport is smoother in straight GNRs due to increased scattering in curved GNRs. This also results in higher bandgaps for higher angles between the leads. Moreover, currents at the edges are very sensitive

Technique	Advantages	Disadvantages	Min. width (nm)	Carrier mobility ($cm^2V^{-1}s^{-1}$)	Bandgap (meV)	I_{on}/I_{off}	Ref.
Mechanical exfoliation and lithography	- Formation of single-layer GNRs	- No precise control of GNR edges - Difficult in large-scale	∼15		∼200		[45]
Exfoliation and chemical treatment	- Nearly pristine GNRs - Smooth edges	- Non-uniform shapes	<10	∼100−200	>300	up to 10^7	[46]
Exfoliation and catalytic etching	- Well-defined edges	- Etching along crystallographic directions	∼15				[128]
Metal-assisted etching	- Aligned GNRs - Large-scale	- Large and non-uniform width	19		∼100	∼7−10 up to 5000	[49]
CVD and electron beam lithography	- Wafer-scale graphene - Controllable dimensions	- Unavailable information on edge definition	12		∼100	∼10	[129]
CVD, electron beam lithography and neutral beam etching	- Aligned GNRs - Ultra-low defects	- Unavailable results for narrower GNRs	70 (tested) down to 30	>200		$\sim10^3$ -10^4	[130]
CVD and STM nanolithography	- Narrow GNRs with defined crystallographic orientations	- Edge roughness - Difficult in large-scale	3		∼300		[44]
Direct growth on silicon dioxide	- No substrate transfer - Large-scale production	- Formation of plateaus - Large and non-uniform width	20	>1000	∼50	∼2	[131]
CVD on germanium	- High aspect ratio - Clean GNR/substrate interface	- Nonuniform edges - Low control on placement	8.2			∼20	[132]
SnO_2 nanoribbon mask and O_2 etching	- Reduces process steps for fabrication of GNRFETs	- Requires selection and transferring of SnO_2 nanoribbons	230		∼800	3.7	[133]
Cyclodehydrogenat of precursor monomers	- Well-defined edges - Atomically precise width	- Limited to substrates compatible with precursors	0.74		1600		[134]
Polymerization of molecular precursors	- Narrow GNRs with well-defined edges - Bandgap similar to Si	- Unpredicted length - Width variations	∼1		∼1300		[135]
Growth on SiC trenches	- Precise dimensions - Reproducible features	- Limited to SiC substrate	∼1.4		>500		[48]

Table 3.2: GNR fabrication techniques and characteristics at room temperature on typical top or back gate GNRFETs.

to impurities, especially when absorbed in sites where focused currents are localized, resulting in conduction decreasement.

Datta and colleagues present a catalytic etching process that uses thermally activated metallic nanoparticles and etching along crystallographic axes to form long layers of graphene [128]. This crystallographic etching process of graphene is potentially useful to produce atomically precise GNRs, as the metal-assisted etching process presented by Solís-Fernández and colleagues, who highlight the importance of completely controlling width, orientation and length of the GNRs by avoiding the randomness of conventional processes [49]. This large-scale technique allows the formation of highly aligned GNRs by means of a metal-assisted etching process that was used to produce 25 GNRs per μm with widths around 19 nm. The process seems to be very promising; however, the authors refer a few degrees of misalignment that produces impure AGNRs or ZGNRs after transferring the ribbon to the desired substrate.

Scanning tunneling microscope (STM) nanolithography uses the tip of a STM for breaking carbon-carbon bonds locally and allows the patterning of GNRs with well-defined crystallographic zigzag and armchair orientations [47], and widths down to 3 nm with edge roughness less than 0.5 nm, using CVD graphene transferred to Au substrates [44].

Another etching alternative is presented by Huang and co-workers in [130], where the authors use electron beam lithography and oxygen neutral beam etching on CVD graphene to fabricate GNR arrays with reduced damages to the material and low defects. The resulting array contains high-quality GNRs with width of 70 nm, which were used to fabricate a back-gated FET with a carrier mobility around 200 $cm^2V^{-1}s^{-1}$ and I_{on}/I_{off} ratio in the order of 10^3-10^4 at room temperature.

The direct-growth on dielectric substrate process presented in [131] develops nanotemplates for GNRs that well define their length and position. This method avoids the formation of ripples and defects originated after graphene is transferred to the desired substrate using other methods, and the fabrication steps used to pattern the GNRs are compatible with standard fabrication techniques for ICs. Moreover, it has the potential to manufacture GNRs in arbitrary sizes and geometries by controlling the metal-catalyst film thickness in their CVD process; thus, allowing the production of GNRs with bandgaps around 0.5-1 eV [137].

Tung and Kan present a process to pattern a side-gate GNR transistor with a 20-nm-wide channel [116]. The process uses a CVD grown graphene layer on SiO_2 and a single electron beam lithography (with negative-tone hydrogen silsesquioxane and oxygen plasma etching) step to pattern the GNR, source, drain and side gates (all made of graphene). This process could be very useful for planar (single layer) all-graphene devices, however, the etching step produces edge roughness defects that decrease the performance of such devices. Similarly, a process using double-self-aligned spacers (instead of electron beam lithography) is used in [105] to pattern GNRs for side-gate

transistors, that also results in significant edge roughness.

Directional and anisotropic CVD growing of GNRs on germanium was explored in [132]. The process allows the formation of GNRs with controlled orientation, widths below 10 nm, high aspect ratio and smooth edges (mostly armchair), but lack control over the placement of the GNR on the surface. Moreover, the authors indicate the necessity to use slow growing rates in the width direction (<5 nm/h) for improving the control over the dimensions of the GNRs.

Graphene can also be grown on diamond for usage in digital applications, as presented by Yu and colleagues in [114]. Even though the authors claim this technology could impact graphene applications in interconnects and radio frequency transistors, building graphene devices on ultrananocrystalline diamond (UNCD) and single-crystal diamond (SCD) substrates (see Figure 3.1(g)), instead of the traditional SiO_2/Si substrates, helps to improve the saturation velocity in graphene due to the larger energy of the optical phonons in diamond, and might be able to reduce the $1/f$ noise because of their lower trap density. Moreover, bottom dielectrics made with synthetic diamond can work as good heat spreaders. This technology is compatible with the CMOS process and could be used to fabricate nanoribbons if a precise control of the width and edge roughness is achievable, together with the advances in lithography; however, there are significant issues that need to be solved, including the high surface roughness (δH) of synthetic diamond, difficulty to visualize the graphene on diamond, and problems with the top-gate fabrication (since no bottom gates are possible on SCD substrates). Liao and co-workers conclude that high-field transport in GNRs on SiO_2 is limited by self-heating and the maximum current density at a given temperature is inversely proportional to the width of the GNR, which could be significantly improved if the device is built on a diamond substrate [138].

On an effort for integrating GNR and device fabrication steps, the process presented in [133] uses tin dioxide (SnO_2) nanoribbons for patterning GNRs on a Si/SiO_2 substrate containing a mechanically exfoliated graphene sheet. The SnO_2 nanoribbon works as a mask for defining the width of the GNR and for protecting the graphene from subsequent O_2 plasma treatment, which significantly affects its electrical properties. Then, gold electrodes are placed on the sample according to the desired length of the GNR, which is obtained by removing the unmasked graphene with O_2 plasma etching. The process does not require wet processes at any stage of the device fabrication, avoiding surface contamination; however, control over the width of the GNR depends on the width of the SnO_2 nanoribbon that needs to be selected and transferred.

Finally, once graphene sheets are formed, nanopores with different forms and sizes can be patterned into the sheet to obtain GNMs. Several fabrication techniques have been used for this purpose, including: i) electron beam lithography and reactive ion etching [61], ii) block copolymer lithography and O_2 plasma etching [31, 58], iii) nanoimprint lithography and O_2 plasma etching [30], and iv) nanosphere lithography [59].

3.2.2 Bottom-up manufacturing approaches

Opposite to the top-down techniques, bottom-up approaches are expected to produce GNRs with well-defined structures and controlled electronic properties. The process described by Cai and colleagues in [134] allows the formation of defect-free AGNRs on Au(111) and Ag(111) surfaces. The process consists in using a precursor monomer molecule (10,10'-dibromo-9,9'-bianthryl) to form a linear polymer after dehalogenation and C-C coupling; then, a cyclodehydrogenation process is used to obtain the AGNR. Atomically precise GNRs with different topologies and defined width and edge periphery can be obtained depending on the structure of the precursor. For instance, the authors obtained a 7-AGNR with a bandgap of 1.6 eV. Similarly, Bronner and colleagues obtain a non-aromatic polymer with bandgap of 5.25 eV, starting with the same precursor molecule. After a cyclodehydrogenation process, the authors obtain a GNR with a bandgap of 2.6 eV [139, 140]. Moreover, structurally perfect GNRs (soluble in organic solvers, such as toluene, tetrahydrofuran, and dichloromethane) can be obtained using polyphenylene precursors and an oxidative cyclodehydrogenation process [55]. Therefore, it is possible to fabricate defect-free GNRs on Au/Ag surfaces and organic solvents, but one of the main issues is to obtain the adequate precursor.

Bennett and co-workers use a similar process to fabricate GNR arrays and include a layer transfer process to build and measure FETs [141]. The authors report difficulties in obtaining GNRs with controlled orientation, width and length, which make it difficult to guarantee that the ribbons are in contact with the source and drain, leading to very low on-currents.

Kim and colleagues describe a similar approach that uses different precursor molecules, such as phenylene, naphthalene and anthracene, and cyclodehydrogenation with Iron trichloride ($FeCl_3$) to obtain GNRs [142]. The authors fabricated thin-film transistors with the resulting GNRs and the anthracene-based device presented the best performance with hole and electron mobilities of 3.25 x 10^{-2} $cm^2V^{-1}s^{-1}$ and 7.11 x 10^{-3} $cm^2V^{-1}s^{-1}$.

The synthetic bottom-up technique presented in [135] was used for manufacturing ~1-nm-wide AGNRs with high-aspect-ratio, smooth edges and bandgap of ~1.3 eV, by means of polymerization of pre-synthesized molecular precursors and cyclodehydrogenation. The GNRs can self-assemble in highly ordered structures >100-nm-long. The process is scalable and GNRs with different widths and geometries could be produced by choosing proper precursor molecules. The resulting GNR is p-type and can be deposited on many substrates, such as mica, Si/SiO_2 and Au(111). These GNRs could be used for obtaining transistors with high on/off ratios, however, the resulting devices need to be tested for finding their performance and usability in logic applications. Furthermore, these GNRs can be controllably doped with nitrogen and obtain *p-n* heterojunctions (see Figure 3.1(t)) [123], which could lead to the fabrication of transistors with *p-n-p* or *n-p-n* regions for complementary logic.

Hicks and co-workers present a novel technique to fabricate an all-graphene structure, which is a 1D metallic–semiconducting–metallic junction made entirely from graphene (see Figure 3.1(m)) [48]. This is carried out by means of a scalable technique to grow graphene on SiC that helps to improve the atomic ordering of graphene and that is able to produce semiconducting strips with a precisely defined width and consistent band structure, leading to a bandgap greater than 0.5 eV.

Another bottom-up technique used to control the electronic properties of GNRs is the chemical doping using heteroatoms –any atom other than carbon or hydrogen that replace carbon in the backbone of a molecular structure–, such as boron and nitrogen. For instance, the synthesis of nitrogen-doped graphene described in [143] allows the formation of n-type GNRs, which are required to fabricate complementary logic circuits; however, these chemically-doped GNRs need to maintain large mobilities, for which no scattering should be introduced [16].

3.3 Tunneling-effect devices

Devices whose transport characteristics rely on tunneling effect are expected to be very fast and reduce the effects of fundamental problems in traditional FETs. Tunneling field-effect transistors (TFETs) are gaining significant interest from the research community because of their favorable subthreshold swings and increased I_{on}/I_{off} ratios. According to a recent benchmark of beyond-CMOS devices, TFETs are the leading option for low-power applications with lower switching energy, but slower switching than high-performance CMOS circuits [144].

Usually, TFETs rely on band-to-band tunneling to obtain on/off states. Regular TFETs consist of an n-type source (drain), an intrinsic channel and a p-type drain (source), where switching between on/off states is based on source-drain tunneling, instead of gate modulation of carrier injection and concentration in the channel. Then, tunneling between the channel and source (drain) is controlled through the gate voltage, allowing steeper subthreshold characteristics than conventional MOSFETs (with subthreshold swing below 60mV/dec) [51]. Moreover, tunneling allows very low I_{off}, but to the expense of lower I_{on}. As discussed in [112], the n-i-p doping profile can be created by means of gate-controlled doping, that is, adding an insulating layer and a metal contact on top of the source/drain regions of the GNR and applying bias voltages to control the majority of carriers in each region. The authors tested a triple-gate TFET (see Figure 3.1(f)) using a 30-nm-wide GNR as the channel material, showing that n-type and p-type FET characteristics can be obtained by applying appropriate bias voltages to the gate, source-side gate and drain-side gate [113]. The experiment shows that the 30-nm-wide GNR is not narrow enough to have a suitable bandgap, resulting in large leakage currents when turning the device off. Then, narrower GNRs

with well-defined edges are required, having the same fabrication issues previously discussed for GNRFETs.

As observed in Figure 3.3, I_{on} is produced by electrons tunneling from source to channel when applying a gate voltage that lowers the conduction band in the channel below the Fermi level in the source. The opposite occurs when a gate voltage raises the conduction band in the channel above the Fermi level in the source; thus, I_{off} is produced by electrons tunneling from source to drain [108]. Zhang and colleagues modeled analytically TFETs with direct bandgap semiconductors, showing that it is possible to calculate optimized values of bandgap and supply voltage for fulfilling I_{on}/I_{off} ratios above 10^5; thus, for a TFET using 10 and 15-nm-long GNRs, 0.6 and 0.93 eV bandgap are required, respectively, to obtain $I_{off} = 5\text{nA}/\mu\text{m}$, using minimum supply voltage of 0.39 and 0.24 V, respectively [108].

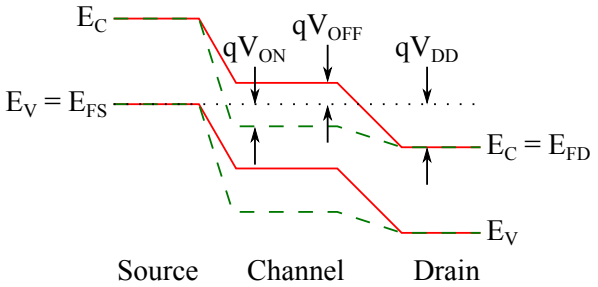

Figure 3.3: Band diagram of an n-channel TFET. Solid red and dashed green bands correspond to the off-state and on-state, respectively [108].

Another type of TFET is presented in [117]. The proposed device, known as barrier-controlled TFET (BC-TFET), uses both a channel potential barrier and tunneling between the source and the channel to obtain high I_{on}/I_{off} ratios and low subthreshold swing (but larger than 60mV/dec). In this particular case, the channel corresponds to a carbon nanotube (but structures with customizable bandgap, such as GNRs, could be used) with all-around-gate that is composed of three segments (M1, M2 and M3) with different work functions (see Figure 3.1(l)). The work function of the middle segment M2 is larger than the work function of the other segments M1 and M3 in order to have increased bandgap bending and electrical field at the source-channel junction. This causes an in-channel barrier that is controlled by the gate voltage to effectively turn on/off the device.

Mehr and colleagues present the graphene base transistor (GBT, see Figure 3.1(d)), which is based on the operation of a hot-electron transistor, but using graphene as the base electrode [145, 146, 111]. A positive emitter-base voltage is required to turn on the device, allowing carriers to tunnel from emitter to collector. This approach is estimated to have high I_{on}/I_{off} ratio and current gain, making it more suitable for high-frequency applications.

Mohamadpour and Asgari explore the performance of a resonant tunneling transistor (RTT, see Figure 3.1(b)) that uses a p^+-n-p^+ structure, with a GNR as the n-type channel of the device, whose electronic transport properties are explained with the band to band tunneling of the carriers [109]. The simple 2-state switching device might be of special interest for digital applications in long and short channels for high enough bias (the short channel device can also have many switching states and oscillate in certain conditions). In addition to that, the authors consider this RTT model to be more ideal than practical due to the difficulty to manufacture narrow GNRs with clean edges.

Ghobadi and Pourfath present a heterostructure that uses graphene-hBN layers to form a tunneling barrier, and two GNRs as drain and source, obtaining the vertical GNR-hBN FET (VTGNRFET, see Figure 3.1(i)) [104]. The authors perform simulations for devices with 3, 5 and 7 layers of hBN, achieving the best results for the VTGNRFET with 7 layers of hBN and a 1.3-nm-wide GNR, where the I_{on}/I_{off} ratio is 1.8 x 10^4 and the intrinsic subthreshold swing is 170 mV/dec, which is almost twice of a modern MOSFET, but could be improved with narrower GNRs at the expense of smaller I_{on}. Furthermore, the performance of the device can be improved by using higher-quality dielectric barrier, such as molybdenum disulfide (MoS_2) instead of hBN [147].

According to Zhao and colleagues, the symmetric TFET (SymFET, see Figure 3.1(k)) presented in [106] achieves relatively high I_{on}/I_{off} ratio, proportional to the doping potential $\triangle$E and the length of the graphene layer. This is independent of temperature, which might be useful for digital applications; however, practical devices might be too big for nanoscale logic circuits (I_{on}/I_{off} around 10^3 for a gate length of 1 μm). The bilayer pseudo-spin FET (BiSFET) presented by Reddy and colleagues in [148] is another promising approach for future logic devices which relies on the formation of electron-hole-pairs/excitons (bosons) when electrons in one layer pair with holes in the opposite layer, being very sensitive to thickness variations in the insulator layers. The physical principles of these devices are also very different compared to MOSFETs and the implementation of digital circuits are not directly related. Nonetheless, the structures are very attractive for their very low power consumption, compared to typical CMOS devices.

3.4 Ambipolar conduction devices

For many next-generation devices, such as graphene-based devices, ambipolar conduction has been demonstrated due to *p-n* symmetry (see Figure 3.4). This property is characterized by a superposition of electron and hole currents, allowing devices to be switched from p-type to n-type by changing the gate bias [149]. This could represent a major advantage compared to CMOS devices, since there is no need for gate sizing

during design and fabrication to match current magnitudes in complementary devices [121], but at the expense of high I_{off} and limited performance.

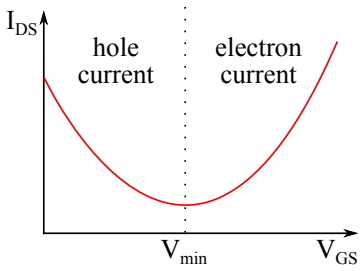

Figure 3.4: Ambipolar conduction in graphene-based transistors [149].

The wide-narrow-wide structure (see Figure 3.1(q)) presented in [121] takes advantage of the ambipolarity of GNRs and their ability to exhibit semiconducting or metallic properties, depending on the width of the material. Similarly, Hasegawa and co-workers simulate a multi-junction GNR (see Figure 3.1(o)) for bandgap engineering, consisting on two $3p + 2$ AGNRs that work as quantum wells, and a $3p$ AGNR that works as a potential barrier [119].

Moutaouakil and colleagues presented the back-gate epitaxial graphene-on-silicon FET (GOSFET, see Figure 3.1(h)), which uses the ambipolarity of graphene to create a logic inverter with a voltage gain of 0.8-2.6 and a good matching of the input and output voltage levels at room temperature [115]. Even though wide-graphene is being used (mean channel width of 10 μm), the device is very promising and requires further improvements, such as a faster on/off switching and higher gains.

Because of high off-state currents, a lot of effort is aimed to find new fabrication techniques and structures that allow the conversion to unipolar conduction, such as the process presented in [150], in which a p-type graphene FET with a tunable threshold voltage was fabricated by applying significant hole doping with titanium oxide on top of the graphene layer. Additionally, an annealing process and a silicon nitride passivation are used to convert the p-type device into n-type.

Kim and colleagues present another way to fabricate n-type semiconducting GNRs in [143]. Known as nitrogen-doped GNRs (GNR-Ns), this approach uses a bottom-up method that attempts to switch GNRs from ambipolar to n-type by doping with nitrogen. Moreover, this technique increases the electron mobility of the GNR (0.102 $cm^2\ V^{-1}s^{-1}$, two orders of magnitude bigger than the untreated GNR) and shifts its threshold voltage from 20 to -6V.

3.5 Negative resistance devices

Alternative devices, such as those based on negative differential resistance (NDR, see Figure 3.5) could be used in the design of logic circuits. According to Khatami and co-workers, the implementation of digital circuits with negative resistance properties has been limited to very low I_{on}/I_{off} ratios [103]; thus, they propose a novel structure where the top-gate covers half of the GNR channel and the back-gate the other half (see Figure 3.1(e)). The device can be tuned for achieving I_{on}/I_{off} ratios in the order of 10^5 and used in complementary logic devices.

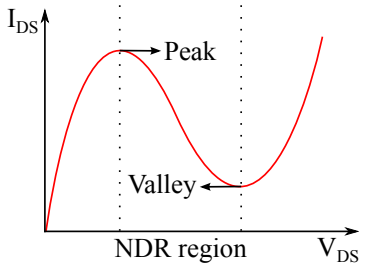

Figure 3.5: Current-voltage (I-V) characteristics of a negative differential resistance (NDR) device [103, 118, 107].

Nguyen and colleagues investigate the effects of NDR in graphene tunnel diodes, using a T-shape armchair structure (see Figure 3.1(n)) that contains two doped regions (n-type and p-type) connected by a wider transition region with small bandgap, and that seeks to increase the peak-to-valley ratio and decrease the interband tunneling sensitivity to the length of the device [118].

NDR devices can also be obtained with chemical modifications to the edges of the GNR. For instance, a nitrogen-passivated ZGNRFET was simulated in [107], showing bandgaps up to 0.6 eV and NDR in the range of 0.1-0.35 V, with a peak value that can be controlled by a gate voltage. The simulated device uses a strip of nitrogen-passivated ZGNR with n-type contacts (doped with nitrogen) and a p-type channel (doped with boron). The doping atoms are located near the center of the GNR in order to avoid adverse effects on the bandgap. The resulting currents are very low, producing I_{on}/I_{off} ratios up to 12.

3.6 Logic gates

For logic applications, graphene-based nanostructures need to have a non-zero bandgap (preferably ~1 eV, similar to Si, for reliable switching), but without decreasing its carrier mobility and being able to achieve I_{on}/I_{off} >10^6 with significant on-state current

for voltage gains $A_v > 10$; for which new device structures are very likely to be required [16]. Graphene-based inverters and other logic gates have been fabricated using wide graphene sheets (0.25 to 20 μm) in [151, 152, 153, 154]. Some of these techniques could be used to obtain novel structures for GNR-based logic circuits. A few authors reject the use of narrow graphene layers for digital applications due to the different manufacturing issues and the limitations that arise from the lowering of the carrier mobility, despite of the large on/off ratio and high channel resistance that can be obtained in GNRs [152]; however, the zero bandgap of graphene causes that these gates have high static power dissipation [153, 154]. Some of the structures described in these papers use additional processing techniques in order to obtain complementary p-type and n-type FETs for the design of logic gates [152, 153].

As previously stated, graphene-based devices still require lots of efforts for opening a big enough bandgap or designing novel circuits before being suitable for replacing silicon in very large scale electronics, such as implementing equivalent logic functionality with fewer transistors [151]. Structures such as the one presented in [151], not only deal with the high power dissipation caused by the impossibility to turn the device off, but also with the issue of having different input and output voltage levels, as also reported in [153], which would require additional design efforts and extra conditioning hardware for cascading logic gates.

According to [152], practical devices require an optimized operating bias, a good enough intrinsic voltage gain ($A = g_m/g_d > 1$), and cascading characteristic [154]. Large-area graphene logic gates, as the inverters presented in [152] and [154], have similar input and output voltage levels and a voltage gain >1; however, they still have to deal with the low on/off ratio and the high dissipation power effect. Moreover, works that take advantage of the ambipolarity of graphene, use a pair of identical FETs to construct an inverter. By doing structural modifications and employing different materials for the top-gate and dielectric layer of the device (such as aluminum and alumina, respectively), researchers have been able to reduce the operating bias and improve the voltage gain of the logic gate. After applying a positive bias ($V_{DD} > 0$), the upper and lower FETs turn into p-type and n-type, respectively, obtaining a complementary behavior [152, 154].

CMOS-like logic circuits have been simulated using SPICE models of SB-GNRFETs with symmetric and asymmetric gates, showing that the latter outperform the former because of better noise margin, less dynamic and leakage power, and better Energy-delay product (EDP) in the ideal case [110]. Moreover, the authors in [110] show that edge defects significantly reduce the transistor current in both devices, producing higher propagation delay.

All-graphene circuits exhibit promising performance metrics, however, it is necessary to solve the limitations that do not allow the fabrication of narrow GNRs with atomic precision and smooth edges. TB modeling of metallic and semiconducting AGNRFETs

is presented in [155], where the authors modeled a top-gated GNRFET using a 7-AGNR as semiconducting channel and 8-AGNRs as metallic leads (see Figure 3.1(o)); however, it is important to mention that the leads would need to be wide graphene in order to be metallic, as in Figure 3.1(q). This device shows FET-like behavior without saturation for bias voltages under 1V. When the channel is modeled with metallic-semiconducting-metallic GNRs, the resulting device can be used as an on-chip resistance with a fixed value according to the relative length of the semiconducting and metallic portions of GNR in the channel. Then, the combination of both devices is used to obtain an inverter circuit with 0.2 V noise margin and 100 nW power consumption, operating at 10 GHz.

Non-conventional topologies have also been used to develop logic circuits, such as the logic inverter based on two GOSFETs (see Figure 3.1(h)) that has a voltage gain of 0.8-2.6 and input/output matching at room temperature [115]. Additionally, Pan and Naeemi developed MUX-based graphene logic devices (see Figure 3.1(p)) that use the angular dependent transmission probability of electrons on a *p-n* junction to obtain complex circuits with graphene interconnects, whose performances are better than 15-nm-node CMOS because of smaller device area, lower output resistance, lower delay and power consumption [120].

3.7 Chapter summary

GNR-based nanodevices for logic applications still require years of development before reaching industrial production. The performance of devices up to date are still unsatisfactory for replacing silicon-based circuits, however, the increasing number of publications and patents in the field favor the expectations of using the remarkable properties of GNRs for realistic implementations in the near future, given the fact that nanoelectronic devices for logic circuits demand the purest quality of material and lowest defect densities for achieving consistent performance of devices and reliability. For this, improvements in the manufacturing processes of graphene and GNRs are mandatory. Furthermore, experiments have shown the difficulty in producing very narrow GNRs with consistent electron transport properties that could outperform silicon. For this issue, bottom-up techniques using monomer precursors have enabled the production of extremely narrow GNRs with usable bandgaps for switching devices [134, 135], but at the expense of reduced carrier mobilities.

Typical GNRFETs with exfoliated graphene have achieved the highest I_{on}/I_{off} (up to 10^7) [46], but the bandgap of the device is still too small (300 meV) and the carrier mobility is drastically reduced (~100-200 $cm^2V^{-1}s^{-1}$). Therefore, it is very likely that the performance of typical GNRFETs is not sufficient for replacing silicon devices. This will require not only improvements in the GNR manufacturing techniques, but also the design of novel nanodevices that use different physical principles for operation.

Knowing this, the required nanodevices should address the issues of manufacturing and reduced carrier mobility in narrow GNRs. TFETs and NDR-based devices are predicted to have I_{on}/I_{off} in the order of 10^5, yet they still require very narrow GNRs (1.2 and 1.7 nm) for proper operation [103, 108] and further studies on performance with defective GNRs. TFETs with tunable n-i-p profiling seem to allow an easy transition to the development of complementary logic circuits; however, the devices require wide bandgaps for reducing the leakage currents. Thereafter, hybrid structures using graphene with doped sections, functionalizations or controlled defects can result in successful devices for realistic applications, but more theoretical and experimental works are required.

Top-down and bottom-up fabrication techniques have been explored for manufacturing graphene sheets in large scale, but process variations still need to be reduced in conventional top-down processes. In this context, bottom-up techniques enable the production of highly pure GNRs with atomically precise widths and well-defined edges, however, they are limited to the substrates that are compatible with the fabrication steps, which also limit their application to practical devices. The combination of top-down patterning and bottom-up assembling should enable the development of novel processes for manufacturing high-quality nanostructures at the large scale [54], however, more theoretical and experimental studies are required for emergent materials and devices [39].

Ambipolarity of graphene results in devices with high off-state currents, even though circuit design is favored by symmetry of carriers. Researchers are conducting different experiments to fabricate unipolar graphene sheets and heterostructures that could be used to design complementary n-type and p-type graphene FETs.

Realistic applications require improved I_{on}/I_{off} ratios, where the off-state leakage current needs to be significantly reduced [26]. Current performance of GNRFETs is insufficient for switching from silicon technologies to graphene; then, the challenge is to develop novel device structures that could outperform CMOS devices by reducing leakage current and power dissipation, without increasing the production costs [16].

Consequently, researchers have been exploring alternative device structures that take advantage of tunneling and negative resistance effects that could be used to overcome fundamental issues presented by conventional approaches. TFETs with n-i-p doping profiles enable a deeper testing of the electronic transport properties of GNRs and are very promising for replacing silicon technologies [112, 113]. These structures have been probed to be possible and achieve high I_{on}/I_{off} ratios and steep subthreshold swings at the expense of changing the operational principles for obtaining effective n-type and p-type FET characteristics that would ease the design of logic circuits.

Finally, graphene-based nanoelectronics is possible according to the different device structures that have been presented in the literature, however, the biggest concern is to find a scalable, reliable and cost-effective manufacturing process that enables the

production of devices with minimum defect densities and highly reproducible features. Therefore, the goal is to overcome this issue by designing novel nanodevices that operate under different physical principles, in addition to typical field-effect devices.

4 Spin Hall Effect and Nonlocal Resistance in Adatom-Decorated Graphene

4.1 Introduction

Over the past decade, the spin Hall effect (SHE) has evolved rapidly from an obscure theoretical prediction to a major resource for spintronics [156, 157]. In the direct SHE, injection of a conventional unpolarized charge current into a material with extrinsic (due to impurities) or intrinsic (due to band structure) spin-orbit coupling (SOC) generates a pure spin current in the direction transverse to the charge current. Although the SHE was first observed only a decade ago [158, 159, 160, 161], it is already ubiquitous within spintronics as the standard pure spin-current generator and detector [156, 157]. The spin Hall angle θ_{sH}, as the ratio of generated spin Hall current and injected charge current, is the figure of merit for charge-to-spin conversion efficiency. To date, measured values of θ_{sH} range from $\sim 10^{-4}$ in semiconductors to ~ 0.1 in metals like β-Ta and β-W [157].

Concurrently, the discovery of graphene [24, 16] has ignited a considerable amount of activity, owing to its unique electronic properties and versatility for practical applications, including possible applications in spintronics [162, 163]. The intrinsically small SOC and hyperfine interactions [164, 165, 166, 167] in graphene lead to spin relaxation lengths reaching several tens of micrometers at room temperature [168, 169, 170, 171, 172, 173, 174], but simultaneously making pristine graphene inactive for the SHE [162]. On the other hand, recent nonlocal transport measurements on graphene decorated with heavy adatoms like copper, gold and silver have extracted exceptionally large values for $\theta_{\mathrm{sH}} \sim 0.2$ [175]. These reports follow prior experiments on weakly hydrogenated graphene, which showed surprisingly similar results [97] despite using light adatoms like hydrogen. The large values of θ_{sH} observed in both types of experiments have been supported by semiclassical transport theories [176, 177].

The very recent experiments [178, 179] aiming to reproduce these results have indeed confirmed a large nonlocal transport signal near the charge neutral point (CNP) of graphene which, however, appears to be disconnected from SHE physics or any other

spin-related mechanism. For example, Wang and coworkers [178] reported that Au- or Ir-decorated graphene exhibits no signature of the SHE and relate the large nonlocal resistance R_{NL} to the formation of neutral Hall currents. Kaverzin and van Wees [179] found large R_{NL} in hydrogenated graphene which was insensitive to an applied in-plane magnetic field. These authors [179] exclude valley Hall effect and long-range chargeless valley currents [1] as mediating such R_{NL}, given the absence of both its temperature dependence and broken inversion symmetry, and conclude that a nontrivial and unknown phenomenon is at play.

The presently available theories for θ_{sH} [176] or R_{NL} [180] offer little guidance on how to resolve these controversies, since they utilize semiclassical approaches to charge transport and spin relaxation which are known to break down [98, 181, 182, 183] near the CNP. Moreover, while the Kubo formula [184] offers a fully quantum-mechanical treatment that can, in principle, capture all relevant effects, its standard analytic evaluation neglects [185] terms (such as those corresponding to skew scattering from pairs of closely spaced impurities [186, 187, 188]) in the perturbative expansion in disorder strength which can become crucial for clusters of adatoms. Finally, the impact of unavoidable adatom clustering [189] on θ_{sH} is an open and important question, since adatom segregation has been shown to strongly affect spin transport properties [190, 191, 192, 193].

In this chapter, the spin Hall angle in graphene decorated with Au-adatoms is computed by using two different *numerically exact* quantum transport methodologies—the real-space Kubo formula and the multiterminal Landauer-Büttiker (LB) formula [194]. At zero temperature, both methods yield $\theta_{\mathrm{sH}} \sim 0.1$–$0.3$ for the same Au-adatom concentration n_i. However, those values require rather large $n_i \gtrsim 10\%$ and drop significantly when temperature and adatom clustering are taken into account.

Furthermore, the LB formula applied to six-terminal graphene geometry in Figure 4.1 reveals large background contributions to R_{NL} even when *SOC is artificially turned off*. They are, therefore, unrelated to SHE physics, and are also unrelated to trivial Ohmic contribution due to classical current paths [179, 180]. We show that their sign [195, 196] and scaling with the channel length L makes it possible to understand their origin. This allows us to propose a novel six-terminal graphene setup (see Figure 4.11) where such background contributions can be eliminated in order to study a purely SHE-driven R_{NL} signal.

4.2 Hamiltonian model for Au-decorated graphene

When an adatom like gold, thallium or indium is absorbed onto a graphene surface, it resides in the center of graphene carbon rings, where it can enhance the intrinsic SOC or induce Rashba SOC due to the broken inversion symmetry [197]. The minimal

(with single π orbital per site) effective tight-binding model for graphene with such adatoms is given by

$$\begin{aligned}\mathcal{H} = & - \gamma_0 \sum_{\langle ij \rangle} c_i^\dagger c_j + \frac{2i}{\sqrt{3}} V_I \sum_{\langle\langle ij \rangle\rangle \in \mathcal{R}} c_i^\dagger \vec{s} \cdot (\vec{d}_{kj} \times \vec{d}_{ik}) c_j \\ & + i V_R \sum_{\langle ij \rangle \in \mathcal{R}} c_i^\dagger \vec{z} \cdot (\vec{s} \times \vec{d}_{ij}) c_j - \mu \sum_{i \in \mathcal{R}} c_i^\dagger c_i. \end{aligned} \tag{4.1}$$

The first term is the nearest-neighbor hopping term with $\gamma_0 = 2.7$ eV. The second term is the next-nearest-neighbor hopping term, which accounts for the local intrinsic SOC enhancement by adatoms residing on the set of hexagons $\mathcal{R}$. The unit vector $\vec{d}_{kj}$ points from atom j to atom k, with atom k standing in between i and j, and $\vec{s} = (s_x, s_y, s_z)$ is the vector of the Pauli matrices. The third term is the nearest-neighbor hopping term describing the Rashba SOC which explicitly violates $\vec{z} \to -\vec{z}$ symmetry. The last term is the on-site potential μ on carbon atoms in the hexagons hosting adatoms, which simulates charge modulation induced locally around the adatom [197]. The Hamiltonian in Equation 4.1 has been employed to study spin dynamics in graphene decorated with Au-adatoms [98], and here we use the same parameters $V_I = 0.007\gamma_0, V_R = 0.0165\gamma_0$ and $\mu = 0.1\gamma_0$ fitted to first-principles calculations [197].

Figure 4.1 shows the geometry used for the calculations of bulk Kubo conductivities and multiterminal charge and spin currents. The calculations of θ_{sH} with the Kubo formula are performed using a graphene flake of the size 400 nm $\times$ 400 nm enclosed in a dashed square with periodic boundary conditions. For LB calculations, we consider full six-terminal geometry in Figure 4.1, where the central region with edges of armchair type, width $W = 50$ nm (composed of $3n+2$ dimer lines, so that its electronic structure resembles that of large-area graphene [183]) and variable distance L between the pair of leads 1 and 2 and the pair of leads 3 and 4 is attached to two armchair longitudinal leads and four transverse leads with zigzag edges and of width $W = 50$ nm. Akin to the experimental procedure [97, 175, 178, 179, 198], injecting unpolarized charge current I_1 into this measurement geometry induces $R_{\mathrm{NL}} = (V_3 - V_4)/I_1$ and $\theta_{\mathrm{sH}} = I_5^{S_z}/I_1$.

4.3 Real-space Kubo formula for spin Hall conductivity

The Kubo formula for spin Hall conductivity σ_{sH} reads [157]

$$\sigma_{\mathrm{sH}} = \frac{e\hbar}{\Omega} \sum_{m,n} \frac{f(E_m) - f(E_n)}{E_m - E_n} \frac{\mathrm{Im}\left[\langle m | J_x^z | n \rangle \langle n | v_y | m \rangle\right]}{E_m - E_n + i\eta}, \tag{4.2}$$

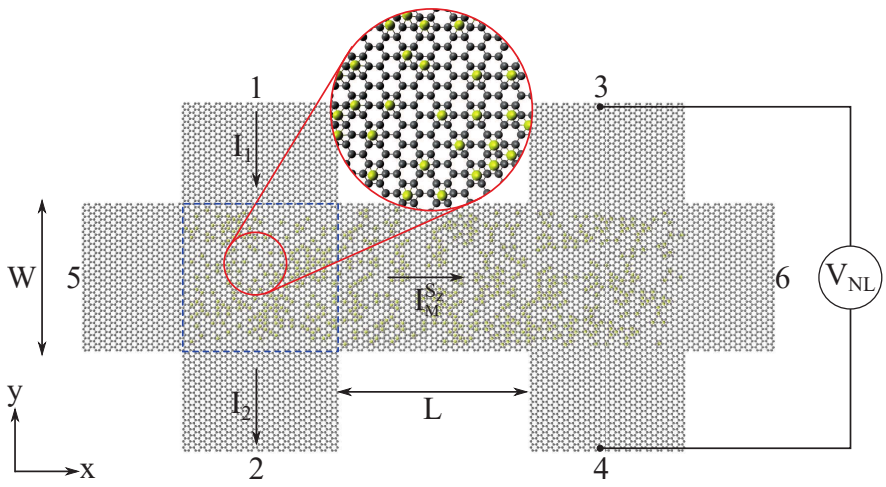

Figure 4.1: Schematic view of a six-terminal graphene employed to compute the nonlocal resistance $R_{\rm NL} = V_{\rm NL}/I_1$ and the spin Hall angle $\theta_{\rm sH} = I_5^{S_z}/I_1$. For nonlocal transport, the injected transverse charge current between leads 1 and 2 generates the longitudinal spin current $I_5^{S_z}$ in lead 5, as well as the mediative spin current $I_{\rm M}^{S_z}$ whose conversion into the voltage drop $V_{\rm NL} = V_3 - V_4$ between leads 3 and 4 generates $R_{\rm NL}$. The dashed region illustrates the sample of size 400 nm × 400 nm, with periodic boundary conditions, used for calculations of Kubo conductivities. The enlargement shows carbon atoms (black circles) and Au adatoms (yellow circles).

where v_x is the velocity operator and $J_x^z = \frac{\hbar}{4}\{s_z, v_x\}$ is the spin-current operator. The numerical evaluation of Equation 4.2 is usually made by finding the whole spectrum E_m and the full set of eigenvectors $\{|m\rangle\}$ of $\mathcal{H}$, which is a computationally expensive task. Here we develop an alternative and efficient real-space formalism by re-writing $\sigma_{\rm sH}$ as

$$\sigma_{\rm sH} = \frac{e\hbar}{\Omega}\int dxdy \frac{f(x)-f(y)}{(x-y)^2+\eta^2} j(x,y), \tag{4.3}$$

with $j(x,y) = \sum_{m,n} {\rm Im}\left[\langle m|J_x^z|n\rangle\langle n|v_y|m\rangle\right]\delta(x-E_m)\delta(y-E_n)$. This can be calculated by rescaling $\mathcal{H}, x, y$ and E into $[-1,1]$ (the corresponding variables are $h, \hat{x}, \hat{y}$ and ϵ, respectively) and by expanding $j(x,y)$ into Chebyshev polynomials $T_m(\hat{x})$ as $j(x,y) = \sum_{m,n}^{M}[4\mu_{mn}g_m g_n T_m(\hat{x})T_n(\hat{y})]/[(1+\delta_{m,0})(1+\delta_{n,0})\pi^2\sqrt{(1-\hat{x}^2)(1-\hat{y}^2)}]$, where $\mu_{mn} = {\rm Im}\{{\rm Tr}[J_x^z T_n(\mathcal{H}) v_y T_m(\mathcal{H})]\}/\Delta E^2$ and ΔE is half the bandwidth [199]. Here g_m is the filter, Jackson kernel, that minimizes the Gibbs oscillations arising in truncating the series to finite order M [199]. The trace in μ_{mn} is computed by averaging [200, 201, 202] over a small number $r \ll N$ of random phase vectors $|\varphi\rangle$, with N being the number of carbon atoms considered in the sample. Hereafter, $M = 1500$ (= 6000) for $\sigma_{\rm sH}$ (σ_{xx}), $r = 1$ and $N = 4 \times 10^6$. Similar methods have been developed for the longitudinal conductivity σ_{xx} [200, 201, 202], Hall conductivity σ_{xy} [203, 204, 205] and spin Hall

conductivity σ_{sH} [206]. The method is validated by comparing our computed σ_{sH} with analytic results [207] for clean graphene with homogeneous Rashba or intrinsic SOC.

4.4 Chebyshev-polynomial Green function method for Kubo formula

The longitudinal conductivity is calculated using a method similar to the one developed in the previous section for σ_{sH} called Chebyshev-polynomial Green function method. This method was introduced very recently by Ferreira and Mucciolo [202] to study charge transport in graphene flakes containing very large number of carbon atoms and disorder due to structural vacancies. It is inspired from the real-space order N quantum transport method pioneered in Refs. [200, 201]. The starting point is to write an exact representation of the Kubo formula for the zero-frequency conductivity

$$\sigma_{xx}(E,\eta) = \frac{2\hbar e^2}{\pi\Omega} \sum_{m,n=0}^{M} \mathrm{Im}\left[g_m(E+i\eta)\right]\mathrm{Im}\left[g_n(E+i\eta)\right]\mu_{mn}, \tag{4.4}$$

where

$$\mu_{mn} = \frac{1}{\Delta E^2}\mathrm{Tr}\left[v_x T_m(\mathcal{H}) v_x T_n(\mathcal{H})\right], \tag{4.5}$$

is given in terms of the velocity operator $v_x = [x,\mathcal{H}]/i\hbar$ and Chebyshev polynomials $T_n(\mathcal{H})$. Here Ω is the area, ΔE is half the bandwidth and η is the inelastic broadening parameter, required to define the retarded Green function $\mathcal{G}(E+i\eta)$, which has to be larger than the mean level spacing. The coefficients $g_m(E+i\eta)$ appear in the expansion of $\mathcal{G}(E+i\eta)$ in terms of first-kind Chebyshev polynomials [202]

$$\mathcal{G}(E+i\eta) = \frac{1}{E+i\eta-\mathcal{H}} = \sum_{m=0}^{\infty} g_m(E+i\eta)T_m(\mathcal{H}), \tag{4.6}$$

and are given by

$$g_m(z) = \frac{2}{i}\frac{1}{1+\delta_{m,0}}\frac{\left(z-i\sqrt{1-z^2}\right)^m}{\sqrt{1-z^2}}. \tag{4.7}$$

The most time-consuming part of this method is evaluation of the trace in Equation 4.5, which for sparse matrices representing the tight-binding effective Hamiltonian $\mathcal{H}$ can be replaced by stochastic average over r complex vectors with random phases [202]. For example, insets of Figure 4.3 show σ_{xx} for $n_i = 15\%$ concentration of Au adatoms on graphene where we used Hamiltonian matrix of size $N = 4\times10^6$ (i.e., N is the number of carbon atoms considered in the dashed square in Figure 4.1), $M = 6000$ and all results are averaged over 400 disorder configurations.

4.5 Validation of the real-space method for spin Hall conductivity

To validate our implementation of the real-space Kubo formula for σ_{sH}, we perform calculations for graphene with homogeneous spin-orbit couplings (SOCs) as described by the Hamiltonian

$$\mathcal{H} = -\gamma_0 \sum_{\langle ij \rangle} c_i^\dagger c_j + \frac{2i}{\sqrt{3}} V_I \sum_{\langle\langle ij \rangle\rangle} c_i^\dagger \vec{s} \cdot (\vec{d}_{kj} \times \vec{d}_{ik}) c_j + i V_R \sum_{\langle ij \rangle} c_i^\dagger \vec{z} \cdot (\vec{s} \times \vec{d}_{ij}) c_j. \tag{4.8}$$

Here the symbols have the same meaning as in Equation 4.1, except that V_I and V_R are nonzero on every hexagon. In the continuum limit and close to K and K' points located at the corners of the first Brillouin zone of graphene, this Hamiltonian is equivalent to the Dirac Hamiltonian

$$H(\vec{k}) = \hbar v_F \vec{\sigma} \cdot \vec{k} + \lambda_I \sigma_z s_z + \lambda_R \left(\vec{\sigma} \times \vec{s}\right)_z, \tag{4.9}$$

with $\lambda_R = 3V_R/2$ and $\lambda_I = 3\sqrt{3}V_I$.

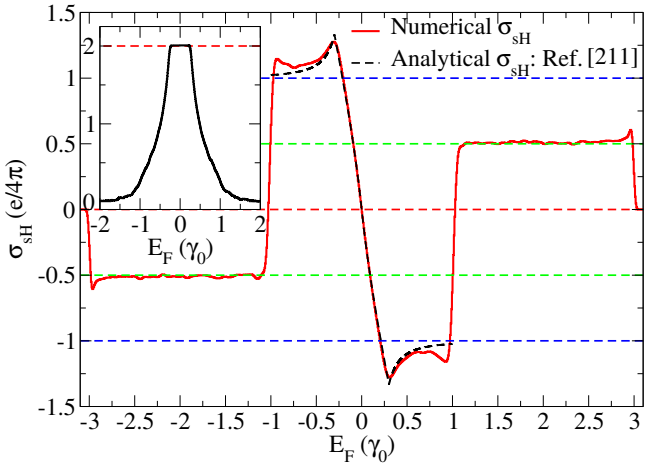

Figure 4.2: Main frame: Spin Hall conductivity σ_{sH} of graphene with homogeneous Rashba SOC obtained from our real-space Kubo formula calculations (red solid line)—with parameters $V_R = 0.1\gamma_0$, $M = 300$, $r = 100$ and $N = 1.3 \times 10^6$—is compared with analytic expression (black dashed line) in Equation 4.10. Inset: Numerically computed σ_{sH} for the case of homogeneous intrinsic SOC with parameters: $V_I = 0.05\gamma_0$, $M = 500$, $r = 50$ and $N = 32 \times 10^6$.

In the first validation test, we use Hamiltonian in Equation 4.8 with homogeneous Rashba SOC, $V_R = 0.1\gamma_0$, and zero intrinsic SOC, $V_I = 0$. For this case, an analytic

expression

$$\sigma_{\mathrm{sH}}(E) = \begin{cases} -\frac{e}{4\pi}\frac{\mathrm{sign}(E)E^2}{\left(E^2-\lambda_R^2\right)} & \text{for } |E| \geq 2\lambda_R, \\ -\frac{e}{4\pi}\frac{E(E+2\mathrm{sign}(E)\lambda_R)}{2\lambda_R(E+\mathrm{sign}(E)\lambda_R)} & \text{for } |E| < 2\lambda_R, \end{cases} \tag{4.10}$$

was obtained in Ref. [207] by starting from the Dirac Hamiltonian in Equation 4.9. The spin conductivity in two-dimensions has the same unit as spin conductance and it is naturally given in the units of spin conductance quantum, $e/4\pi$ [208]. However, to make the spin Hall angle a dimensioneless quantity, spin conductivity/conductance should be expressed in the same units as charge conductivity/conductance by replacing $e/4\pi$ with charge conductance quantum $e^2/h = (2e/\hbar)(e/4\pi)$. Figure 4.2 (main frame) compares our numerical result for σ_{sH} (red solid line) with Equation 4.10 (black dashed line). Our numerical result is in perfect agreement with Equation 4.10 up to $E \simeq 0.5\gamma_0$, despite the fact that the Dirac Hamiltonian is expected to be a good approximation only sufficiently close to charge neutral point (CNP) at $E_F = 0$. For very small Rashba SOC, $\lambda_R \ll E$, (Equation 4.10) can be rewritten as $\sigma_{\mathrm{sH}}(E) = -\mathrm{sign}(E)e/4\pi$, which is a step function explaining the shape of σ_{sH} in the scattered case (with $V_I = 0$) in Figure 4.3.

In the second validation test, we use Hamiltonian in (Equation 4.8) with homogeneous intrinsic SOC, $V_I = 0.05\gamma_0$, and zero Rashba SOC, $V_R = 0$. Such system exhibits quantum spin Hall effect (QSHE) with a gap opening in the bulk and two gapless helical edge states with opposite spin and momentum direction on each edge [96]. Consequently, the QSHE is characterized by $\sigma_{\mathrm{sH}} = 2 \times e/4\pi$ [96, 209, 207]. Figure 4.2 (inset) shows our numerical result for σ_{sH} which exhibits quantized value inside the gap, which is in full accord with QSHE phenomenology.

4.6 Spin Hall angle for different adatom distributions

Figure 4.3 shows σ_{sH} for $n_i = 15\%$ of Au adatoms distributed in a scattered (a) or clustered fashion (b), where clusters are randomly distributed islands of radius $\in [1, 3]$ nm. Although the random distribution of Au adatoms and the Rashba SOC associated with them induce scattering ($\mu = 0.1\gamma_0$ in Equation 4.1), the dependence of σ_{sH} on the Fermi energy E_F in the absence of intrinsic SOC is reminiscent of a step behavior obtained for a homogeneous Rashba SOC, with $\sigma_{\mathrm{sH}} \simeq \pm e/4\pi$ near the CNP. Adding a small intrinsic SOC, $V_I = 0.007\gamma_0 \ll V_R$, slightly changes the absolute value of σ_{sH} but preserves the step behavior. In contrast, the clustered distribution of Au adatoms suppresses the step behavior and smooths out the shape of σ_{sH} close to the CNP. The effect of intrinsic SOC is more pronounced for the clustered distribution with a more significant enhancement of σ_{sH} on both electron and hole side.

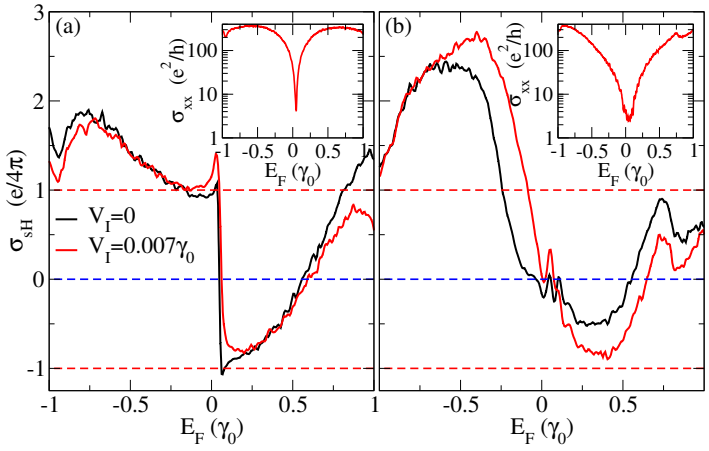

Figure 4.3: Spin Hall σ_{sH} (main frame) and longitudinal σ_{xx} (insets) conductivities for the two cases of $n_i = 15\%$ Au-adatom distributions: (a) scattered and (b) clustered, where Au islands have varying radius $\in [1, 3]$ nm. In both cases the effect of presence (red lines, $V_I = 0.007\gamma_0$) or absence (black lines, $V_I = 0$) of the enhanced intrinsic SOC within the hexagons hosting adatoms is also shown. All results are averaged over 400 disorder configurations.

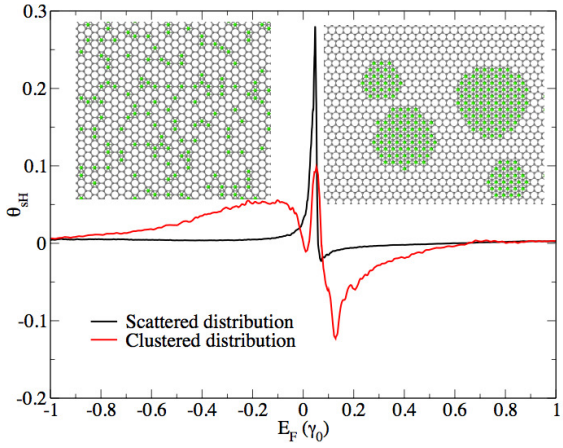

Figure 4.4: Spin Hall angle $\theta_{\mathrm{sH}} = \sigma_{\mathrm{sH}}/\sigma_{xx}$ corresponding to Figure 4.3 for scattered (black curve) and clustered (red curve) distributions of Au adatoms, which are illustrated in the insets.

The spin Hall angle $\theta_{\mathrm{sH}} = \sigma_{\mathrm{sH}}/\sigma_{xx}$ requires the additional calculation of the longitudinal conductivity σ_{xx}, which is performed using a real-space Kubo formula. Figure 4.3 (insets) shows σ_{xx} for both cases. Comparable values of σ_{xx} are obtained at the CNP, but for the scattered case σ_{xx} increases with energy faster than for the clustered case. Figure 4.4 shows θ_{sH} for $n_i = 15\%$ of Au adatoms, which are distributed homogeneously (black lines) or in clusters (red line). Remarkably, the values of θ_{sH} shown in Figure 4.4 are very large ~ 0.1 close to the CNP, which is similar to experimentally reported values [175]. At the CNP, a threefold decrease in θ_{sH} is obtained when adatoms are clustered into islands with small radius. This conclusion seems to differ from the semiclassical transport predictions, where θ_{sH} increases with the radius of adatom clusters [176], although a strict comparison would require to treat a system consisting of identical islands. At higher energies, we observe a sizable θ_{sH} for clustered adatoms, which contrasts with vanishingly small values for the scattered geometry. We finally extrapolate that, for n_i =2%–3% (as estimated in experiments [175]), θ_{sH} should range between 0.01 and 0.1. We stress, however, that our calculations represent an upper limit for experimental situations. There, the increase of the cluster size and the finite temperature can significantly decrease θ_{sH} below 0.01.

4.7 Spin Hall effect in graphene with clustering of Thallium adatoms

It is insightful to compare our predictions for the SHE in graphene decorated with Au adatoms with the onset of SHE found in the case graphene decorated with clusters of thallium (Tl) adatoms [193]. Heavy adatoms like Tl locally enhance the intrinsic SOC while generating negligible Rashba SOC [197]. For large concentration and scattered distribution of Tl adatoms, QSHE is expected [197], followed by a crossover from QSHE to SHE upon Tl clustering [193]. Figure 4.5 shows that for clustered Tl adatoms, θ_{sH} is larger than in the case of scattered Au adatoms, assuming the same concentration for both types of adatoms. Thus, high charge-to-spin conversion efficiency could be achieved by using adatoms which locally enhance intrinsic SOC, even in the presence of adatom clustering.

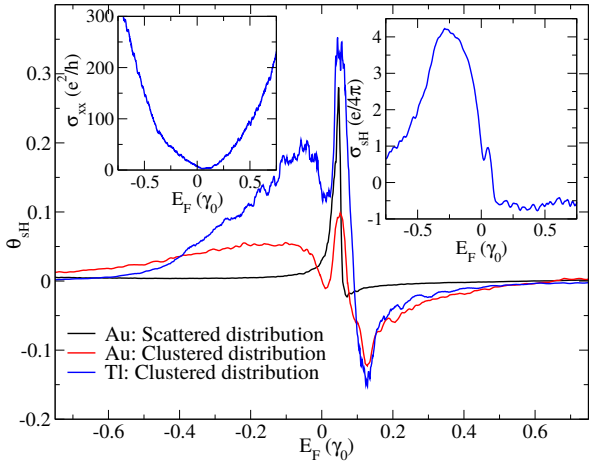

Figure 4.5: Main frame: Spin Hall angle $\theta_{\rm sH}$ for graphene with Au adatoms, which are scattered (black) or clustered (red), as well as for clustered Tl adatoms (blue curve). The concentration of both Au and Tl adatoms is $n_i = 15\%$. Insets: Conductivities $\sigma_{\rm sH}$ (right inset) and σ_{xx} (left inset) for graphene with Tl adatoms whose ratio gives $\theta_{\rm sH} = \sigma_{\rm sH}/\sigma_{xx}$ in the main frame. All curves are obtained using real-space Kubo formula calculations averaged over 400 disorder configurations.

4.8 Spin Hall angle and nonlocal resistance from multiterminal Landauer-Büttiker formula

Our numerically exact quantum transport calculations for multiterminal finite-size graphene are based on the LB formula [194]

$$I_p = \sum_q G_{pq}(V_p - V_q). \tag{4.11}$$

which relates the total charge current I_p, flowing through semi-infinite ideal (i.e., without any impurities or SOC) lead p =1–6 attached to the central phase-coherent region, to voltages V_q in all other leads. The charge conductance coefficients

$$G_{pq} = \frac{e^2}{h} \int dE\, {\rm Tr}[\mathbf{t}_{pq}\mathbf{t}_{pq}^\dagger] \left(-\frac{\partial f}{\partial E}\right), \tag{4.12}$$

are expressed in terms of the transmission matrix $\mathbf{t}_{pq}$ between transverse propagating modes within semi-infinite leads p and q. The same Equation 4.11 can be converted into the formula for total spin current $I_p^{S_\alpha}$ (which is conserved along the leads without SOC or other spin-flip mechanisms [210], as assumed in Figure 4.1)

$$I_p^{S_\alpha} = \sum_q G_{pq}^{S_\alpha}(V_p - V_q). \tag{4.13}$$

on the proviso that G_{pq} is replaced by the spin conductance coefficients

$$G_{pq}^{S_\alpha} = \frac{e^2}{h} \int dE \, \mathrm{Tr}[s_\alpha \mathbf{t}_{pq} \mathbf{t}_{pq}^\dagger] \left(-\frac{\partial f}{\partial E} \right), \tag{4.14}$$

where s_α is the Pauli matrix. The derivative of the Fermi function $(-\partial f/\partial E)$ takes into account thermal broadening effects, but inclusion of inelastic scattering at finite temperature which smooths out features of G_{pq} or $G_{pq}^{S_\alpha}$ due quantum interference effects requires to add phenomenological dephasing [183] which we do not perform in this study.

The calculation of spin and charge conductance coefficients in Equation 4.12 and Equation 4.14 was performed by using the `KWANT` package [211] which employs highly efficient and robust algorithms to calculate the transmission matrix, while being able to significantly outperform commonly used recursive GF methods [212, 213] for multiterminal devices containing large number of atoms. The `KWANT` package also avoids instabilities that occur with many commonly used algorithms (such as in dealing with the evanescent modes of complicated leads) [211].

One can apply Equation 4.11 and Equation 4.13 to the six-terminal device in Figure 4.1 by either setting the voltages V_q to find currents I_p and $I_p^{S_\alpha}$, or fix the injected current I_p and then find voltages V_q which develops as the response to it. For the analysis of experiments reported in Ref. [175] the latter approach is the most suitable, so we set injected charge current I_1 through lead 1 and current $-I_1$ flows through lead 2 while $I_p \equiv 0$ in the other four leads. We then compute voltages which develop in the leads p =3–6 in response to injected current I_1 and obtain the nonlocal resistance as the quantity which is measured directly in experiments from $R_{\mathrm{NL}} = (V_3 - V_4)/I_1$. We define the spin Hall angle for the six-terminal graphene device in Figure 4.1 or for the device in Figure 4.11 as $\theta_{\mathrm{sH}} = I_5^{S_z}/I_1$ (which is not a directly measurable quantity due to difficulty in measuring spin currents $I_p^{S_\alpha}$).

4.9 Nonlocal resistance and spin Hall angle in multiterminal graphene

In the SHE experiments [97, 175], multiterminal graphene devices are employed to measure R_{NL}, as illustrated in Figure 4.1. In such a circuit, a charge current I_1 injected from lead 1 towards lead 2 generates a nonlocal resistance $R_{\mathrm{NL}} = (V_3 - V_4)/I_1$ for the Fermi energy E_F sufficiently close to the CNP. The appearance of nonzero R_{NL}, due to a SHE-driven mechanism, is explained by charge current I_1 inducing mediative spin current $I_{\mathrm{M}}^{S_z}$ in the first crossbar in Figure 4.1 flowing in the direction $5 \to 6$, which is subsequently converted into the nonlocal voltage $V_{\mathrm{NL}} = V_3 - V_4$ by the inverse SHE in the second crossbar. We calculate the total charge I_p and spin $I_p^{S_z}$ currents and voltages

V_p in leads p =2–6 in response to injected charge current I_1 using the multiterminal LB formula [194], as implemented in `KWANT` software package [211].

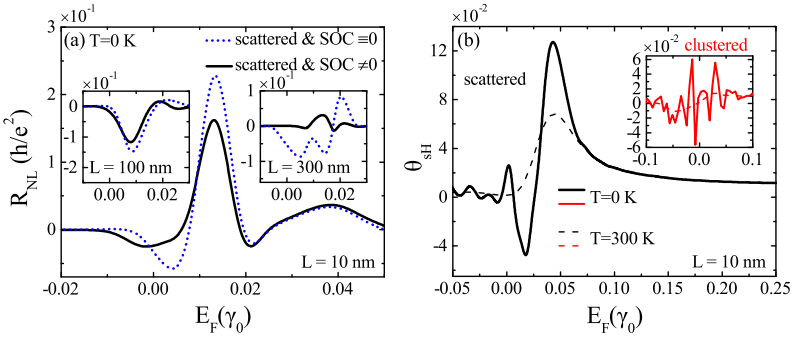

Figure 4.6: (a) Nonlocal resistances for six-terminal graphene in Figure 4.1 with n_i = 15% of scattered Au adatoms, fixed channel width $W = 50$ nm and several channel lengths: $L = 10$ nm (main frame); $L = 100$ nm (left inset); and $L = 300$ nm (right inset). Dotted lines plot $R_{\rm NL}$ when all SOC terms in (Equation 4.1) are switched off (SOC $\equiv 0 \Leftrightarrow V_I = V_R = 0$). (b) Spin Hall angle, obtained from LB formula calculations, for the same concentration of Au adatoms which are scattered (main frame) or clustered (inset). All curves are averaged over 10 disorder configurations.

The spin Hall angle—defined as $\theta_{\rm sH} = I_5^{S_z}/I_1$—is shown in Figure 4.6(b), where we confirm large values obtained from the Kubo formula, as well as the detrimental effect of clustering of Au adatoms. While both Kubo and LB formula calculations predict $\theta_{\rm sH} \simeq 0.1$ close to the CNP, thermal broadening effects included in LB formula calculations further reduce $\theta_{\rm sH}$ by up to one order of magnitude (see Figure 4.6(b)). By comparing Figure 4.6(b) with Figure 4.9, we find that the hypothetical case of homogeneous Rashba SOC, due to Au adatoms covering every hexagon in Figure 4.1, generates the SHE akin to the intrinsic one in finite-size two-dimensional electron gases [214, 209, 215, 210]. Its $\theta_{\rm sH}$ exhibits wider peak (centered at $E_F = 0.3\gamma_0$ due to doping of graphene by Au adatoms) of smaller magnitude than in the case of randomly scattered Au adatoms. Thus, adatom-induced resonant scattering [176] plays an important role in generating large extrinsic SHE.

Figure 4.6(a) shows $R_{\rm NL}$ as a function of energy and for various channel lengths L. Most notably, we find a nonzero $R_{\rm NL}$ *even when all SOC terms are switched off* ($V_R = V_I = 0$) in (Equation 4.1), while keeping random on-site potential $\mu \neq 0$ due to Au adatoms unchanged. Furthermore, we find a complex sign change of $R_{\rm NL}$ in Figure 4.6(a) with increasing channel length from $L = 10$ nm to $L = 300$ nm, which suggests the following interpretation. The total $R_{\rm NL}$ can have four contributions $R_{\rm NL} = R_{\rm NL}^{\rm SHE} + R_{\rm NL}^{\rm Ohm} + R_{\rm NL}^{\rm qb} + R_{\rm NL}^{\rm pd}$, assuming they are additive after disorder averaging. For an unpolarized charge current injected from lead 1 (i.e., electrons injected

from lead 2): $R_{\mathrm{NL}}^{\mathrm{SHE}}$ generated by combined direct and inverse SHE has a positive sign; trivial Ohmic contribution $R_{\mathrm{NL}}^{\mathrm{Ohm}}$ due to classical diffusive charge transport [180, 179] has a positive sign; $R_{\mathrm{NL}}^{\mathrm{qb}}$ is the negative quasiballistic contribution arising due to direct transmission $T_{32} \neq 0$ from lead 2 to lead 3 (see Figure 4.12), as observed previously in SHE experiments on multiterminal gold devices [195]; finally, $R_{\mathrm{NL}}^{\mathrm{pd}}$ is a positive contribution specific to Dirac materials where evanescent wavefunctions generate pseudodiffusive transport [216, 217] close to the CNP characterized by two-terminal conductance scaling as $G \propto 1/L$ even in perfectly clean samples as long as their geometry satisfies $W > L$ (see Figure 4.11).

Thus, in a device with $W > L$, such as $W = 50$ nm and $L = 10$ nm in the main frame of Figure 4.6(a), the positive sign R_{NL} is dominated by $R_{\mathrm{NL}}^{\mathrm{pd}}$, which can be larger than in the case of perfectly clean graphene in Figure 4.11 due to scattering from impurities (of uniform strength) at the CNP [218]. The negative sign of R_{NL} in the two insets in Figure 4.6(a) in the absence of SOC and for $L > W$ suggests that $R_{\mathrm{NL}}^{\mathrm{Ohm}}$ can be safely neglected in our samples due to small n_i—we estimate the mean free path $\ell = 300$–400 nm for $n_i = 15\%$, so that when diffusive transport regime sets in for $\ell > L$ the Ohmic contribution $R_{\mathrm{NL}}^{\mathrm{Ohm}} \propto \exp(-\pi L/W)$ [180, 179] is already negligible due to $L/W \gg 1$. Therefore, for $L > W$ the main competition is between $R_{\mathrm{NL}}^{\mathrm{qb}}$ with negative sign and $R_{\mathrm{NL}}^{\mathrm{SHE}}$ with positive sign, as found in the two insets in Figure 4.6(a). The existence of background contributions to R_{NL} that do not originate from the SHE, and can be even larger than $R_{\mathrm{NL}}^{\mathrm{SHE}}$, could explain insensitivity of the total R_{NL} to the applied external in-plane magnetic field observed in some experiments [178, 179].

The difficulty in clarifying the dominant contribution to R_{NL} could be resolved by detecting its sign change as a function of the channel length L in Figure 4.1. An alternative is to design a setup where $R_{\mathrm{NL}}^{\mathrm{Ohm}}$, $R_{\mathrm{NL}}^{\mathrm{qb}}$, and $R_{\mathrm{NL}}^{\mathrm{pd}}$ are negligible so that $R_{\mathrm{NL}}^{\mathrm{SHE}}$ can be isolated. We propose such setup in Figure 4.11 where adatoms are removed in the channel. When such a channel is sufficiently long, $R_{\mathrm{NL}}^{\mathrm{pd}} = 0$ due to $L > W$ and $R_{\mathrm{NL}}^{\mathrm{Ohm}}$, $R_{\mathrm{NL}}^{\mathrm{qb}} \to 0$ due to the absence of impurity scattering in the channel, so that the mediative spin current $I_{\mathrm{M}}^{S_z}$ generated by the direct SHE in the first crossbar arrives conserved [210] at the second crossbar where it is converted into V_{NL} by the inverse SHE. Indeed, Figure 4.12 demonstrates that R_{NL} and θ_{sH} in this setup are unambiguously related, since they both display a sharp peak at virtually the same E_F very close to the CNP.

4.10 Scaling of spin Hall angle with adatom concentration

In the experiments [175], the density of gold clusters of diameter ranging from 20 to 40 nm is estimated to lie within $10^{10}\mathrm{cm}^{-2}$–$10^{11}\mathrm{cm}^{-2}$. This leads to $n_i \simeq 2$–3% assuming

that clusters are two-dimensional. The values of $\theta_{\rm sH}$ obtained from the Kubo formula calculations assume larger adatom concentration $n_i = 15\%$. Because of too large mean free paths (above the micrometer) for few percent adatom densities, we cannot (within our present computational capability) reach the diffusive regime in which the Kubo conductivities could be safely estimated. An estimate of $\theta_{\rm sH}$ for much lower density is actually not straightforward because the scaling of $\sigma_{\rm sH}$ with n_i is predicted to ultimately depend on the mechanism dominating the SHE [187, 188].

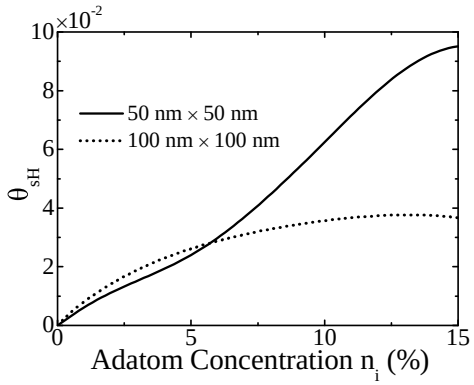

Figure 4.7: Spin Hall angle as a function of the concentration of randomly scattered Au adatoms. These results are obtained from numerically evaluation of the LB formula (see section 4.8) applied to four-terminal graphene devices whose central square-shaped region of the size 50 nm × 50 nm or 100 nm × 100 nm is attached to four semi-infinite leads of the same respective width. The values of $\theta_{\rm sH}$ are averaged over the Fermi energy interval $[-0.01\gamma_0, 0.01\gamma_0]$.

Neglecting localization effects, the scaling of longitudinal conductivity should follow the Fermi golden rule, $\sigma_{xx} \sim 1/n_i$. Similarly, the spin Hall conductivity follows $\sigma_{\rm sH} \sim 1/n_i$, but only when the skew-scattering mechanism predominates the extrinsic SHE [176, 187, 188] (e.g., as confirmed numerically in Ref. [219] for adatoms inducing Rashba SOC). As discussed in Refs. [187, 188], $\sigma_{\rm sH}$ should be dominated by a n_i-independent value for the side-jump mechanism, whereas higher order quantum interference terms between scattering paths could lead to n_i^α dependence (where $\alpha = 1, 2, ...$) [202, 187, 188, 220].

Therefore in the limit of small n_i, $\theta_{\rm sH}$ is expected to be either constant or $\propto n_i$. The value $n_i = 15\%$ used in our Kubo formula calculations lies outside the dilute adatom regime where such theories have been developed [187, 188, 219], but based on the arguments above we extrapolate that for few percent of Au adatom concentration, the maximum value should range within $\theta_{\rm sH} \simeq 0.01$–$0.1$, where the lower limit is for adatom clusters. Thus, our estimate is about one order of magnitude lower than the value reported in Ref. [175]. Finite temperatures and larger clusters will lead to even lower spin Hall angles.

Finally, a brute-force calculation of θ_{sH} for *arbitrary* adatom concentration in finite-size samples is possible using the multiterminal LB formula approach discussed in section 4.8. Figure 4.7 shows that θ_{sH} does increase with the adatom concentration in the limit of low n_i, with values agreeing with estimates made above. Comparing our results in Figure 4.7 with those in Refs. [187, 188, 219] suggests that side jump and anomalous quantum processes could dominate the physics of SHE in graphene decorated with low concentration of adatoms.

4.10.1 Nonlocal resistance for a uniform distribution of gold adatoms

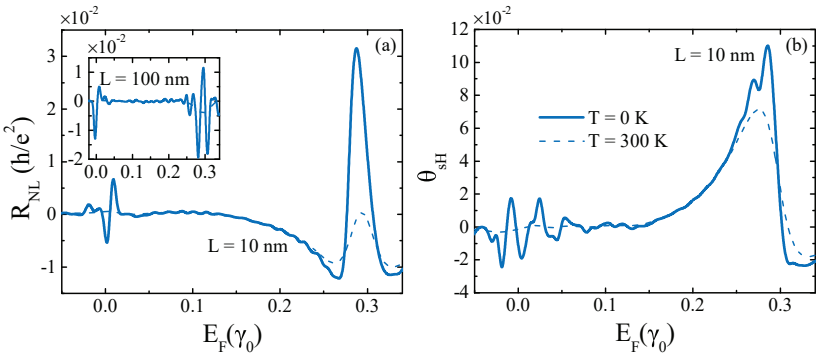

Figure 4.8: (a) Nonlocal resistance R_{NL} and (b) spin Hall angle θ_{sH} as a function of the Fermi energy for graphene with uniform distribution of adatoms where every hexagon within the central region in Figure 4.1 is covered by one gold adatom.

Figure 4.8 shows R_{NL} and θ_{sH} for the case of a completely uniform distribution of Au adatoms, where each hexagon within the central region hosts one Au adatom. Both quantities are calculated at temperatures $T = 0$ K and $T = 300$ K, where the latter includes thermal broadening effects in the LB calculations. The uniform Rashba SOC generates the intrinsic SHE in multiterminal systems, akin to the one found in multiterminal two-dimensional electron gases [210, 208, 221]. Note that the large value of the nonlocal signal and θ_{sH} is observed in Figure 4.8 away from CNP due to doping of graphene by $\mu = 0.3\gamma_0$ (chosen by viewing the central region of the device as a single large cluster) in Equation 4.1. The spin Hall angle and R_{NL} due to such intrinsic SHE are actually smaller than the same quantities shown in Figure 4.12 for scattered distribution of Au adatoms in purely SHE-driven nonlocal transport setup in Figure 4.11. This confirms the importance of resonant scattering off adatoms for enhancing the extrinsic SHE—a conclusion reached also by semiclassical transport theories [202].

4.10.2 Scaling of pseudodiffusive and quasiballistic contributions to R_{NL}

Figure 4.9 shows the scaling of R_{NL} with the length L (at fixed width W) of six-terminal pristine graphene devices when all adatoms are removed from the setup in (Figure 4.1). Such nonlocal signal, which is positive around the CNP, is specific to Dirac electron systems, like graphene [216] or metallic surfaces of three-dimensional topological insulators [217], where evanescent wavefunctions penetrate through the zero gap of the Dirac cone to generate the so-called "pseudodiffusive" transport close to CNP. The pseudodiffusive transport regime is characterized by the Ohmic-like two-terminal conductance $G \propto 1/L$ [216, 217], even though the device is perfectly clean. This mechanism provides background contribution $R_{\mathrm{NL}}^{\mathrm{pd}}$ of positive sign to total R_{NL}, as long as $W > L$, which can be further enhanced at CNP by scattering from impurities of uniform strength [218] as observed in (Figure 4.6).

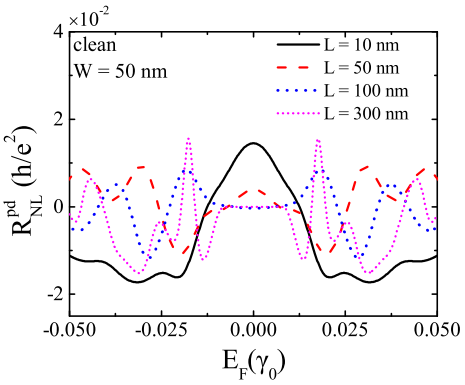

Figure 4.9: Nonlocal resistance generated in perfectly clean six-terminal graphene device where all adatoms removed. The width of the device is fixed at $W = 50$ nm, while the length between the two crossbars varies from $L = 10$ nm to $L = 300$ nm.

Figure 4.10 shows scaling of the transmission function $T_{pq} = \mathrm{Tr}[\mathbf{t}_{pq}\mathbf{t}_{pq}^{\dagger}]$ in Equation 4.12 with the length L (at fixed width W) for electron paths from lead $2 \to 3$ and lead $2 \to 4$, as well as their difference, in six-terminal graphene device in (Figure 4.1). The difference $T_{32} - T_{42}$ being positive means that more electrons arriving into lead 3 than in lead 4 will cause negative $R_{\mathrm{NL}}^{\mathrm{qb}}$ at some intermediate length scales. The slow decay of quantities in Figure 4.10 characterizing the quasiballistic transport regime can manifest as long as the channel length L is smaller than the mean free path, which we estimate for $n_i = 15\%$ concentration of adatoms to be between 300 nm and 400 nm.

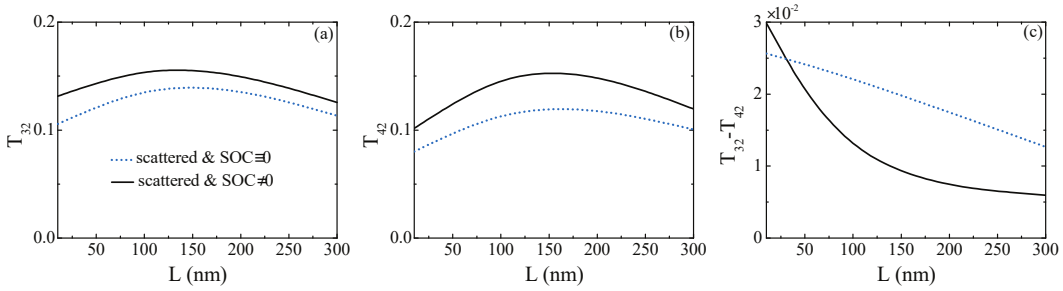

Figure 4.10: Scaling with length L of the transmission functions T_{pq} from lead q to lead p in six-terminal graphene device of width $W = 50$ nm in Figure 4.1: (a) T_{32}; (b) T_{42}; and (c) their difference, $T_{32} - T_{42}$. The central region is covered by scattered distribution of Au adatoms of concentration $n_i = 15\%$, while their SOC is switched on (solid lines) or off (dotted lines). All curves are obtained by averaging T_{pq} over the Fermi energy interval $[-0.01\gamma_0, 0.01\gamma_0]$.

4.10.3 Six-terminal graphene geometry for isolating the SHE contribution to R_{NL}

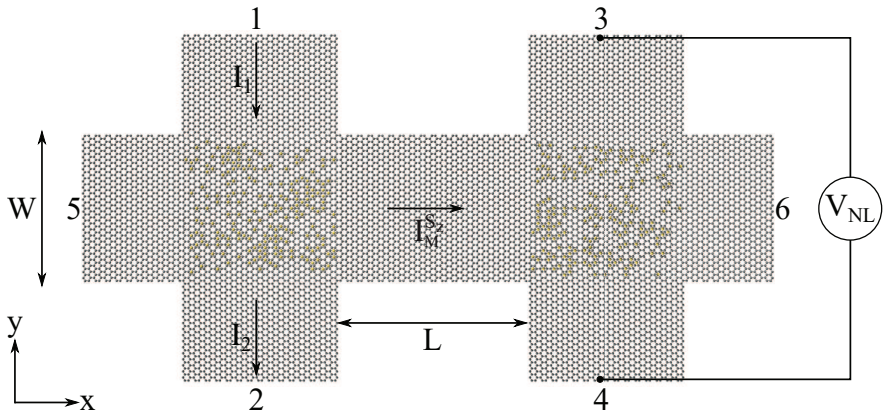

Figure 4.11: Schematic view of a six-terminal graphene geometry where adatoms are removed from the channel connecting the two crossbars in order to isolate $R_{\mathrm{NL}}^{\mathrm{SHE}}$.

Our interpretation of different contributions to $R_{\mathrm{NL}} = R_{\mathrm{NL}}^{\mathrm{SHE}} + R_{\mathrm{NL}}^{\mathrm{Ohm}} + R_{\mathrm{NL}}^{\mathrm{qb}} + R_{\mathrm{NL}}^{\mathrm{pd}}$ in Figure 4.6 and their scaling with the length L of the device motivates us to propose a setup in Figure 4.11 where adatoms are completely removed in the channel and $R_{\mathrm{NL}}^{\mathrm{SHE}}$ could be isolated and its maximum value quantified. When such ballistic channel is sufficiently long, $R_{\mathrm{NL}}^{\mathrm{pd}} = 0$ due to $L > W$ (see Figure 4.9) and $R_{\mathrm{NL}}^{\mathrm{qb}}$, $R_{\mathrm{NL}}^{\mathrm{Ohm}} \to 0$ due to the absence of adatom-induced scattering in the channel. The mediative spin current $I_{\mathrm{M}}^{S_z}$ generated by the direct SHE in the left crossbar then arrives conserved at the right crossbar where it is converted into nonlocal voltage signal V_{NL} by the inverse SHE.

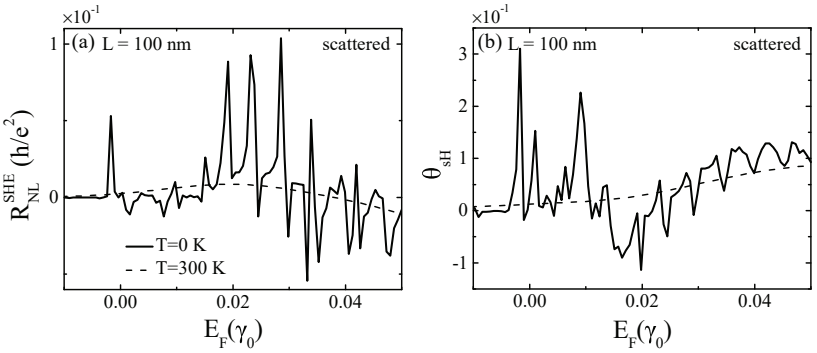

Figure 4.12: (a) Nonlocal resistance $R_{\mathrm{NL}}^{\mathrm{SHE}}$ generated solely by the combination of direct SHE (in the left crossbar) and inverse SHE (in the right crossbar) in the setup of Figure 4.11. (b) Spin Hall angle θ_{sH} for the same setup in Figure 4.11. The gold adatoms are distributed in scattered fashion with concentration $n_i = 15\%$ in each of the square regions within the two crossbars in Figure 4.11.

The maximum value of $R_{\mathrm{NL}}^{\mathrm{SHE}}$ in Figure 4.12 is still smaller than the absolute value of other contributions to the R_{NL} in (Figure 4.6) at intermediate channel lengths L. We also find that both R_{NL} and θ_{sH} exhibit a sharp peak at about the same Fermi energy located very close to the CNP, which demonstrates one-to-one correspondence between directly measurable charge transport quantity R_{NL} and indirectly inferred spin transport quantity θ_{sH}.

4.11 Chapter summary

By using the real-space Kubo formula and the multiterminal LB formula, we obtained $\theta_{\mathrm{sH}} \sim 0.1$–$0.3$ in Au-decorated graphene with large Au-adatom concentration $n_i \gtrsim 10\%$, that significantly decreases with temperature and adatom clustering. We also used a six-terminal graphene geometry for calculating R_{NL}, where we observe a non-zero signal close to the CNP, even when SOC is not present. Then, we consider the components of R_{NL} to be additive and use an alternative configuration without impurities inside the channel for getting the pure SHE-driven component, where we confirm its positive contribution to the total R_{NL}, competing with the negative quasi-ballistic contribution in configurations with $L > W$. These results are important for comparison with experiments that have also shown a large nonlocal transport signal near the CNP and could be used for designing transistors with large on/off ratios.

5 Valley Hall Effect and Nonlocal Resistance in gapped Graphene

5.1 Introduction

The recent experimental observation [1] of a sharply peaked nonlocal voltage $V_{\rm NL}$ in a narrow energy range near the Dirac point (DP) of multiterminal graphene on a hexagonal boron nitride (hBN) substrate has been interpreted [222, 223, 224, 225] as the manifestation of the valley Hall effect (VHE). In this theoretical interpretation, the injection of charge current I_3 between leads 3 and 4 of the device illustrated in Figure 5.1 generates a VH current in the first crossbar flowing from lead 1 to lead 2, which traverses the channel of length L to be converted into a nonlocal voltage $V_{\rm NL}$ between leads 5 and 6 (typically a few microns [1] away from leads 3 and 4) by the inverse VHE in the second crossbar. The corresponding nonlocal resistance $R_{\rm NL} = V_{\rm NL}/I_3$ has also been observed before near the DP in multiterminal graphene due to an external magnetic field inducing edge states in the quantum Hall regime or the Zeeman spin Hall effect at higher temperatures [226, 227, 228, 183, 93], as well as due to the spin Hall effect [97, 175, 229, 93] driven by adatom-induced spin-orbit coupling.

However, none of these mechanisms is operational in the experiment of Ref. [1]. Instead, the physics of graphene on hBN with their crystallographic axes aligned is expected to be governed by the spatial inversion symmetry breaking due to different potentials on two triangular sublattices of carbon atoms induced by the hBN substrate. This opens a gap E_g at the DP of two valleys K and K' in the band structure of an infinite two-dimensional sheet of graphene, where *ab initio* calculations have estimated $E_g \simeq 50$ meV [230]. The finite Berry curvature of opposite sign at the two valleys was predicted [222, 223, 224] to generate valley-dependent transverse conductivities, $\sigma^K_{xy} = e^2/h$ and $\sigma^{K'}_{xy} = -e^2/h$. The VH current is characterized by the VH conductivity, $\sigma^v_{xy} = \sigma^K_{xy} - \sigma^{K'}_{xy} = 2e^2/h$, and zero accompanying transverse charge conductivity, $\sigma_{xy} = \sigma^K_{xy} + \sigma^{K'}_{xy} \equiv 0$, within the gap [231]. Such chargeless currents, denoted also as "topological" [222, 223, 224] due to the involvement of the Berry curvature, are not conserved but are expected to be long-ranged when the intervalley scattering is weak.

However, σ^v_{xy} is *not directly observable*, and semiclassical transport theories [1, 224, 225] attempting to connect σ^v_{xy} to the observable nonlocal resistance—$R_{\rm NL} \propto (\sigma^v_{xy})^2 \rho^3_{xx}$ [1,

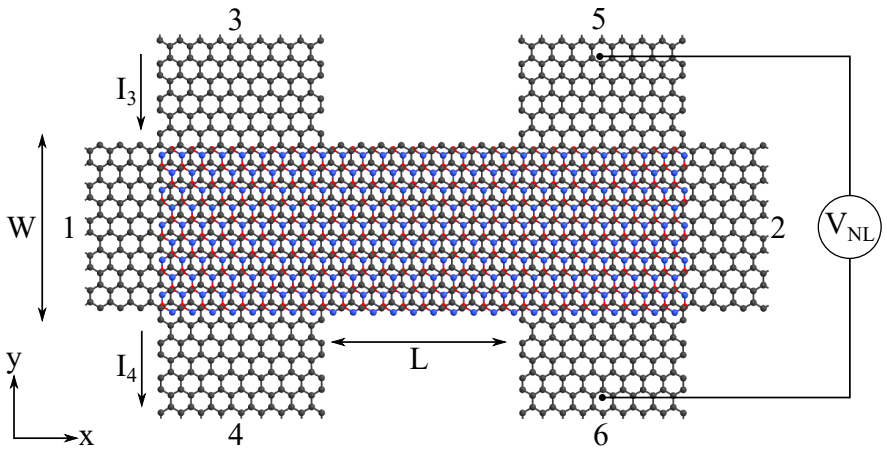

Figure 5.1: Schematic view of a six-terminal graphene, whose central region is placed onto the hBN substrate, used in the LB formula calculations of nonlocal voltage $V_{\rm NL}$ between leads 5 and 6 and the corresponding resistance $R_{\rm NL} = V_{\rm NL}/I_3$ in response to a charge current I_3 injected between leads 3 and 4. Black, blue and red circles represent carbon, nitrogen and boron atoms, respectively.

180], where ρ_{xx} is the longitudinal resistivity of the channel between the two crossbars in Figure 5.1—are not strictly applicable [232, 233] to electronic transport near the DP. This is further emphasized [234] by the presence of the gap E_g forcing electrons to tunnel through the system which is a phenomenon with no classical analog. The Landauer-Büttiker (LB) formalism [194, 235, 211], which offers a rigorous quantum transport framework to compute $R_{\rm NL}$ and has been used for nearly three decades to model nonlocal transport measurements [236, 237], yields $R_{\rm NL} \equiv 0$ near the DP in Figure 5.2(c) in multiterminal geometries when the channel length in Figure 5.1 is larger than its width $L > W$ ($L/W \approx 3.5$ in the experiments of Ref. [1]) using the same simplistic Hamiltonian employed [222, 223, 224, 231] to get $\sigma^v_{xy} \neq 0$. In geometries with $L < W$, we get $R_{\rm NL} \neq 0$ for both graphene-on-hBN channel in Figure 5.2(c) and for isolated graphene channel in Figure 5.2(b), which is trivially explained by the evanescent wave-functions propagation from the first to the second crossbar through the gap in short-channel geometries [229, 234]. The numerically exact result $R_{\rm NL} \equiv 0$ near the DP in Figure 5.2(c) is also incompatible with the interpretation [223] of $R_{\rm NL} \neq 0$ based on the picture of topological valley currents carried by the Fermi sea states just beneath the gap. Such currents are assumed to be persistent in equilibrium [223], but they would become mediative VH currents connecting the two crossbars in Figure 5.1 under the application of a bias voltage, thereby bypassing the absence of states around the DP as the fundamental reason for $R_{\rm NL} \equiv 0$ in the LB theory.

Another *long-standing puzzle* is the metallic-like resistivity $\rho_{xx} \sim 10$ kΩ observed experimentally [1] despite the expected $E_g \neq 0$ [230] in the bulk of graphene on hBN. This suggests the presence of additional conduction pathways, such as edge currents

observed very recently [238], which shunt the highly insulating state at low temperatures. However, previous theoretical studies of graphene-on-hBN wires [239, 240, 241, 242, 243] have concluded that edge states are either absent [223] or, when they appear for special types of edges like zigzag [244, 245, 90] or chiral [43, 246], they become gapped near the DP and dispersionless away from it so they are unable to carry any current [239, 240, 241, 242, 243]. The latter conclusion is reproduced in Figure 5.5 where we compute the band structure of a graphene-on-hBN wire of width $W = 50$ nm with zigzag edges using the same simplistic Hamiltonian assumed in prior theoretical studies [1, 222, 223, 224, 231, 234, 239, 240, 241, 242, 243].

In this chapter, we aim to resolve *both puzzles*—$R_{\rm NL} \equiv 0$ in Figure 5.2(c) obtained for multiterminal graphene on hBN whose bulk counterpart exhibits $\sigma^v_{xy} \neq 0$, and metallic-like ρ_{xx} despite presumed gap opening around the DP—by performing density functional theory (DFT) calculation combined with quantum transport simulations, based on both the multiterminal LB formula (Figure 5.2 and Figure 5.7) and the Kubo formula (Figure 5.3). We demonstrate that the puzzles have been generated as an artifact of too simplistic and inadequate Hamiltonian of graphene on hBN assumed in prior theoretical studies [1, 222, 223, 224, 231, 234, 239, 240, 241, 242, 243]. For example, in contrast to previously computed [239, 240, 241, 242, 243] gapped band structure for all types of graphene-on-hBN wires, the *ab initio* band structure of graphene-on-hBN wires with zigzag edges in Figure 5.7(a) does not exhibit any gap. The *ab initio* Hamiltonian combined with the LB formula yields $R_{\rm NL}$ in Figure 5.2(a) and ρ_{xx} in Figure 5.2(d) whose sharply peaked features near the DP, persisting in the presence of edge disorder, are *remarkably similar* to their counterparts measured in Ref. [1].

5.2 Hamiltonian model for gapped graphene

Since the resolution of the two puzzles crucially relies on the accuracy of the Hamiltonian for the graphene-on-hBN systems and its combination with a proper transport theory approach, we first summarize the inconsistencies in previous theoretical analyses. A putative "standard model" [1, 222, 223, 224, 231, 234, 239, 240, 241, 242, 243] of graphene on hBN is TBH defined on a honeycomb lattice with the lattice constant $a_0 \approx 2.46$ Å and a single p_z orbital per each carbon atom

$$\hat{H}_{\rm TB} = \sum_i \varepsilon_i \hat{c}_i^\dagger \hat{c}_i - \gamma_0 \sum_{\langle ij \rangle} \hat{c}_i^\dagger \hat{c}_j. \tag{5.1}$$

Here $\hat{c}_i^\dagger$ ($\hat{c}_i$) creates (annihilates) electron on site i; the on-site energy $\varepsilon_i = \pm\Delta$, which generates a gap $E_g = 2\Delta$, is positive on one atom of the graphene unit cell and negative on the other one to take into account the staggered potential induced by the hBN substrate while neglecting any reorganization of chemical bonding or change in the atomic order of the graphene and hBN layers; and hopping $\gamma_0 = 2.7$ eV is nonzero only between nearest-neighbor (NN) carbon atoms as denoted by $\langle ij \rangle$.

5.3 Nonlocal resistance and valley Hall effect in multiterminal graphene-on-hBN

We use $\hat{H}_{\rm TB}$ from Equation 5.1 with $\Delta = 29$ meV [230] to obtain $R_{\rm NL}$ in Figure 5.2(c) for a graphene-on-hBN wire with zigzag edges as the channel whose band structure is shown in Figure 5.5(f).

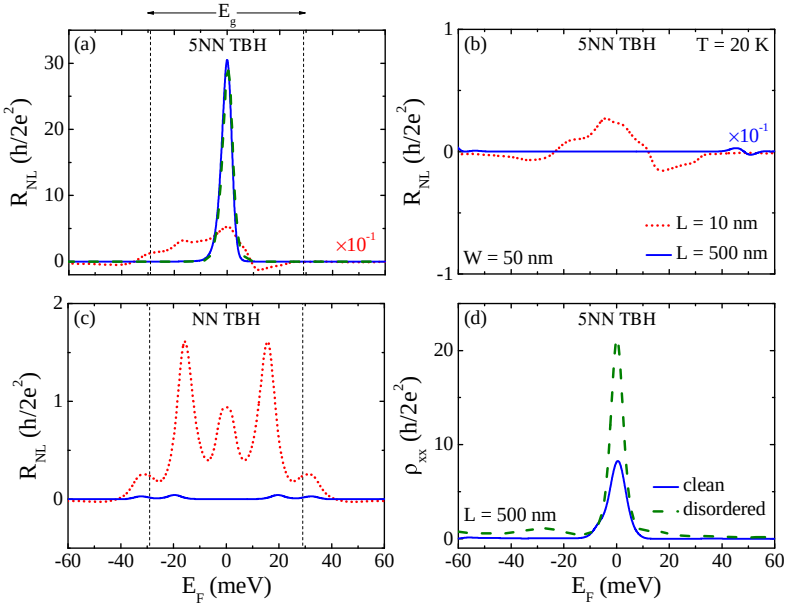

Figure 5.2: (a)–(c) Nonlocal resistance $R_{\rm NL}$ in the six-terminal device in Figure 5.1, of width $W = 50$ nm and length $L = 10$ nm or $L = 500$ nm, computed by the multiterminal LB formula. We use an *ab initio* 5NN TBH describing the graphene-on-hBN channel in (a) or isolated graphene in (b), while in panel (c) we use the NN TBH in Equation 5.1 assumed in previous theoretical studies [1, 222, 223, 224, 231, 234, 239, 240, 241, 242, 243]. Panel (d) shows longitudinal resistivity ρ_{xx} for the clean and edge-disordered channel of length $L = 500$ nm described by the 5NN TBH, where the latter is averaged over ten samples. The same type of disorder is used to compute $R_{\rm NL}$ (dashed line) in panel (a). The temperature is set at $T = 20$ K, as in the experiment of Ref. [1].

For analytical calculations, the long wavelength limit of $\hat{H}_{\rm TB}$ is preferred, $\hat{H}_{\rm D} = \hbar v_F(\hat{\boldsymbol{\sigma}}\cdot\hat{\mathbf{k}}) + \Delta\hat{\sigma}_z$, which is a gapped Dirac Hamiltonian describing each of the two valleys separately. Here $v_F = (\sqrt{3}/2)a_0\gamma_0$ is the Fermi velocity, $\hat{\boldsymbol{\sigma}} = (\hat{\sigma}_x, \hat{\sigma}_y)$ is the vector of the Pauli matrices corresponding to the sublattice degree of freedom and $\hbar\hat{\mathbf{k}}$ is the momentum operator. Unlike $\hat{H}_{\rm D}$, more general $\hat{H}_{\rm TB}$ describes both valleys and can,

therefore, be used to capture the intervalley scattering effects on transport quantities, as illustrated in Figure 5.3(a) where short-range disorder diminishes σ^v_{xy}.

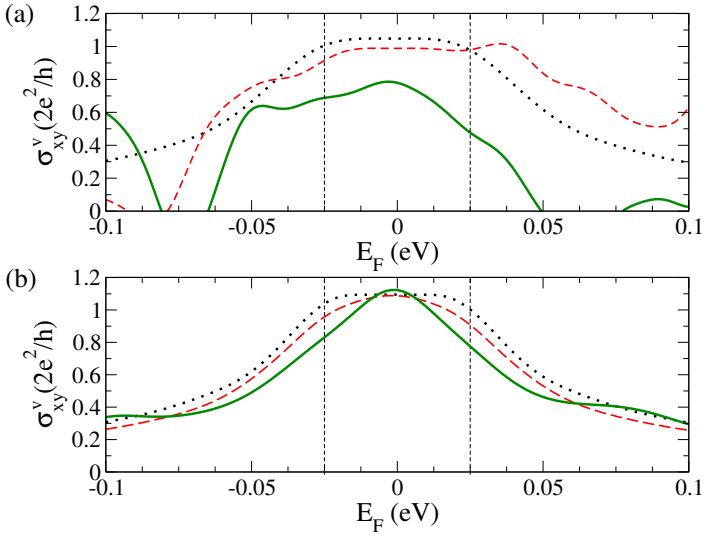

Figure 5.3: Zero-temperature σ^v_{xy}, computed by the Kubo-Bastin formula, for a 2048×2048 supercell of graphene on hBN described by: (a) NN TBH in Equation 5.1; or (b) *ab initio* Wannier TBH. The dotted black line plots the clean case; the red dashed line includes long-range disorder (with range $\xi = 10 \times a/\sqrt{3}$ and strength $U_p = 1.275$ eV in the model of Ref. [247]); and the solid green line includes short-range disorder (with range $\xi = 0.1 \times a/\sqrt{3}$ and strength $U_p = 1.275$ eV in the model of Ref. [247]). The impurity concentration is 30% for both types of disorder.

The seminal prediction [222] for VHE in gapped graphene is based on the semiclassical transport theory for wave-packets of Bloch states with dispersion $\epsilon_{\mathbf{k}}$ whose velocity $\mathbf{v_k} = \frac{1}{\hbar}\partial\epsilon_{\mathbf{k}}/\partial\mathbf{k} + d\mathbf{k}/dt \times \mathbf{\Omega_k}$, acquires an anomalous term due to the Berry curvature $\mathbf{\Omega_k}$ becoming nonzero near the apex of each valley in gapped graphene. Since $\mathbf{\Omega_k}$ points in opposite directions in the two valleys, electrons belonging to two valleys will be separated in the opposite transverse directions in the presence of an applied electric field $\mathbf{E}$ required to accelerate electrons according to $\hbar d\mathbf{k}/dt = e\mathbf{E}$. This gives rise [222] to $\sigma^K_{xy} = \frac{e^2}{\pi\hbar}\int d^2k\, f(\varepsilon_{\mathbf{k}})\Omega(\mathbf{k})$, where $f(\varepsilon_{\mathbf{k}})$ is the Fermi function forcing the integration over the whole Fermi sea—from the bottom of the band to the Fermi level E_F.

However, it has already been pointed out in Ref. [234] that nonzero $\mathbf{E}$ *cannot* appear in the linear-response limit of the multiterminal LB formula [194, 235, 211], $I_p = \frac{2e^2}{h}\sum_q G_{pq}(V_p - V_q)$, which relates the total charge current I_p in lead p to voltages V_q in all other leads via the conductance coefficients $G_{pq} = \int dE\,(-\partial f/\partial E)T_{pq}(E)$ expressed in terms of the transmission functions $T_{pq}(E)$ [194, 235, 211] which do not include any effect of the applied $\mathbf{E}$. Here the derivative of the Fermi function confines the integration to a shell of states of width $\sim k_BT$ around E_F. We use the multitermi-

nal LB formula implemented in the `KWANT` package [211, 248] to compute $V_{\mathrm{NL}} = V_5 - V_6$ and R_{NL} in response to an injected current $I_3 = -I_4$ [229] while keeping $I_p \equiv 0$ in the other four leads. The same procedure allows us to compute $\rho_{xx} = R_{4\mathrm{T}}W/L$ from the four-terminal resistance $R_{4\mathrm{T}} = (V_3 - V_4)/I_1$ obtained by injecting a current $I_1 = -I_2$ into the device in Figure 5.1 with leads 5 and 6 removed and the voltage probe condition imposed, $I_3 = I_4 = 0$.

To accommodate nonzero $\mathbf{E}$, one could employ the multiterminal LB formula at finite bias voltage [249] where the self-consistent electric potential is required to ensure the gauge invariance [250] of the current-voltage characteristics. However, experiments measuring R_{NL} are carefully kept [1] in the linear-response regime in order to avoid heating of the device and the ensuing thermoelectric effects that can add large spurious contributions [227] to R_{NL}.

5.4 Valley projection scheme in the Kubo-Bastin formula calculations

The semiclassical arguments for the origin of σ^v_{xy} can be replaced by a rigorous quantum transport theory based on the Kubo-Bastin formula [231, 251] which requires to first obtain [202, 205, 219] the velocity operator $\hat{\mathbf{v}}$ for the chosen Hamiltonian. The physical consequences of the equation of motion for $\hat{\mathbf{v}} = v_F\hat{\boldsymbol{\sigma}}$ defined by $\hat{H}_{\mathrm{D}}$ [231]

$$\frac{d\hat{\mathbf{v}}}{dt} = \frac{1}{i\hbar}[\hat{\mathbf{v}}, \hat{H}_{\mathrm{D}}] = 2v_F^2(\hat{\mathbf{k}} \times \hat{\boldsymbol{\sigma}}) - \frac{E_g}{\hbar}\hat{\mathbf{v}} \times \mathbf{e}_z, \tag{5.2}$$

are extracted by finding the expectation value of the acceleration operator $d\hat{\mathbf{v}}/dt$ in a suitably prepared wave-packet [214]. The wave-packet can be injected with an initial velocity into the graphene wire where it propagates in the absence of any electric field [214]. The first term in Equation 5.2 then causes zitterbewehgung motion of the center of the wave-packet, while the second one acts on it like a Lorentz force due to an effective magnetic field in the direction of the unit vector $\mathbf{e}_z$ perpendicular to the graphene plane. For electrons from the K' valley, $\hat{v}_y = -v_F\hat{\sigma}_y$, leading to opposite direction of the Lorentz force and, therefore, $\sigma^K_{xy} = -\sigma^{K'}_{xy}$ [231].

Figure 5.3(a) shows σ^v_{xy}, computed using the Kubo-Bastin [251] formula combined with a valley-projection scheme [93, 205, 219], for a bulk graphene on hBN described by the $\hat{H}_{\mathrm{TB}}$ in Equation 5.1 which is either clean or contains long- or short-range disorder as additional terms in the on-site energy ε_i (using the same model as in Ref. [247]). In the clean limit, we confirm [231] that $\sigma^v_{xy} = 2e^2/h$ is quantized inside the gap in Figure 5.3(a), as well as that the Fermi sea states just beneath the gap provide the main contribution to it [223]. For long-range disorder which does not mix valleys, σ^v_{xy} in Figure 5.3(a) remains close to the clean limit within a smaller energy range

than E_g due to disorder-induced broadening of the states. On the other hand, σ^v_{xy} in Figure 5.3(a) diminishes to a small value for valley mixing short-range disorder.

The valley-projection scheme [93, 205, 219] employed for numerically exact calculations using the Kubo-Bastin formula in Figure 5.4 relies on the artificial separation of the Brillouin zone of graphene into a K and K' regions with different chirality. This feature can be exploited to speed up the valley Hall conductivity calculation, where the main source of noise comes from the stochastic calculation of the trace [205, 219, 202]. These fluctuations are random and as such do not obey any symmetry of the system. As shown in Figure 5.4, when computing the Hall conductivities, σ^K_{xy} and $\sigma^{K'}_{xy}$, for each of the two valleys a lot of such noise is generated. But once we compute the valley Hall conductivity, $\sigma^v_{xy} = \sigma^K_{xy} - \sigma^{K'}_{xy}$, this noise is filtered away because it does not have opposite chirality. Nonetheless, when we incorporate disorder that connects the two valleys, such property is removed and one should proceed to remove these fluctuations by averaging over disorder configurations.

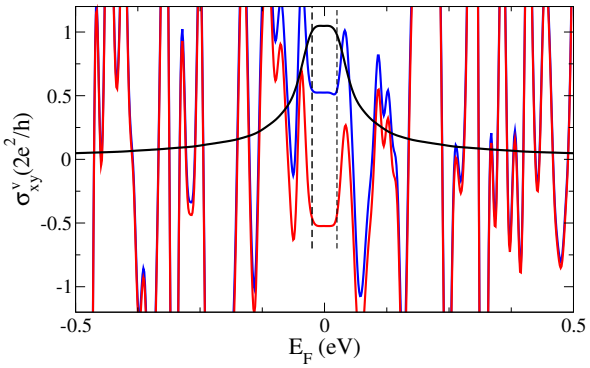

Figure 5.4: Hall conductivity computed in K (red line) and K' (blue line) regions of the BZ of pristine graphene whose difference gives the valley Hall conductivity (black line). These results are obtained by computing the Kubo-Bastin formula for 2048×2048 supercell of graphene on hBN described by the phenomenological NN TBH in Equation 5.1.

5.5 *Ab initio* versus tight-binding band structure of graphene-on-hBN wires with zigzag edges

Since the multiterminal LB formula yields $R_{\rm NL} \equiv 0$ near the DP in Figure 5.2(a) for the same $\hat{H}_{\rm TB}$ for which the Kubo-Bastin formula produces quantized σ^v_{xy} in Figure 5.3(a), we investigate the *ab initio* band structure of graphene-on-hBN wires using local-orbital pseudopotential DFT, as implemented in the `ATK` [252] and `OpenMX` [253, 254] packages, whose Kohn-Sham Hamiltonian can be also be easily combined with the LB

formula [255, 77]. Such calculations produce the band structure of graphene-on-hBN wires shown in Figure 5.7(a) and Figure 5.5(a)–(c), which *drastically differs* from the band structure in Ref. [239] or in Figure 5.5(f) produced by the "standard model" TBH in Equation 5.1. We assume a stacking where one C atom is over a B atom and the other C atom in the unit cell of graphene is centered above the hBN hexagon, which is the energetically most stable configuration found in DFT calculations [230].

The diagonalization of the Kohn-Sham Hamiltonian in DFT to obtain the *ab initio* band structure proceeds by approximating the Hilbert space of all single-electron eigenfunctions with a finite set of basis functions. A popular basis set is plane-waves (PWs), where varying the energy cutoff makes it possible to improve the basis systematically. The linear combination of atomic orbitals (LCAO) basis sets require more tuning, however, they allow us to treat supercells containing large number of atoms with $O(N)$ computational complexity [256] and they simplify the *ab initio* quantum transport calculations, based on the LB formula combined with the DFT Hamiltonian [255, 77], where one has to spatially separate the system into a central region and semi-infinite leads illustrated by Figure 5.1.

A commonly used minimal LCAO basis set for graphene systems is composed of single-zeta polarized (SZP) pseudoatomic orbitals on C atoms [257]. However, when applied to wires made of graphene on a hexagonal boron nitride (hBN) substrate—together with double-zeta polarized (DZP) orbitals on B and N and single-zeta orbitals on edge passivating H atoms—this leads to the valence band of hBN being pushed toward the Fermi level E_F suggesting incorrectly conduction through the hBN substrate. Therefore, we first perform DFT calculations for graphene-on-hBN wires with zigzag edges of width $W = 13$ nm using a dense LCAO basis set in the `OpenMX` package which consists of `s2p1` orbitals on H atoms and `s2p2d1` on C, B and N atoms with cutoff radius 5.0 and 7.0 a.u, respectively. This gives a reference band structure shown in Figure 5.5(a). The same is reproduced by the medium SG15 basis set [258] implemented in the `ATK` package [252], as shown in Figure 5.5(b). In both `OpenMX` and SG15 basis set calculations we use the Perdew-Burke-Ernzerhof (PBE) parametrization of the generalized gradient approximation (GGA) for the exchange-correlation (XC) functional and norm-conserving pseudopotentials for describing electron-core interactions.

However, the DFT Hamiltonian matrices represented in `OpenMX`, and even in the smaller SG15 basis sets, are still too large for computationally efficient quantum transport simulations. Therefore, we perform additional calculation using DZP orbitals on all C, B, N, and H atoms and the Perdew-Zunger parametrization of the local density approximation (LDA) for the XC functional, which leads to a reasonably small Hamiltonian matrix. The corresponding band structure in Figure 5.5(c) matches the band structure obtained in Figure 5.5(a) and Figure 5.5(b) in the energy interval around the DP at $E - E_F = 0$ of interest to quantum transport studies. The same match (not shown) remains valid for $W = 50$ nm wires used as the channel in the device in Figure 5.1, for which R_{NL} is calculated in Figure 5.2(d).

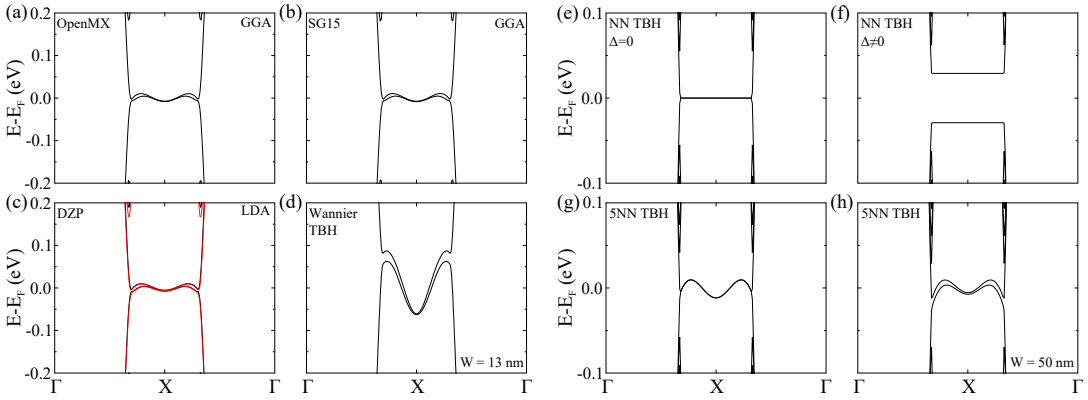

Figure 5.5: (a)—(d) *Ab initio* band structure of graphene-on-hBN wires of width $W = 13$ nm with zigzag edges obtained by diagonalizing: (a) DFT Hamiltonian in the LCAO basis generated by the `OpenMX` package [253, 254]; (b) DFT Hamiltonian in the SG15 [258] LCAO basis; (c) DFT Hamiltonian in the basis of DZP orbitals on C, B, N and H atoms; (d) *ab initio* Wannier TBH constructed from PW DFT calculations via the `VASP` package for bulk graphene-on-hBN. The red dashed line in panel (c) plots the band structure obtained from the *ab initio* 5NN TBH whose parameters are given in Figure 5.6. (e)–(h) Tight-binding band structure of graphene-on-hBN or isolated graphene wires of width $W = 50$ nm with zigzag edges: (e) isolated graphene wire described by the phenomenological NN TBH in Equation 5.1 with $\varepsilon_i = 0$; (f) graphene-on-hBN wire described by the phenomenological NN TBH in Equation 5.1 with $\varepsilon_i = \pm 29$ meV; (g) isolated graphene wire described by the *ab initio* 5NN TBH with parameters in Figure 5.6; and (h) graphene-on-hBN wire described by *ab initio* 5NN TBH with parameters in Figure 5.6.

Figure 5.5(e)–(h) plot the band structure obtained by diagonalizing the phenomenological and *ab initio* TBHs for graphene-on-hBN or isolated graphene wires with zigzag edges of width $W = 50$ nm, which serve as the channel between two crossbars in the device in Figure 5.1. The nonlocal resistances $R_{\rm NL}$, corresponding to channels in Figure 5.5(e)–(h), are given in Figure 5.2(a)–(d). The band structure in Figure 5.5(f) obtained from the phenomenological NN TBH in Equation 5.1 is gapped and it was predicted previously in Ref. [239]. The flat bands connecting the two valleys at the gap boundary correspond to edge states, and they are inherited from the band structure of an isolated graphene wire with zigzag edges shown in Figure 5.5(e). That is, simulating the presence of hBN by using the staggered on-site potential $\varepsilon_i = \pm\Delta$ in the NN TBN in Equation 5.1 simply opens the gap between the flat bands in Figure 5.5(e) to produce the band structure in Figure 5.5(f). Both of these band structures, which are an artifact of the phenomenological NN TBH [259, 246] or continuous Dirac Hamiltonian with appropriate boundary conditions [260], *do not* generate edge currents [261]. This *contradicts* experimental observation of edge currents near the DP in isolated graphene

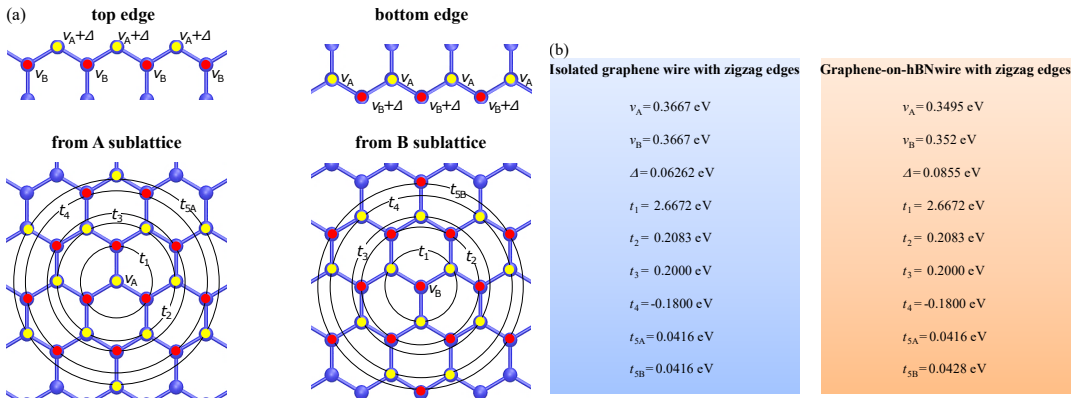

Figure 5.6: (a) Schematic view of up to fifth nearest neighbor hoppings t_n between p_z orbitals on each C atom, on-site potential $\varepsilon_i = \nu_A$ or $\varepsilon_i = \nu_B$ and additional term in the on-site potential Δ for edge C atoms required to reproduce the DFT-computed band structure of an isolated graphene wire or graphene-on-hBN wires with zigzag edges, as illustrated in Figure 5.5(c). (b) Numerical values of parameters introduced in panel (a).

wires with zigzag edges [244] or in graphene-on-hBN wires where some zigzag segments are present [262]. These edge currents [262] are responsible for the metallic-like resistivity $\rho_{xx} \sim 10$ kΩ observed [1] in multiterminal graphene-on-hBN devices.

Therefore, in order to replace the phenomenological NN TBH with an accurate TBH with long-range hoppings, which is required for LB- or Kubo formula-based quantum transport calculations on systems containing large number ($\sim 10^6$) of carbon atoms, our first approach is to transform [263] the DFT Hamiltonian in the PW basis computed by the `VASP` package [264, 265] to a basis of maximally localized Wannier functions [263, 266] where we consider p_x, p_y and p_z orbitals on C atoms for bands around E_F of bulk graphene-on-hBN. In the `VASP` calculations we use a plane-wave cutoff energy 500 eV; PBE parametrization of GGA for the exchange-correlation (XC) functional; and the projector augmented wave method for describing the electron-core interactions [267, 268]. The k-point mesh of size $8 \times 6 \times 1$ is used for the Brillouin zone (BZ) sampling of a rectangle unit cell consisting of four C atoms. The *ab initio* Wannier TBH is useful for the Kubo formula calculations on squares with periodic boundary conditions, as employed in Figure 5.3(b).

While the Wannier TBH reproduces the band structure of bulk graphene on hBN, it generates a much higher group velocity $\partial\varepsilon(k_x)/\hbar\partial k_x$ of edge state bands near $E - E_F = 0$ in Figure 5.5(d) when compared to those in Figure 5.5(a)–(c) obtained from the LCAO pseudopotential DFT calculations. This is because the `VASP` calculations for bulk graphene on hBN used to construct the Wannier TBH did not include information about the edge passivating H atoms. We resolve this issue by constructing another

ab initio TBH via least square fitting of the bands around $E - E_F = 0$, as shown in Figure 5.5(c). This TBH includes up to fifth NN hoppings and on-site potentials which are explained in Figure 5.6. The *ab initio* 5NN TBH is used to compute R_{NL} in Figure 5.2(c) and (d), as well as the two-terminal conductance in Figure 5.3(c).

5.6 Conductance and local density of states in clean and disordered graphene-on-hBN wires with zigzag edges

When the DFT Hamiltonian for a wire—composed of C, B and N atoms, as well as H atoms passivating dangling bonds along the zigzage edges—is combined with the LB formula within the `ATK` [252] package, we obtain its zero-temperature conductance $G_{21} = 5 \times 2e^2/h$ shown in Figure 5.7(b) at the DP at $E - E_F = 0$. This value is insensitive to the bulk nanopore in Figure 5.7(d), signifying edge current transport, but it is reduced to $G_{21} \lesssim 2e^2/h$ in the presence of the edge vacancy shown in Figure 5.7(e) or quantum interferences generated by the edge vacancies in series shown Figure 5.7(f). The valley-polarized states [269] above and below $E - E_F = 0$ are bulk states since G_{21} is reduced at those energies by the presence of the bulk nanopore in Figure 5.7(d). The low-energy dispersive edge state are visualized by plotting the local density of states (LDOS) in Figure 5.7(c), which is peaked near the edges but it remains nonzero even in the bulk [246]. This is quite different from topologically protected edge states in quantum (ordinary [93], spin [270, 193] and anomalous [271]) Hall insulators where LDOS in the bulk vanishes. The spatial profile of the edge currents in Figure 5.7(e)–(f) survives even in the presence of edge disorder which breaks the graphene-on-hBN wire into short zigzag-edge segments.

For comparison with Figure 5.7, we provide identically calculated panels of Figure 5.8 using the LCAO pseudopotential DFT whose Kohn-Sham Hamiltonian is represented in the basis of DZP orbitals on C, B, N and H atoms, LDA is used for XC functional and the energy mesh cutoff for the real-space grid is chosen as 75.0 Hartree. Careful comparison shows that the hBN substrate slightly changes the spatial extension of the edge states. This helps to make conductance in Figure 5.7(b) more resilient to quantum interference effects in the case of a series of edge vacancies in Figure 5.8(f), thereby evading antiresonance in the conductance at the DP in Figure 5.8(b).

We note that even in systems with topological invariants in the bulk band structure, such as Chern number $\mathcal{C}$ which counts the number of metallic edge states, zigzag edges of the honeycomb lattice play a special role [271] due to their ability to modify the energy-momentum dispersion and the corresponding conductance carried by edge states. Nevertheless, quantized conductance $\mathcal{C} \times 2e^2/h$ survives disorder [271], while no such topological protection exists in the case of isolated graphene or graphene-on-hBN

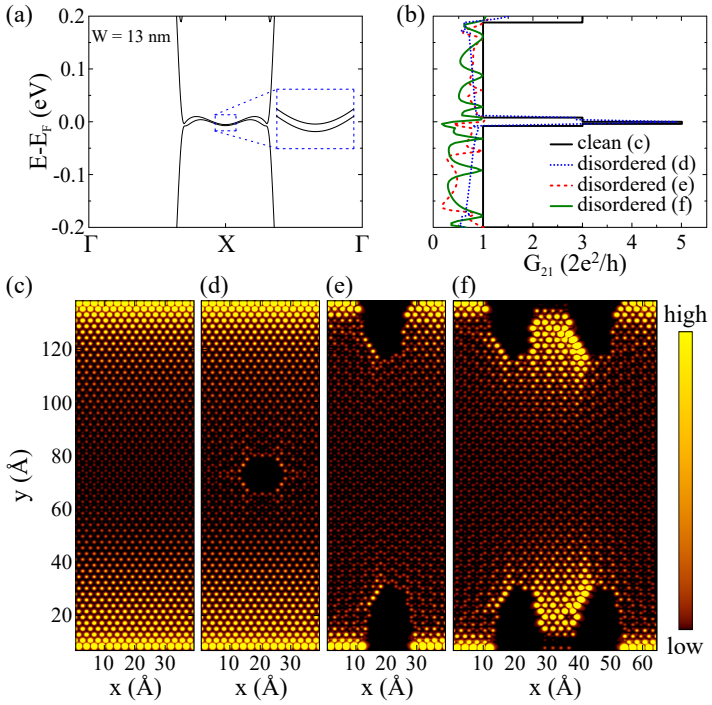

Figure 5.7: (a) *Ab initio* band structure; (b) zero-temperature two-terminal conductance G_{21}; and (c)–(f) LDOS at $E - E_F = 0$ for an infinite graphene-on-hBN wire with zigzag edges. The wire is clean in (c); it includes bulk nanopore in (d); or edge vacancies in (e) and (f). The wire of width $W = 13$ nm is described by a DFT Hamiltonian in the basis of double-zeta polarized pseudoatomic orbitals on C, B, N and edge passivating H atoms, and local density approximation is used for the exchange-correlation functional.

whose two- or four-terminal resistance, nevertheless, remains $\lesssim h/2e^2$ in Figure 5.7(b) and Figure 5.3(a).

5.7 Chapter summary

By combining *ab initio* with quantum transport calculations, we demonstrate that graphene-on-hBN wires with zigzag edges host edge states near the DP. This was previously missed in theories based on too simplistic gapped Hamiltonians that predicted insulating states of graphene on hBN. Then, look for models that better describe the system and result in $R_{\rm NL} \neq 0$ near the DP, similar to experimental observations [1].

Since the usage of a DFT Hamiltonian is prohibitively expensive for the large number of atoms ($\sim 10^6$) in our LB or Kubo formula calculations, we construct simpler *ab initio* TBHs. A widely-used approach for this purpose is to transform the DFT

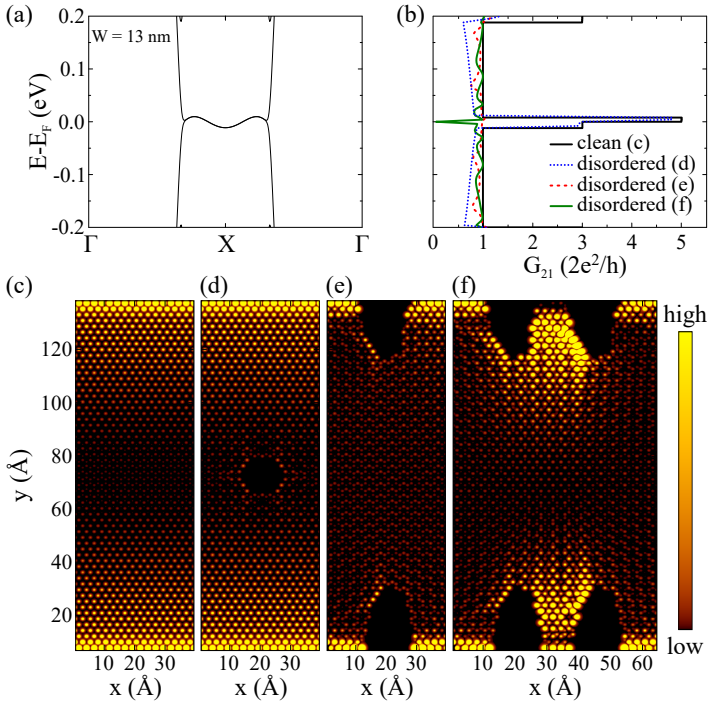

Figure 5.8: (a) *Ab initio* band structure; (b) zero-temperature two-terminal conductance G_{21}; and (c)–(f) LDOS at $E - E_F = 0$ for an infinite isolated graphene wire with zigzag edges. The wire is clean in (c), or it includes bulk nanopore in (d) or edge vacancies in (e) and (f). The wire of width $W = 13$ nm is described by a DFT Hamiltonian in the basis of DZP orbitals on C, B, N and edge passivating H atoms, and LDA is used for the XC functional. Each panel can be compared with the corresponding panels in Figure 5.7 for graphene-on-hBN wire with zigzag edges.

Hamiltonian to a basis of maximally localized Wannier functions [263, 266] in a selected energy window around E_F. We employ a Wannier TBH in the Kubo-Bastin formula calculations in Figure 5.3(b), finding also quantized σ^v_{xy} in the gap, as well as its surprising resilience to short-range disorder that was not exhibited in Figure 5.3(a) for the "standard model" TBH in Equation 5.1. However, the Wannier TBH applied to graphene-on-hBN wires generates a much higher group velocity $\partial\varepsilon(k_x)/\hbar\partial k_x$ of the edge state bands near $E - E_F = 0$ in Figure 5.5(d) than the DFT Hamiltonian in Figure 5.7(a) because the bulk DFT calculations performed to construct the Wannier TBH do not include information about atoms (like H) passivating bonds of edge carbon atoms which effectively changes the on-site energy in the TBH along the edge [272].

Therefore, we construct another *ab initio* TBH which fits the bands around $E - E_F = 0$ in Figure 5.5(c), whose up to fifth NN hoppings and on-site energies are given in Figure 5.6. The *ab initio* 5NN TBH combined with the multiterminal LB formula calculations yields $R_{\rm NL}$ in Figure 5.2(a) and ρ_{xx} in Figure 5.2(d) which are sharply

peaked near the DP in both clean and edge-disorder graphene-on-hBN channels. The edge disorder is introduced by removing the edge tight-binding sites along segments of random length, as well as by adding an on-site energy on the remaining edge sites which is distributed randomly in the range ± 1 eV chosen to model the binding of chemical species to the outermost carbon atoms [152]. The peak value of ρ_{xx} in Figure 5.2(d) is about an order of magnitude larger than the measured one in Ref. [1], which could be attributed to the choice of contacts like an abrupt interface between graphene-on-hBN central region and graphene leads in Figure 5.1. Although metallic-like ρ_{xx} could arise due to trivial reasons, such as charge inhomogeneity induced by chemical or electrostatic doping, the recent experimental imaging [238] of proximity-induced supercurrents flowing within narrow strips near the edges is in full agreement with the spatial profiles of edge currents computed in Figure 5.7(d)–(f).

6 Tunneling anisotropic magnetoresistance in TI/metal heterostructures

6.1 Introduction

The recent experiments on spin-orbit torque (SOT) [2, 3, 4, 5] and spin-to-charge conversion [6, 7, 8, 9, 10, 11] in topological-insulator/ferromagnetic-metal (TI/FM) heterostructures have ignited the field of *topological spintronics*. In these devices, giant non-equilibrium spin densities [273, 99, 274, 275] are expected to be generated due to strong spin-orbit coupling (SOC) on metallic surfaces of three-dimensional (3D) TIs and the corresponding (nearly [276]) helical spin-momentum locking along a single Fermi circle for Dirac electrons hosted by those surfaces [12, 13]. Such strong interfacial SOC-driven phenomena are also envisaged to underlie a plethora of novel spintronic technologies [92].

These effects have been interpreted almost exclusively using simplistic models, such as the Dirac Hamiltonian for the TI surface with an additional Zeeman term describing the coupling of magnetization of the FM layer to the surface state spins [12, 13], $\hat{H}^{\mathrm{Dirac}} = v_F(\hat{\boldsymbol{\sigma}} \times \hat{\mathbf{p}})_z - \Delta \mathbf{m} \cdot \hat{\boldsymbol{\sigma}}$, where $\hat{\mathbf{p}}$ is the momentum operator, $\hat{\boldsymbol{\sigma}}$ is the vector of the Pauli matrices, $\mathbf{m}$ is the magnetization unit vector and v_F is the Fermi velocity. Thus, the only effect of the FM layer captured by $\hat{H}^{\mathrm{Dirac}}$ is the proximity effect-induced exchange coupling Δ which opens a gap in the Dirac cone energy-momentum dispersion [12, 13], thereby making Dirac electrons massive. On the other hand, recent first-principles calculations [277, 278] demonstrate that the band structure of even TI/ferromagnetic-insulator (TI/FI) bilayers, where hybridization between TI and FI states is largely absent, cannot be captured by simplistic models like $\hat{H}^{\mathrm{Dirac}}$. The properties of TI/FM interfaces are far more complex due to injection of evanescent wave functions from the FM layer into the bulk gap of the TI layer, which can hybridize with the surface state of the TI and blur its Dirac cone (as already observed in tight-binding models of TI/metal interfaces [274, 279, 280]), as well as related charge transfer. Thus, the *key issue* for topological spintronics [2, 3, 4, 5, 6, 7, 8, 9, 10, 11, 92] is to understand the band structure and spin textures (including the fate of the Dirac cone and its spin-momentum locking) in hybridized TI with FM or normal metal (NM) [11] layers at

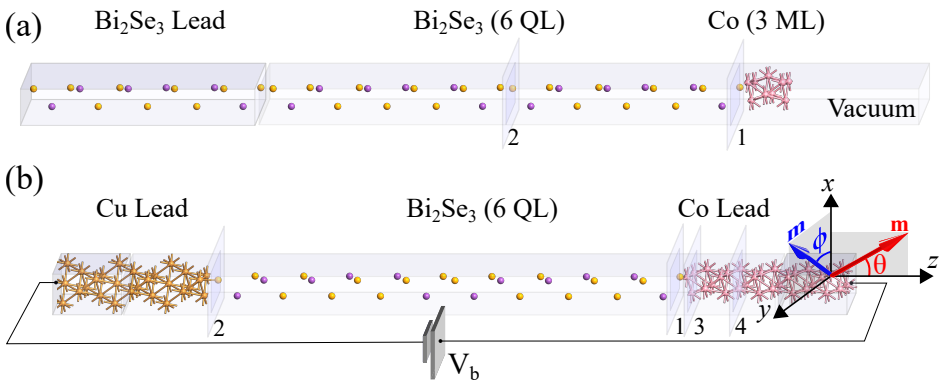

Figure 6.1: Schematic view of a TI-based heterostructures where: (a) semi-infinite Bi_2Se_3 layer is attached to n monolayers of Co(0001); (b) 6 QLs of Bi_2Se_3 are sandwiched between a semi-infinite Cu(111) layer and semi-infinite Co(0001) layer. Both heterostructures are infinite in the transverse direction, so that the depicted supercells are periodically repeated within the xy-plane. The magnetization $\mathbf{m}$ of the Co layer is fixed along the z-axis in (a), or rotated within the xy-plane or the xz-plane in (b). Applying the bias voltage V_b to the *vertical* heterostructure in panel (b) leads to a charge current flowing *perpendicularly* to both Bi_2Se_3/Cu and Bi_2Se_3/Co interfaces.

the nanometer scale around the interface where they are brought into contact, where properties of both the TI side and FM or NM side of the interface can be quite different from the properties of the corresponding bulk materials.

For example, computational searches [70] for new materials realizing 3D TIs (or other topologically nontrivial electronic phases of matter like Weyl semi-metals [281] and Chern insulators [271]) have crucially relied on first-principles calculations of spectral function on their boundaries and its confirmation by spin- and angle-resolved photoemission spectroscopy (spin-ARPES) [282]. A standard density functional theory (DFT)-based framework developed for this purpose—where the DFT band structure around the Fermi level E_F^0 is reconstructed using the Wannier tight-binding Hamiltonian [263] used to obtain the retarded Green's function (GF) of a semi-infinite homogeneous crystal and the spectral function on its surface in contact with vacuum [70, 281, 271]—is difficult to apply to complicated inhomogeneous systems like TI/FM bilayers due to strongly entangled bands in the region of interest around E_F^0. Also, spin-ARPES experiments cannot probe buried interfaces below too many monolayers (e.g., penetration depth of low-energy photons is 2–4 nm) of FM or NM deposited onto the TI surface [282].

An attempt [283] to obtain the spectral function, $A_j(E;\mathbf{k}) = \sum_{n,i}^{i\in \mathrm{QL}_j} w_{n\mathbf{k}}^i \delta(E-\varepsilon_{n\mathbf{k}})$, directly from DFT computed energy-momentum dispersion $\varepsilon_{n\mathbf{k}}$ (n is the band index and $\mathbf{k}$ is the crystal momentum) and site-projected character $w_{n\mathbf{k}}^i$ of the corresponding

eigenfunctions for TI/FM supercells has produced ambiguous results. This is due to arbitrariness in broadening the delta function $\delta(E - \varepsilon_{n\mathbf{k}})$, as well as due to usage of atomic sites i within the whole j quintuple layer (QL_j) of Bi_2Se_3 (one QL consists of three Se layers strongly bonded to two Bi layers in between) which effectively averages the spectral function over all geometric planes within QL_j. Similar ambiguities (such as setting the amount of electron density which is localized on the surface or within the whole interfacial QL) plague the interpretation of the projected DFT band structure of TI/FI [278] and TI/FM bilayers [284].

Here we develop a framework which combines the noncollinear DFT Hamiltonian $\mathbf{H}^{\mathrm{DFT}}$, represented in a basis of variationally optimized localized atomic orbitals [254], with retarded GF calculations from which one can extract the spectral function and spin textures at an arbitrary geometric plane of interest within a junction combining TI, FM and NM layers. It also makes it possible to compute their spin and charge transport properties in the linear-response regime or at finite bias voltage. We apply this framework to two Bi_2Se_3-based heterostructures whose supercells are depicted in Figure 6.1, where we assume that those supercells are periodically repeated in the transverse xy-direction.

6.2 Proximity band structure and spin textures on Bi_2Se_3/ferromagnetic-metal interfaces

The heterostructure in Figure 6.1(a) consists of Bi_2Se_3, chosen as the prototypical 3D TI [276, 12, 13, 70], whose surface is covered by n monolayers (MLs) of Co. The retarded GF of this heterostructure is computed as

$$\mathbf{G}_{\mathbf{k}_\parallel}(E) = [E - \mathbf{H}^{\mathrm{DFT}}_{\mathbf{k}_\parallel} - \mathbf{\Sigma}^{\mathrm{Bi_2Se_3}}_{\mathbf{k}_\parallel}(E)]^{-1}, \tag{6.1}$$

where $\mathbf{k}_\parallel = (k_x, k_y)$ is the transverse k-vector, $\mathbf{\Sigma}^{\mathrm{Bi_2Se_3}}_{\mathbf{k}_\parallel}(E)$ is the self-energy [285, 286, 287] describing the semi-infinite Bi_2Se_3 lead and $\mathbf{H}^{\mathrm{DFT}}_{\mathbf{k}_\parallel}$ is the Hamiltonian of the *active region* consisting of n MLs of cobalt plus 6 QLs of Bi_2Se_3 to which the lead is attached. We choose n =1–3 since ultrathin FM layers of thickness $\simeq 1$ nm are typically employed in SOT experiments [288] in order to preserve perpendicular magnetic anisotropy (note that magnetocrystalline anisotropy does favor the out-of-plane $\mathbf{m}$ in Bi_2Se_3/Co bilayers [284]). The spectral function (or local density of states) at an arbitrary plane at position z within the active region is computed from

$$A(E; k_x, k_y, z) = -\mathrm{Im}\,[G_{\mathbf{k}_\parallel}(E; z, z)]/\pi, \tag{6.2}$$

where the diagonal matrix elements $G_{\mathbf{k}_\parallel}(E; z, z)$ are obtained by transforming Equation 6.1 from orbital to a real-space representation.

The heterostructure in Figure 6.1(b) consists of semi-infinite Cu and Co leads sandwiching a Bi_2Se_3 layer of finite thickness, where we choose Cu as the NM layer similar to the very recent spin-to-charge conversion experiment of Ref. [11]. Such a heterostructure is termed *vertical* or *current-perpendicular-to-plane* in spintronics terminology since applying bias voltage V_b drives a current perpendicularly to the TI/FM interface. Its retarded GF is computed as

$$\mathbf{G}_{\mathbf{k}_\parallel}(E) = [E - \mathbf{H}^{\mathrm{DFT}}_{\mathbf{k}_\parallel} - \mathbf{\Sigma}^{\mathrm{Cu}}_{\mathbf{k}_\parallel}(E) - \mathbf{\Sigma}^{\mathrm{Co}}_{\mathbf{k}_\parallel}(E)]^{-1}, \tag{6.3}$$

where $\mathbf{H}^{\mathrm{DFT}}_{\mathbf{k}_\parallel}$ describes the active region consisting of 6 QLs of Bi_2Se_3 plus 4 MLs of Cu and 4 MLs of Cu. Its linear-response resistance R is given by the Landauer formula

$$\frac{1}{R} = \frac{e^2}{h\Omega_{\mathrm{BZ}}} \int_{\mathrm{BZ}} d\mathbf{k}_\parallel \int dE \left(-\frac{\partial f}{\partial E}\right) \mathrm{Tr}[\mathbf{\Gamma}^{\mathrm{Co}}_{\mathbf{k}_\parallel} \mathbf{G}_{\mathbf{k}_\parallel} \mathbf{\Gamma}^{\mathrm{Cu}}_{\mathbf{k}_\parallel} \mathbf{G}^{\dagger}_{\mathbf{k}_\parallel}], \tag{6.4}$$

where we assume temperature $T = 300$ K in the Fermi-Dirac distribution function $f(E)$, $\mathbf{\Gamma}^{\alpha}_{\mathbf{k}_\parallel} = i(\mathbf{\Sigma}^{\alpha}_{\mathbf{k}_\parallel} - [\mathbf{\Sigma}^{\alpha}_{\mathbf{k}_\parallel}]^{\dagger})$ and Ω_{BZ} is the area of the two-dimensional (2D) Brillouin zone (BZ) within which $\mathbf{k}_\parallel$ vectors are sampled.

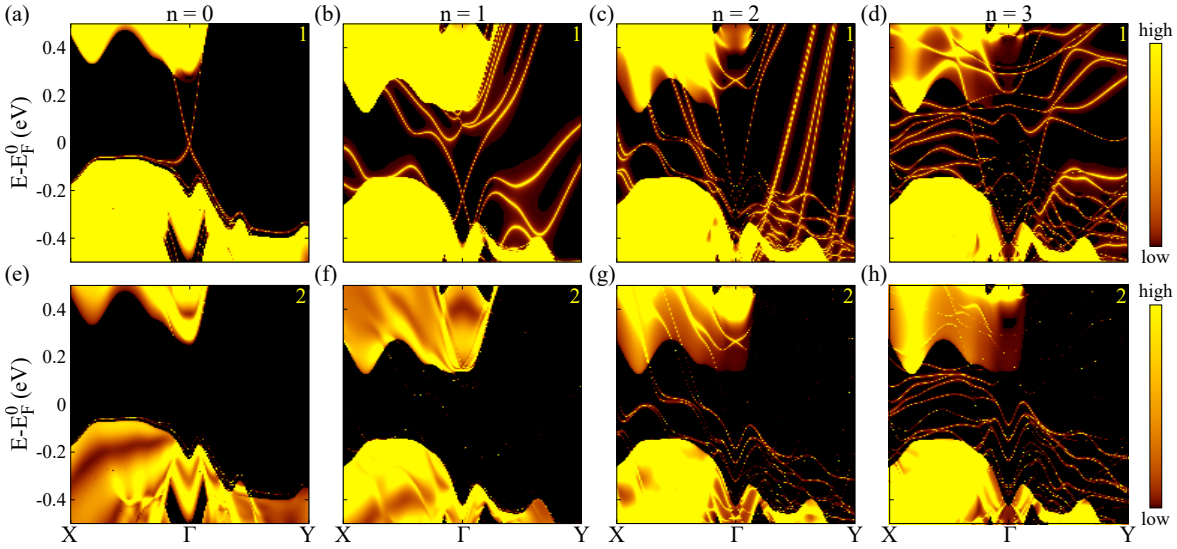

Figure 6.2: Spectral function, defined in Equation 6.2, at plane 1 for panels (b)–(d) or plane 2 for panels (f)–(h) within Bi_2Se_3/Co(n ML) heterostructure in Figure 6.1(a) with $\mathbf{m} \parallel \hat{z}$. For comparison, panels (a) and (e) plot the spectral function at planes 1 (akin to Ref. [70]) and 2, respectively, within the semi-infinite Bi_2Se_3 crystal in contact with vacuum (i.e., $n = 0$). From Γ to Y we plot $A(E; k_x = 0, k_y; z \in \{1, 2\})$, while from Γ to X we plot $A(E; k_x, k_y = 0; z \in \{1, 2\})$.

The spectral function of the heterostructure in Figure 6.1(a) computed at planes 1 and 2 within the Bi_2Se_3 layer is shown in Figure 6.2(b)–(d) and Figure 6.2(f)–(h),

respectively, where plane 1 is passing through Se atoms on the Bi_2Se_3 surface in contact with the Co layer and plane 2 is three QLs (or $\simeq 2.85$ nm) away from plane 1. For comparison, we also show in Figure 6.2(a) and Figure 6.2(b) the spectral function at the same two planes within the semi-infinite Bi_2Se_3 layer in contact with vacuum, thereby reproducing the results from Ref. [70] by our formalism. While the Dirac cone at the Γ-point is still intact in Figure 6.2(b) for $n = 1$ ML of Co, its Dirac point (DP) is gradually pushed into the valence band of Bi_2Se_3 with increasing n because of charge transfer from metal to TI. The charge transfer visualized in Figure 6.6(c) and Figure 6.6(d) is relatively small, but due to small density of states (DOS) at the DP it is easy to push it down until it merges with the larger DOS in the valence band of the TI. Adding more MLs of Co in Figure 6.2(c) and Figure 6.2(d) also introduces additional bands within the bulk gap of Bi_2Se_3 due to injection of evanescent wave functions which hybridize with the Dirac cone. The metallic surface states of Bi_2Se_3 itself penetrate into its bulk over a distance of 2 QLs [99], so that in Figure 6.2(e) the spectral function on plane 2 vanishes inside the gap of the semi-infinite Bi_2Se_3 layer in contact with vacuum, while the remaining states inside the gap in Figure 6.2(f)–(h) can be attributed to the Co layer.

For infinitely many MLs of Co attached to 6 QLs of Bi_2Se_3 within the Cu/Bi_2Se_3/Co heterostructure in Figure 6.1(b), the remnant of the Dirac cone from the TI surface can be identified in Figure 6.3(a) at around 0.5 eV below E_F^0 while it is pushed even further below in the case of the Cu/Bi_2Se_3 interface in Figure 6.3(e). The difference in work functions $\Phi_{\mathrm{Co}} = 5.0$ eV or $\Phi_{\mathrm{Cu}} = 4.7$ eV and electron affinity $\chi_{\mathrm{Bi_2Se_3}} = 5.3$ eV determines [283] the band alignment and the strength of hybridization, where n-type doping [see also Figure 6.6(c) and Figure 6.6(d)] of the Bi_2Se_3 layer pins E_F^0 of the whole Cu/Bi_2Se_3/Co heterostructure in the conduction band of the bulk Bi_2Se_3. The remnant of the Dirac cone is quite different from the often assumed [12, 13] eigenspectrum of $\hat{H}^{\mathrm{Dirac}}$ because of hybridization with the valence band of Bi_2Se_3, as well as with states injected by the Co or Cu layers whose penetration into TI is visualized by plotting the position- and energy-dependent spectral function $A(E;z) = \frac{1}{\Omega_{\mathrm{BZ}}} \int dk_x dk_y \, A(E;k_x,k_y;z)$ in Figure 6.5(a). On the other hand, the energy-momentum dispersion in the vicinity of E_F^0 and for an interval of $\mathbf{k}_\parallel$ vectors around the Γ-point is surprisingly well-described by another simplistic model—ferromagnetic Rashba Hamiltonian [289].

In Figure 6.3(b)—(d) and Figure 6.3(f)—(h) we show constant energy contours of the spectral function at three selected energies E denoted in Figure 6.3(a) and Figure 6.3(e) by dashed horizontal lines. Instead of a single circle as the constant energy contour for the eigenspectrum of $\hat{H}^{\mathrm{Dirac}}$, or single hexagon or snowflake-like contours (due to hexagonal warping [276]) sufficiently away from the DP for the eigenspectrum of $\mathbf{H}^{\mathrm{DFT}}$ of the isolated Bi_2Se_3 layer, here we find multiple circular and snowflake-like contours close to the Γ-point. The spin textures within the constant energy contours are computed from the spin-resolved spectral function. For energies near $E = E_F^0$, the spin textures shown in Figure 6.3(b) and Figure 6.3c) are quite different from the helical

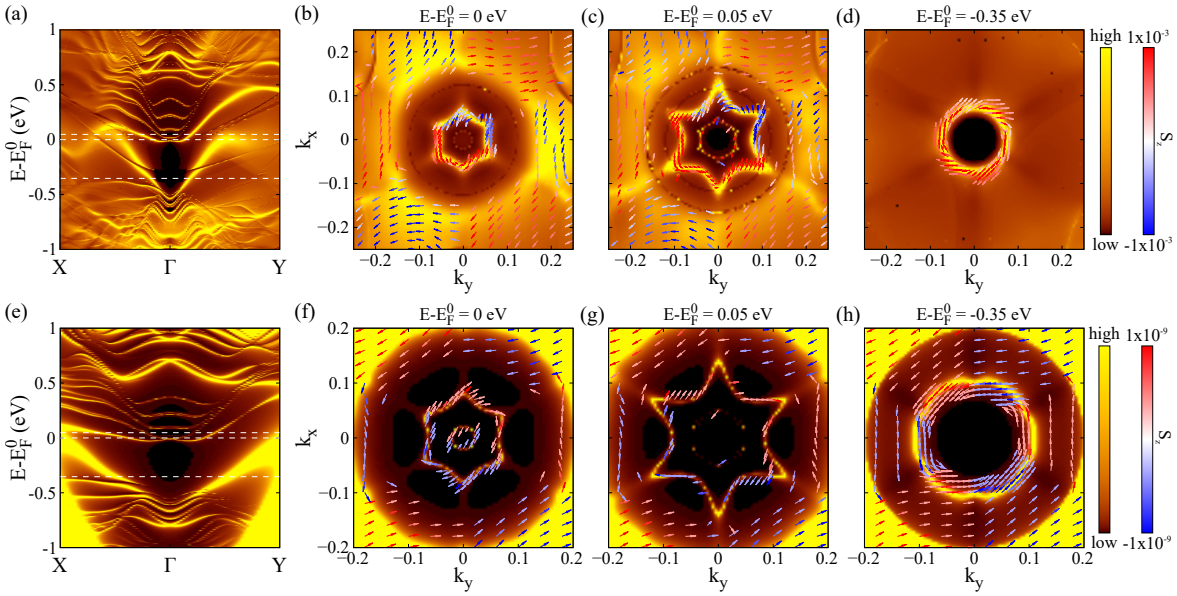

Figure 6.3: Spectral function at: (a)–(d) plane 1 in Figure 6.1(b) which is passing through Se atoms at the Bi_2Se_3/Co interface with $\mathbf{m} \parallel \hat{z}$; and (e)–(h) plane 2 in Figure 6.1(b) which is passing through Se atoms at the Bi_2Se_3/Cu interface, where we remove the Co layer to make Bi_2Se_3 semi-infinite along the z-axis. In panels (a) and (e), we plot $A(E; k_x = 0, k_y; z \in \{1, 2\})$ from Γ to Y and $A(E; k_x, k_y = 0; z \in \{1, 2\})$ from Γ to X. Panels (b)–(d) and (f)–(h) plot constant energy contours of $A(E - E_F^0 \in \{0.0 \text{ eV}, 0.05 \text{ eV}, -0.35 \text{ eV}\}; k_x, k_y; z \in \{1, 2\})$ at three energies marked by horizontal dashed lines in panels (a) or (e), respectively, as well as the corresponding spin textures where the out-of-plane S_z component is indicted in color (red for positive and blue for negative). The units for k_x and k_y are $2\pi/a$ where a is the lattice constant of a common supercell combining two unit cells of the two layers around the corresponding interface.

ones in isolated Bi_2Se_3 layer [70]. Nevertheless, Figure 6.3(d) shows that the remnant Dirac cone still generates distorted helical spin texture wounding along a single circle but with out-of-plane S_z component due to the presence of the Co layer.

The envisaged applications of TIs in spintronics are based [2, 3, 4, 5, 6, 7, 8, 9, 10, 11, 273, 274, 275] on spin textures like the one in Figure 6.3(d) since it maximizes [273, 99] the generation of nonequilibrium spin density when current is passed parallel to the TI surface. However, utilizing spin texture in Figure 6.3(d) in lateral TI/FM heterostructures would require to shift E_F (by changing the composition of TI [11] or by applying a gate voltage [5]) by few tenths of eV below E_F^0 of the undoped heterostructures in Figure 6.3(a). For example, extreme sensitivity of spin-to-charge conversion was recently observed [11] on the surface of $(Bi_{1-x}Sb_x)_2Te_3$ TI covered by a 8 nm thick Cu layer as E_F of the TI layer was tuned, which is difficult to explain by

assuming that the Dirac cone on the TI surface remains intact after the deposition of the Cu layer (e.g., Ref. [11] had to invoke "instability of the helical spin structure"). On the other hand, it is easy to understand from Figure 6.3(f)–(h) how spin textures at the Bi_2Se_3/Cu interface change dramatically as one moves E_F (even slightly) below or above E_F^0. Comparing Figure 6.3(a)–(d) with Figure 6.3(e)–(h) makes it possible to understand the effect of the magnetization of the Co layer, which modifies [289] Rashba dispersion around E_F^0 and the corresponding spin textures (particularly the out-of-plane S_z component).

The theoretical modeling of SOT in TI/FM [2, 275] or heavy-metal/FM [290] bilayers is usually conducted by starting from strictly 2D Hamiltonians, such as $\hat{H}^{\text{Dirac}}$ or the Rashba ferromagnetic model [289], respectively, so that the FM layer is not considered explicitly. Figure 6.4(f)–(h) show that this is not warranted since the Bi_2Se_3 layer induces proximity SOC and the corresponding *proximity in-plane spin textures* over the few MLs of Co, which decay to a negligible value in Figure 6.4(j)–(l) only after reaching plane 4 in Figure 6.1(b). The fact that conventional room temperature metallic ferromagnet can acquire properties of topological insulators, as demonstrated convincingly by Figure 6.4(e)–(l) solves the problem of very small critical temperature $\lesssim 10$ K in recent attempts [3, 291] to create ferromagnetic topological matter by doping 3D TIs with magnetic impurities. The existence of proximity in-plane spin textures in Co due to a TI layer shown in Figure 6.4(f)–(h) is crucial for topological spintronics where it has been considered [2] that an applied current will be shunted through the metallic magnet and, therefore, not contribute to nonequilibrium spin density generation within the topological insulator. On the contrary, Figure 6.4(f)–(h) and Figure 6.4(j)–(l) suggest that the efficiency of the SOT in TI/FM bilayers will be mainly determined by the ability of the TI to inject sizable in-plane spin texture over the *whole ultrathin FM layer* which generates a nonequilibrium spin density [99] $\mathbf{S}_{\text{neq}}$ and SOT $\propto \mathbf{S}_{\text{neq}} \times \mathbf{m}$ [275, 290] when current is passed parallel to the MLs of Co hosting those textures. We note that few previous experimental [282] and theoretical studies [282, 280] have suggested the possibility of proximity-induced spin textures only into one monolayer nonmagnetic metal or semiconductor in contact with a TI layer and for special bonding requirements at the contact [282].

We also find non-trivial in-plane spin texture even on the surface of Co in contact with vacuum, as shown in Figure 6.4(b)–(d), which is nevertheless quite different from those in Figure 6.4(f)–(h). The spin texture in Figure 6.4(b)–(d) is a consequence of the Rashba SOC enabled by inversion asymmetry due to the Co surface [292] where an electrostatic potential gradient can be created by the charge distribution at the metal/vacuum interface and thereby confine wave functions into a Rashba spin-split quasi-2D electron gas [293]. The spin textures in Figure 6.4(a)–(d) explain the origin of recently observed [294] SOT in the absence of any adjacent heavy metal or TI layer.

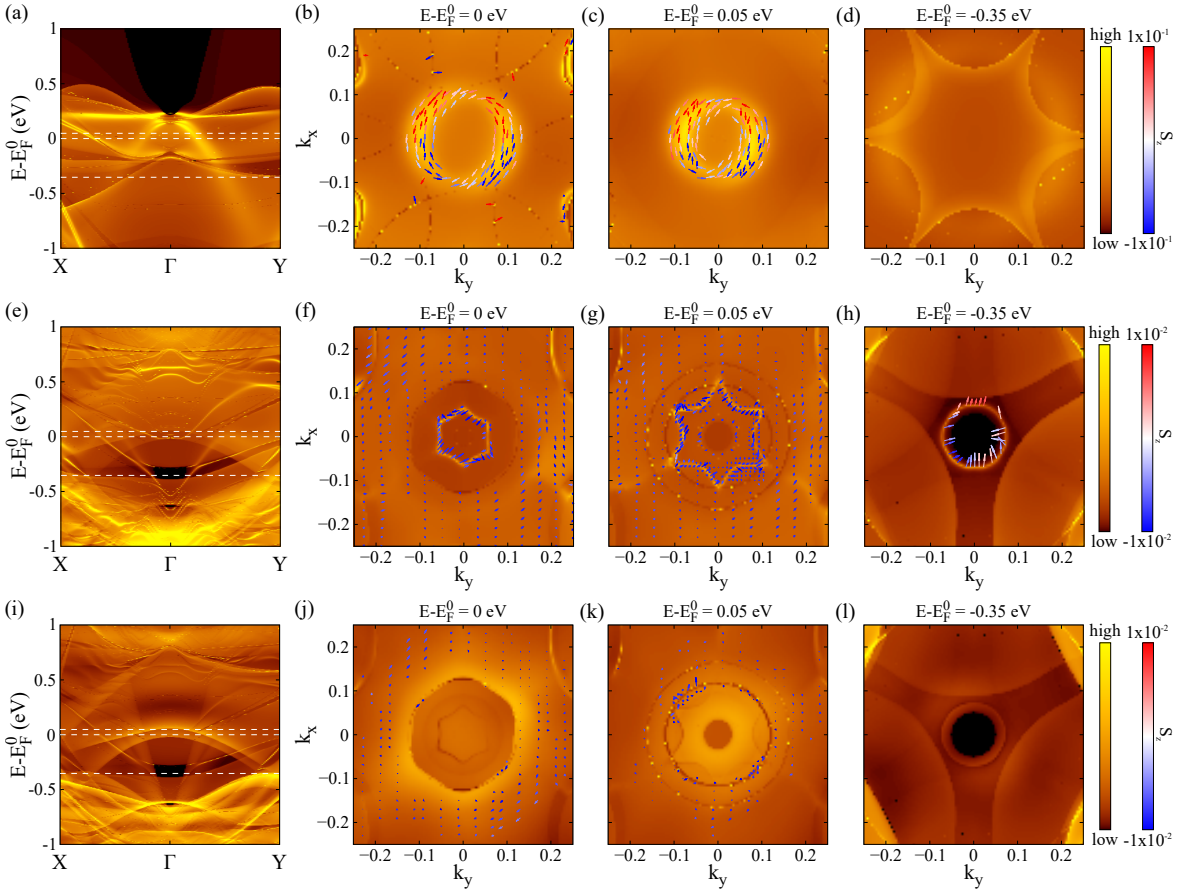

Figure 6.4: Spectral function at: (a)–(d) the surface of a semi-infinite Co layer in contact with vacuum; (e)–(h) plane 3 in Figure 6.1(b) passing through Co atoms at the Bi_2Se_3/Co interface; and (i)–(l) plane 4 in Figure 6.1(b) passing through Co atoms away from the interface. Magnetization $\mathbf{m}$ of the Co layer is perpendicular to the interface, $\mathbf{m} \parallel \hat{z}$, in all panels (a)–(l). In panels (e) and (i), we plot $A(E; k_x = 0, k_y; z \in 3)$ from Γ to Y and $A(E; k_x, k_y = 0; z \in 3)$ from Γ to X. Panels (b)–(d), (f)–(h) and (j)–(l) plot constant energy contours of the spectral function at three energies marked by horizontal dashed lines in panels (a), (e), and (i), respectively, as well as the corresponding spin textures where the magnitude of the out-of-plane S_z component is indicted in color (red for positive and blue for negative). The units for k_x and k_y are $2\pi/a$ where a is the lattice constant of a common supercell combining two unit cells of the two layers around the corresponding interface.

6.3 Tunneling anisotropic magnetoresistance in a Cu/Bi_2Se_3/Co heterostructure

Finally, we propose a purely charge transport measurement that could detect which among the spin-textures shown in Figure 6.3(b)–(d) resides at the Fermi level of the TI/FM interface. Our scheme requires to fabricate the vertical heterostructure in Figure 6.1(b) and measure its tunneling anisotropic magnetoresistance (TAMR). The TAMR is a phenomenon observed in magnetic tunnel junctions with a *single* FM layer [274, 295, 292, 296], where SOC makes the band structure anisotropic so that the resistance of such junctions changes as the magnetization $\mathbf{m}$ is rotated by an angle θ or ϕ in Figure 6.1(b). The resistance change is quantified by the TAMR ratio defined as [292, 296]

$$\mathrm{TAMR}_{\mathrm{out(in)}}(\alpha) = \frac{R(\alpha) - R(0)}{R(0)}. \tag{6.5}$$

Here $\alpha \equiv \theta$ for $\mathrm{TAMR}_{\mathrm{out}}$ where magnetization in Figure 6.1(b) rotates in the plane perpendicular to the TI/FM interface, and $\alpha \equiv \phi$ for $\mathrm{TAMR}_{\mathrm{in}}$ where magnetization in Figure 6.1(b) rotates within the plane of the TI/FM interface. In the case of $\mathrm{TAMR}_{\mathrm{out}}(\theta)$, $R(0)$ is the resistance when $\mathbf{m} \parallel \hat{z}$ in Figure 6.1; and in the case of $\mathrm{TAMR}_{\mathrm{in}}(\phi)$, $R(0)$ is the resistance when $\mathbf{m} \parallel \hat{x}$ in Figure 6.1. Thus, $\mathrm{TAMR}_{\mathrm{out}}(\theta)$ changes due to the different orientations of the magnetization with respect to the direction of the current flow, while the situation becomes more subtle for $\mathrm{TAMR}_{\mathrm{in}}(\phi)$ where the magnetization remains always perpendicular to the current flow. Figure 6.5(b) demonstrates that the largest $\mathrm{TAMR}_{\mathrm{out}}(\theta = \pm 90^\circ)$ is obtained by tuning the Fermi level to $E_F - E_F^0 = -0.35$ eV so that nearly helical spin texture in Figure 6.3(d) resides at the Fermi level. Another signature of its presence is the rapid increase of $\mathrm{TAMR}_{\mathrm{out}}(\theta)$ when tilting $\mathbf{m}$ by small angles θ away from the current direction. The in-plane $\mathrm{TAMR}_{\mathrm{in}}(\phi)$ shown in the inset of Figure 6.5(b) is a much smaller (and difficult to converge in the number of transverse k-points) quantity which does not differentiate between spin textures shown in Figure 6.3(b)–(d).

6.4 Methods

We employed the interface builder in the `VNL` [297] and `CellMatch` [298] packages to construct a common unit cell for: (a) Bi_2Se_3/Cu(111) bilayer, where the common unit cell is 5×5 in size compared to the smallest possible Cu(111) slab cell and copper is under compressive strain of 0.9 % while the Bi_2Se_3 lattice constant is unchanged; (b) Bi_2Se_3/Co(0001) bilayer where Co(0001) has the same lattice constant as Bi_2Se_3, so the same unit cell as for Cu(111) is used without any strain on Co(0001). These two

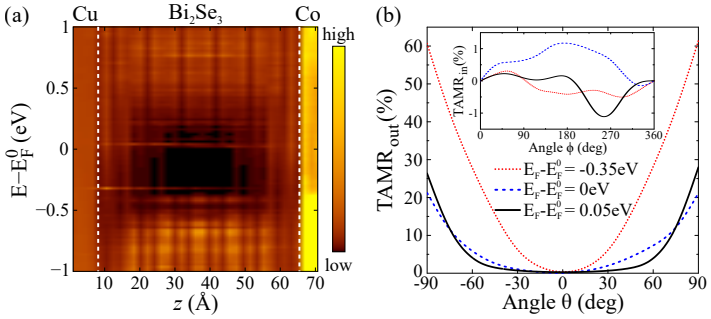

Figure 6.5: (a) The position- and energy-dependent spectral function $A(E;z) = \frac{1}{\Omega_{\mathrm{BZ}}} \int dk_x dk_y \, A(E;k_x,k_y;z)$ from the left Cu lead, across Bi_2Se_3 tunnel barrier, toward the right Co lead for the heterostructure in Fig. Figure 6.1(b). (b) The out-of-plane $\mathrm{TAMR}_{\mathrm{out}}(\theta)$ ratio defined in (Equation 6.5) as a function of the angle θ between the magnetization $\mathbf{m}$ and the direction of current injected along the z-axis in Figure 6.1(b). Inset in panel (b) shows angular dependence of the in-plane $\mathrm{TAMR}_{\mathrm{in}}(\phi)$ ratio. In order to converge the integration over the transverse wave vector $\mathbf{k}_{\parallel}$ in (Equation 6.4), we employ a uniform grid of 101×101 k-points for $\mathrm{TAMR}_{\mathrm{out}}(\theta)$ and 251×251 k-points for $\mathrm{TAMR}_{\mathrm{in}}(\phi)$.

unit cells are illustrated in Figure 6.6(a) and Figure 6.6(b), respectively. In order to determine the best stacking of atomic layers and the distance of the Bi_2Se_3 atoms with respect to the surfaces of Cu(111) and Co(0001), we use DFT calculations as implemented in the `VASP` package [264, 265]. The electron core interactions are described by the projector augmented wave (PAW) method [267, 268], and vdW-DF [299] with optB88 is used as density functional [300] in order to describe van der Waals (vdW) forces between QLs of Bi_2Se_3 or between Bi_2Se_3 and the metallic layers. The cutoff energy for the plane wave basis set is 520 eV for all calculations, while k-points were sampled at 3×3 surface mesh. We use Cu and Co layers consisting of 5 MLs, where 3 bottom MLs are fixed at bulk positions while the top two metallic MLs closest to Bi_2Se_3 are allowed to fully relax until forces on atoms drop below 1 meV/Å. In order to avoid interaction with periodic images of the bilayer, 18 Å of vacuum was added in the z–direction.

For the case of Bi_2Se_3 on Co(0001), the most favorable position yields a binding energy of 460 meV per Co atom. Both ML of Co and QL of Bi_2Se_3 in direct contact gain some corrugation, roughly around $\simeq 0.1$ Å, while the average z–distance between them is 2.15 Å. The average distance between the ML of Cu and QL of Bi_2Se_3 in direct contact is around 2.26 Å with smaller corrugation than in the case of Co(0001), while the binding energy is 294 meV per Cu atom. For other relative positions of the Bi_2Se_3 layer with respect to the Cu(111) and Co(0001) layers the difference in binding energy is very small. Binding energies in both cases are rather small, thereby signaling the dominant vdW forces. Nevertheless, some charge rearrangement does occur at the interface

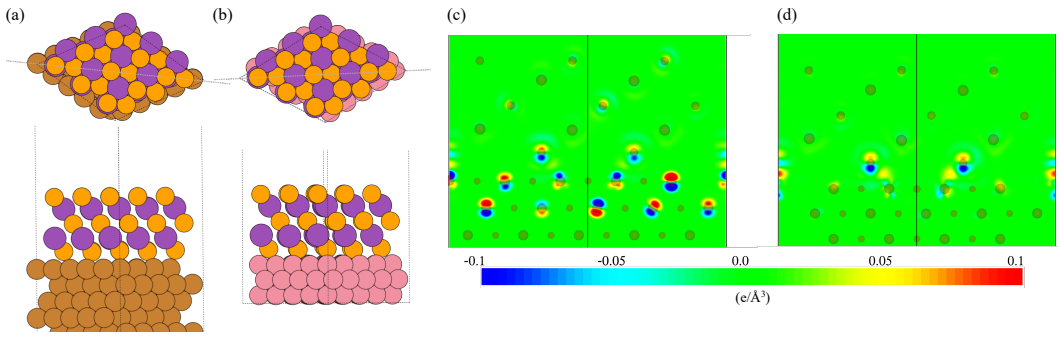

Figure 6.6: Top and side view of common unit cells for (a) Bi_2Se_3/Cu(111) and (b) Bi_2Se_3/Co(0001) bilayers. Panels (c) and (d) show charge rearrangement around the interface of bilayers in panels (a) and (b), respectively.

due to the push back/pillow effect [301], as shown in Figure 6.6(c) and Figure 6.6(d) where the charge rearrangement is more pronounced for the case of the Bi_2Se_3/Cu(111) interface.

The calculation of the retarded GF in Equation 6.1 and Equation 6.3 requires $\mathbf{H}^{\mathrm{DFT}}_{\mathbf{k}_\parallel}$ represented in the linear combination of atomic orbitals (LCAO) basis set which makes it possible to spatially separate the system into an active region attached to one or two semi-infinite leads, as illustrated in Figure 6.1(a) and Figure 6.1(b), respectively. We employ the `ATK` package [252] for pseudopotential-based LCAO noncollinear DFT calculations yielding $\mathbf{H}^{\mathrm{DFT}}_{\mathbf{k}_\parallel}$, from which we obtain the retarded GFs and the corresponding spectral functions, as well as the resistance in Equation 6.4. In `ATK` calculations, we use the Perdew-Burke-Ernzerhof (PBE) parametrization of generalized gradient approximation for the exchange-correlation functional; norm-conserving pseudopotentials for describing the electron-core interactions; and the LCAO basis set generated by the `OpenMX` package [254, 253] which consists of `s2p2d1` orbitals on Co, Cu and Se atoms, and `s2p2d2` on Bi atoms. These pseudoatomic orbitals were generated by a confinement scheme [254] with the cutoff radius 7.0 and 8.0 a.u. for Se and Bi atoms, respectively, and 6.0 a.u. for Co and Cu atoms. The energy mesh cutoff for the real-space grid is chosen as 75.0 Hartree.

6.5 Chapter summary

The control of recent experimentally observed effects in topological spintronics, based on heterostructures combining 3D TIs with conventional room temperature metallic ferromagnets, is thwarted by the lack of understanding of energy as a function of momentum and spin properties of electrons around their interfaces. For example, interpretation of these experiments has relied on the naive picture offered by simplistic

models where a ferromagnetic layer simply opens an energy gap in the Dirac cone energy-momentum dispersion on electrons hosted by metallic surfaces of TIs while leaving the locking of electron spin and momentum intact.

Here we introduce a novel first-principles technique which allows us to obtain energy-momentum dispersion and spin properties of electrons at an arbitrary geometric plane within TI/FM heterostructures. This reveals that the FM distorts the Dirac cone on the TI side and pushes it deep below the Fermi energy, while few monolayers of the FM acquire spin textures injected by the TI. Passing charge current parallel to these monolayers will induce nonequilibrium spin density which plays a key role for understanding recent and future experiments in topological spintronics.

We also propose a charge transport measurement, where current flows perpendicular to the TI/FM interfaces while being modulated by rotating the magnetization of the ferromagnetic layer, which offers a sensitive probe of the type of spin texture residing at the Fermi energy. Finally, we calculate a maximum TAMR of 60% for the $Cu/Bi_2Se_3/Co$ heterostructure in Figure 6.1(b) , showing that the studied TI/FM heterostructures could be useful for memory applications as in magnetoresistive random-access memory (MRAM) devices.

7 Conclusions and future work

New paradigms in design for logic and memory devices are required for the next-generation integrated circuits. This includes different approaches in devices, data representation, materials and state variables, where the aim of research is to: i) extend the capabilities of existing CMOS technologies or ii) explore new technologies beyond CMOS elements [14, 144].

In this sense, the initial approach is to replace silicon channels in typical FET structures by other semiconductors that may overcome the technical difficulties of very small silicon-based devices where the length of their channels is only a few nanometers. Since the discovery of graphene, researchers have tried to incorporate this material to traditional semiconductor processes in order to have a more convenient transition to large-scale production of devices, but finding limitations in controllably obtaining defect-free semiconducting structures with highly reproducible bandgaps that could be integrated into existing manufacturing processes, since large-area graphene is a semi-metal that is not suitable for commercial digital devices with very low leakage currents. Then, for achieving successful graphene-based nanoelectronics, it is required to develop scalable, reliable and cost-effective manufacturing process and explore novel device architectures that could outperform state-of-the-art silicon devices.

For such approach, we have explored multiterminal graphene-based structures i) decorated with gold adatoms and ii) deposited on a hBN substrate, where the injection of an unpolarized charge current generates a non-local voltage, whose relation (R_{NL}) is used to characterize the system. We observed non-zero RNL near the CNP in both setups, even in sufficiently long devices for which we calculated $R_{\mathrm{NL}} = 0$ in typical NN-TB models of pristine graphene. Such signal may be useful for implementing novel switching devices for low-power logic applications, if a very sharp signal can be obtained for large I_{on}/I_{off}, as seen in recent experiments [1]. Then, our next step would be to use these non-local signals for designing transistors and calculating their performance metrics, for which it would be required to use simulation techniques beyond TB approximations. One option would be the usage of DFT Hamiltonians for characterizing the system, however, the size of such matrices is very large for the number of atoms in our multiterminal systems ($\sim 10^6$) and computations become prohibitively expensive.

Finally, we have also studied TI/FM heterostructures by means of first-principles calculations that helped us understand the effects of TI/FM interfaces on electrons and their

spin properties near the interface, where we found: i) a distortion of the Dirac cone on the TI side due to the FM and ii) an injection of spin textures on the FM side by the TI. The aim of these heterostructures is to obtain devices whose resistance is strongly dependent on the angle of magnetization, characterized by the TAMR ratio. Then, by looking at the energy-momentum dispersion, it is possible to identify the energy values where nearly helical spin texture resides at the Fermi level for maximizing TAMR. For the studied $Cu/Bi_2Se_3/Co$ heterostructure, we obtained a maxmimum TAMR of 60%, then, future works will focus on other TI/FM heterostructures that could allow larger TAMR values, as required in state-of-the-art and novel magnetoresistive-based devices.

Bibliography

[1] R. V. Gorbachev, J. C. W. Song, G. L. Yu, A. V. Kretinin, F. Withers, Y. Cao, A. Mishchenko, I. V. Grigorieva, K. S. Novoselov, L. S. Levitov, and A. K. Geim, "Detecting topological currents in graphene superlattices," *Science*, vol. 346, no. 6208, pp. 448–451, 2014.

[2] A. R. Mellnik, J. S. Lee, A. Richardella, J. L. Grab, P. J. Mintun, M. H. Fischer, A. Vaezi, A. Manchon, E.-A. Kim, N. Samarth, and D. C. Ralph, "Spin-transfer torque generated by a topological insulator," *Nature*, vol. 511, no. 7510, pp. 449–451, 2014.

[3] Y. Fan, P. Upadhyaya, X. Kou, M. Lang, S. Takei, Z. Wang, J. Tang, L. He, L.-T. Chang, M. Montazeri, G. Yu, W. Jiang, T. Nie, R. N. Schwartz, Y. Tserkovnyak, and K. L. Wang, "Magnetization switching through giant spin-orbit torque in a magnetically doped topological insulator heterostructure," *Nat Mater*, vol. 13, no. 7, pp. 699–704, 2014.

[4] Y. Wang, P. Deorani, K. Banerjee, N. Koirala, M. Brahlek, S. Oh, and H. Yang, "Topological surface states originated spin-orbit torques in bi_2se_3," *Phys. Rev. Lett.*, vol. 114, p. 257202, Jun 2015.

[5] Y. Fan, X. Kou, P. Upadhyaya, Q. Shao, L. Pan, M. Lang, X. Che, J. Tang, M. Montazeri, K. Murata, L.-T. Chang, M. Akyol, G. Yu, T. Nie, K. L. Wong, J. Liu, Y. Wang, Y. Tserkovnyak, and K. L. Wang, "Electric-field control of spin-orbit torque in a magnetically doped topological insulator," *Nat Nano*, vol. 11, no. 4, pp. 352–359, 2016.

[6] Y. Shiomi, K. Nomura, Y. Kajiwara, K. Eto, M. Novak, K. Segawa, Y. Ando, and E. Saitoh, "Spin-electricity conversion induced by spin injection into topological insulators," *Phys. Rev. Lett.*, vol. 113, p. 196601, Nov 2014.

[7] P. Deorani, J. Son, K. Banerjee, N. Koirala, M. Brahlek, S. Oh, and H. Yang, "Observation of inverse spin hall effect in bismuth selenide," *Phys. Rev. B*, vol. 90, p. 094403, Sep 2014.

[8] M. Jamali, J. S. Lee, J. S. Jeong, F. Mahfouzi, Y. Lv, Z. Zhao, B. K. Nikolić, K. A. Mkhoyan, N. Samarth, and J.-P. Wang, "Giant spin pumping and inverse spin hall effect in the presence of surface and bulk spin-orbit coupling of topological insulator bi2se3," *Nano Letters*, vol. 15, no. 10, pp. 7126–7132, 2015. PMID: 26367103.

[9] J.-C. Rojas-Sánchez, S. Oyarzún, Y. Fu, A. Marty, C. Vergnaud, S. Gambarelli, L. Vila, M. Jamet, Y. Ohtsubo, A. Taleb-Ibrahimi, P. Le Fèvre, F. Bertran, N. Reyren, J.-M. George, and A. Fert, "Spin to charge conversion at room temperature by spin pumping into a new type of topological insulator: α-sn films," *Phys. Rev. Lett.*, vol. 116, p. 096602, Mar 2016.

[10] H. Wang, J. Kally, J. S. Lee, T. Liu, H. Chang, D. R. Hickey, K. A. Mkhoyan, M. Wu, A. Richardella, and N. Samarth, "Surface-state-dominated spin-charge current conversion in topological-insulator–ferromagnetic-insulator heterostructures," *Phys. Rev. Lett.*, vol. 117, p. 076601, Aug 2016.

[11] K. Kondou, R. Yoshimi, A. Tsukazaki, Y. Fukuma, J. Matsuno, K. S. Takahashi, M. Kawasaki, Y. Tokura, and Y. Otani, "Fermi-level-dependent charge-to-spin current conversion by dirac surface states of topological insulators," *Nat Phys*, vol. 12, no. 11, pp. 1027–1031, 2016.

[12] M. Z. Hasan and C. L. Kane, "Colloquium," *Rev. Mod. Phys.*, vol. 82, pp. 3045–3067, Nov 2010.

[13] X.-L. Qi and S.-C. Zhang, "Topological insulators and superconductors," *Rev. Mod. Phys.*, vol. 83, pp. 1057–1110, Oct 2011.

[14] ITRS, "Executive summary," 2015.

[15] M. M. Waldrop, "The chips are down for moore's law," *Nature News*, vol. 530, no. 7589, p. 144, 2016.

[16] A. C. Ferrari, F. Bonaccorso, V. Fal'ko, K. S. Novoselov, S. Roche, P. Boggild, S. Borini, F. H. L. Koppens, V. Palermo, N. Pugno, J. A. Garrido, R. Sordan, A. Bianco, L. Ballerini, M. Prato, E. Lidorikis, J. Kivioja, C. Marinelli, T. Ryhanen, A. Morpurgo, J. N. Coleman, V. Nicolosi, L. Colombo, A. Fert, M. Garcia-Hernandez, A. Bachtold, G. F. Schneider, F. Guinea, C. Dekker, M. Barbone, Z. Sun, C. Galiotis, A. N. Grigorenko, G. Konstantatos, A. Kis, M. Katsnelson, L. Vandersypen, A. Loiseau, V. Morandi, D. Neumaier, E. Treossi, V. Pellegrini, M. Polini, A. Tredicucci, G. M. Williams, B. Hee Hong, J.-H. Ahn, J. Min Kim, H. Zirath, B. J. van Wees, H. van der Zant, L. Occhipinti, A. Di Matteo, I. A. Kinloch, T. Seyller, E. Quesnel, X. Feng, K. Teo, N. Rupesinghe, P. Hakonen, S. R. T. Neil, Q. Tannock, T. Lofwander, and J. Kinaret, "Science and technology roadmap for graphene, related two-dimensional crystals, and hybrid systems," *Nanoscale*, vol. 7, pp. 4598–4810, 2015.

[17] M. M. Shulaker, G. Hills, N. Patil, H. Wei, H.-Y. Chen, H. S. P. Wong, and S. Mitra, "Carbon nanotube computer," *Nature*, vol. 501, pp. 526–530, Sep 2013. Letter.

[18] T. Pei, P. Zhang, Z. Zhang, C. Qiu, S. Liang, Y. Yang, S. Wang, and L.-M. Peng, "Modularized construction of general integrated circuits on individual carbon nanotubes," *Nano Letters*, vol. 14, no. 6, pp. 3102–3109, 2014. PMID: 24796796.

[19] T. Wehling, A. Black-Schaffer, and A. Balatsky, "Dirac materials," *Advances in Physics*, vol. 63, no. 1, pp. 1–76, 2014.

[20] J. Wang, S. Deng, Z. Liu, and Z. Liu, "The rare two-dimensional materials with dirac cones," *National Science Review*, vol. 2, no. 1, pp. 22–39, 2015.

[21] A. Geim, "Graphene update," *Bulletin of the American Physical Society*, vol. 55, no. 2, 2010.

[22] A. K. Geim and K. S. Novoselov, "The rise of graphene," *Nat Mater*, vol. 6, pp. 183–191, Mar 2007.

[23] F. Schwierz, "Graphene transistors," *Nat Nano*, vol. 5, pp. 487–496, Jul 2010.

[24] A. H. Castro Neto, F. Guinea, N. M. R. Peres, K. S. Novoselov, and A. K. Geim, "The electronic properties of graphene," *Rev. Mod. Phys.*, vol. 81, pp. 109–162, Jan 2009.

[25] D. Abergel, V. Apalkov, J. Berashevich, K. Ziegler, and T. Chakraborty, "Properties of graphene: a theoretical perspective," *Advances in Physics*, vol. 59, no. 4, pp. 261–482, 2010.

[26] M. J. Allen, V. C. Tung, and R. B. Kaner, "Honeycomb carbon: A review of graphene," *Chemical Reviews*, vol. 110, no. 1, pp. 132–145, 2010. PMID: 19610631.

[27] K. Nakada, M. Fujita, G. Dresselhaus, and M. S. Dresselhaus, "Edge state in graphene ribbons: Nanometer size effect and edge shape dependence," *Phys. Rev. B*, vol. 54, pp. 17954–17961, Dec 1996.

[28] J. B. Oostinga, H. B. Heersche, X. Liu, A. F. Morpurgo, and L. M. K. Vandersypen, "Gate-induced insulating state in bilayer graphene devices," *Nat Mater*, vol. 7, pp. 151–157, Feb 2008.

[29] Y. Zhang, T.-T. Tang, C. Girit, Z. Hao, M. C. Martin, A. Zettl, M. F. Crommie, Y. R. Shen, and F. Wang, "Direct observation of a widely tunable bandgap in bilayer graphene," *Nature*, vol. 459, pp. 820–823, Jun 2009.

[30] X. Liang, Y.-S. Jung, S. Wu, A. Ismach, D. L. Olynick, S. Cabrini, and J. Bokor, "Formation of bandgap and subbands in graphene nanomeshes with sub-10 nm ribbon width fabricated via nanoimprint lithography," *Nano Letters*, vol. 10, no. 7, pp. 2454–2460, 2010.

[31] J. Bai, X. Zhong, S. Jiang, Y. Huang, and X. Duan, "Graphene nanomesh," *Nat Nano*, vol. 5, pp. 190–194, Mar 2010.

[32] R. Sako, N. Hasegawa, H. Tsuchiya, and M. Ogawa, "Electronic band structures of graphene nanomeshes," in *Silicon Nanoelectronics Workshop (SNW), 2012 IEEE*, pp. 1–2, 2012.

[33] R. Sako, N. Hasegawa, H. Tsuchiya, and M. Ogawa, "Computational study on band structure engineering using graphene nanomeshes," *Journal of Applied Physics*, vol. 113, no. 14, p. 143702, 2013.

[34] V. H. Nguyen, M. C. Nguyen, H.-V. Nguyen, and P. Dollfus, "Disorder effects on electronic bandgap and transport in graphene-nanomesh-based structures," *Journal of Applied Physics*, vol. 113, no. 1, p. 013702, 2013.

[35] Z. H. Ni, T. Yu, Y. H. Lu, Y. Y. Wang, Y. P. Feng, and Z. X. Shen, "Uniaxial strain on graphene: Raman spectroscopy study and band-gap opening," *ACS Nano*, vol. 2, no. 11, pp. 2301–2305, 2008.

[36] M. R. Moslemi, M. H. Sheikhi, K. Saghafi, and M. K. Moravvej-Farshi, "Electronic properties of a dual-gated gnr-fet under uniaxial tensile strain," *Microelectronics Reliability*, vol. 52, no. 11, pp. 2579 – 2584, 2012.

[37] G. Seol and J. Guo, "Assessment of graphene nanomesh and nanoroad transistors by chemical modification," in *Electron Devices Meeting (IEDM), 2011 IEEE International*, pp. 2.3.1–2.3.4, 2011.

[38] V.-T. Tran, J. Saint-Martin, and P. Dollfus, "Modulation of bandgap and current in graphene/bn heterostructures by tuning the transverse electric field," in *Computational Electronics (IWCE), 2014 International Workshop on*, pp. 1–2, June 2014.

[39] S. Dutta and S. K. Pati, "Novel properties of graphene nanoribbons: a review," *J. Mater. Chem.*, vol. 20, pp. 8207–8223, 2010.

[40] D.-M. Sun, C. Liu, W.-C. Ren, and H.-M. Cheng, "A review of carbon nanotube- and graphene-based flexible thin-film transistors," *Small*, vol. 9, no. 8, pp. 1188–1205, 2013.

[41] G. Liang, N. Neophytou, D. Nikonov, and M. Lundstrom, "Performance projections for ballistic graphene nanoribbon field-effect transistors," *Electron Devices, IEEE Transactions on*, vol. 54, pp. 677 –682, april 2007.

[42] Y.-W. Son, M. L. Cohen, and S. G. Louie, "Half-metallic graphene nanoribbons," *Nature*, vol. 444, pp. 347–349, Nov 2006.

[43] C. Tao, L. Jiao, O. V. Yazyev, Y.-C. Chen, J. Feng, X. Zhang, R. B. Capaz, J. M. Tour, A. Zettl, S. G. Louie, H. Dai, and M. F. Crommie, "Spatially resolving edge states of chiral graphene nanoribbons," *Nat Phys*, vol. 7, pp. 616–620, Aug 2011.

[44] G. Z. Magda, X. Jin, I. Hagymasi, P. Vancso, Z. Osvath, P. Nemes-Incze, C. Hwang, L. P. Biro, and L. Tapaszto, "Room-temperature magnetic order on zigzag edges of narrow graphene nanoribbons," *Nature*, vol. 514, pp. 608–611, Oct 2014. Letter.

[45] M. Y. Han, B. Özyilmaz, Y. Zhang, and P. Kim, "Energy band-gap engineering of graphene nanoribbons," *Phys. Rev. Lett.*, vol. 98, p. 206805, May 2007.

[46] X. Li, X. Wang, L. Zhang, S. Lee, and H. Dai, "Chemically derived, ultrasmooth graphene nanoribbon semiconductors," *Science*, vol. 319, no. 5867, pp. 1229–1232, 2008.

[47] L. Tapaszto, G. Dobrik, P. Lambin, and L. P. Biro, "Tailoring the atomic structure of graphene nanoribbons by scanning tunnelling microscope lithography," *Nat Nano*, vol. 3, pp. 397–401, Jul 2008.

[48] J. Hicks, A. Tejeda, A. Taleb-Ibrahimi, M. S. Nevius, F. Wang, K. Shepperd, J. Palmer, F. Bertran, P. Le Fevre, J. Kunc, W. A. de Heer, C. Berger, and E. H. Conrad, "A wide-bandgap metal-semiconductor-metal nanostructure made entirely from graphene," *Nat Phys*, vol. 9, pp. 49–54, Jan 2013.

[49] P. Solis-Fernandez, K. Yoshida, Y. Ogawa, M. Tsuji, and H. Ago, "Dense arrays of highly aligned graphene nanoribbons produced by substrate-controlled metal-assisted etching of graphene," *Advanced Materials*, vol. 25, no. 45, pp. 6562–6568, 2013.

[50] K. A. Ritter and J. W. Lyding, "The influence of edge structure on the electronic properties of graphene quantum dots and nanoribbons," *Nat Mater*, vol. 8, pp. 235–242, Mar 2009.

[51] F. Schwierz, "Graphene transistors: Status, prospects, and problems," *Proceedings of the IEEE*, vol. 101, pp. 1567–1584, July 2013.

[52] N. Akhavan, G. Jolley, G. Membreno, J. Antoszewski, and L. Faraone, "Study of uniformly doped graphene nanoribbon transistor (gnr) fet using quantum simulation," in *Optoelectronic and Microelectronic Materials Devices (COMMAD), 2012 Conference on*, pp. 67–68, 2012.

[53] V. Dhand, K. Y. Rhee, H. Ju Kim, and D. Ho Jung, "A comprehensive review of graphene nanocomposites: Research status and trends," *Journal of Nanomaterials*, vol. 2013, p. 14, 2013.

[54] M. L. Curri, R. Comparelli, M. Striccoli, and A. Agostiano, "Emerging methods for fabricating functional structures by patterning and assembling engineered nanocrystals," *Phys. Chem. Chem. Phys.*, vol. 12, pp. 11197–11207, 2010.

[55] L. Dossel, L. Gherghel, X. Feng, and K. Mullen, "Graphene nanoribbons by chemists: Nanometer-sized, soluble, and defect-free," *Angewandte Chemie International Edition*, vol. 50, no. 11, pp. 2540–2543, 2011.

[56] K. S. Novoselov, V. I. Fal[prime]ko, L. Colombo, P. R. Gellert, M. G. Schwab, and K. Kim, "A roadmap for graphene," *Nature*, vol. 490, pp. 192–200, Oct 2012.

[57] X. Wang, Y. Ouyang, L. Jiao, H. Wang, L. Xie, J. Wu, J. Guo, and H. Dai, "Graphene nanoribbons with smooth edges behave as quantum wires," *Nat Nano*, vol. 6, pp. 563–567, Sep 2011.

[58] M. Kim, N. S. Safron, E. Han, M. S. Arnold, and P. Gopalan, "Fabrication and characterization of large-area, semiconducting nanoperforated graphene materials," *Nano Letters*, vol. 10, no. 4, pp. 1125–1131, 2010. PMID: 20192229.

[59] A. Sinitskii and J. M. Tour, "Patterning graphene through the self-assembled templates: Toward periodic two-dimensional graphene nanostructures with semiconductor properties," *Journal of the American Chemical Society*, vol. 132, no. 42, pp. 14730–14732, 2010.

[60] T. G. Pedersen, C. Flindt, J. Pedersen, N. A. Mortensen, A.-P. Jauho, and K. Pedersen, "Graphene antidot lattices: Designed defects and spin qubits," *Phys. Rev. Lett.*, vol. 100, p. 136804, Apr 2008.

[61] J. Eroms and D. Weiss, "Weak localization and transport gap in graphene antidot lattices," *New Journal of Physics*, vol. 11, no. 9, p. 095021, 2009.

[62] Q. Guo, J. Zhang, Y. He, J. Kang, H. Qian, Y. Wang, and Z. Yu, "The electronic structure of graphene nanomesh," in *Solid-State and Integrated Circuit Technology (ICSICT), 2010 10th IEEE International Conference on*, pp. 1811–1813, 2010.

[63] K. Lopata, R. Thorpe, S. Pistinner, X. Duan, and D. Neuhauser, "Graphene nanomeshes: Onset of conduction band gaps," *Chemical Physics Letters*, vol. 498, no. 4-6, pp. 334–337, 2010.

[64] H. Jippo, M. Ohfuchi, and C. Kaneta, "Theoretical study on electron transport properties of graphene sheets with two- and one-dimensional periodic nanoholes," *Phys. Rev. B*, vol. 84, p. 075467, Aug 2011.

[65] T. Chu and Z. Chen, "Graphene nanomesh contacts and its transport properties," in *Device Research Conference (DRC), 2012 70th Annual*, pp. 185–186, 2012.

[66] M. Vanevic, V. M. Stojanovic, and M. Kindermann, "Character of electronic states in graphene antidot lattices: Flat bands and spatial localization," *Phys. Rev. B*, vol. 80, p. 045410, Jul 2009.

[67] W. Liu, Z. F. Wang, Q. W. Shi, J. Yang, and F. Liu, "Band-gap scaling of graphene nanohole superlattices," *Phys. Rev. B*, vol. 80, p. 233405, Dec 2009.

[68] S. Hossain, F. Al-Dirini, F. Hossain, and E. Skafidas, "Enhanced thermoelectric properties of engineered graphene nano-ribbons with nano-pores," in *Nanotechnology (IEEE-NANO), 2014 IEEE 14th International Conference on*, pp. 598–601, Aug 2014.

[69] H. Sadeghi, L. Algaragholy, T. Pope, S. Bailey, D. Visontai, D. Manrique, J. Ferrer, V. Garcia-Suarez, S. Sangtarash, and C. J. Lambert, "Graphene sculpturene

nanopores for dna nucleobase sensing," *The Journal of Physical Chemistry B*, vol. 118, no. 24, pp. 6908–6914, 2014. PMID: 24849015.

[70] H. Zhang, C.-X. Liu, X.-L. Qi, X. Dai, Z. Fang, and S.-C. Zhang, "Topological insulators in bi2se3, bi2te3 and sb2te3 with a single dirac cone on the surface," *Nat Phys*, vol. 5, no. 6, pp. 438–442, 2009.

[71] C.-X. Liu, X.-L. Qi, H. Zhang, X. Dai, Z. Fang, and S.-C. Zhang, "Model hamiltonian for topological insulators," *Phys. Rev. B*, vol. 82, p. 045122, Jul 2010.

[72] C. Kane and J. Moore, "Topological insulators," *Physics World*, vol. 24, no. 02, p. 32, 2011.

[73] Y. Xia, D. Qian, D. Hsieh, L. Wray, A. Pal, H. Lin, A. Bansil, D. Grauer, Y. S. Hor, R. J. Cava, and M. Z. Hasan, "Observation of a large-gap topological-insulator class with a single dirac cone on the surface," *Nat Phys*, vol. 5, no. 6, pp. 398–402, 2009.

[74] M. Noei, M. Moradinasab, and M. Fathipour, "A computational study of ballistic graphene nanoribbon field effect transistors," *Physica E: Low-dimensional Systems and Nanostructures*, vol. 44, no. 7-8, pp. 1780 – 1786, 2012.

[75] S. Datta, "Nanoelectronic devices: A unified view," *ArXiv e-prints*, Sept. 2008.

[76] C. Lewenkopf and E. Mucciolo, "The recursive green's function method for graphene," *Journal of Computational Electronics*, vol. 12, no. 2, pp. 203–231, 2013.

[77] D. A. Areshkin and B. K. Nikolić "Electron density and transport in top-gated graphene nanoribbon devices: First-principles green function algorithms for systems containing a large number of atoms," *Phys. Rev. B*, vol. 81, p. 155450, Apr 2010.

[78] S. Bruzzone, G. Iannaccone, N. Marzari, and G. Fiori, "An open-source multiscale framework for the simulation of nanoscale devices," *Electron Devices, IEEE Transactions on*, vol. 61, pp. 48–53, Jan 2014.

[79] A. Faghaninia, J. W. Ager, III, and C. S. Lo, "ab initio electronic transport model with explicit solution to the linearized boltzmann transport equation," *ArXiv e-prints*, Jan. 2015.

[80] S. Datta, "Nanoscale device modeling: the green's function method," *Superlattices and Microstructures*, vol. 28, no. 4, pp. 253 – 278, 2000.

[81] S. Datta, *Quantum Transport: Atom to Transistor*. Cambridge University Press, 2005.

[82] S. Datta, *Quantum Transport: Atom to Transistor*. Cambridge University Press, 2013.

[83] S. Datta, "Nanoscale device modeling: the green's function method," *Superlattices and Microstructures*, vol. 28, no. 4, pp. 253 – 278, 2000.

[84] I. Zutic, J. Fabian, and S. Das Sarma, "Spintronics: Fundamentals and applications," *Rev. Mod. Phys.*, vol. 76, pp. 323–410, Apr 2004.

[85] S. Wolf, A. Chtchelkanova, and D. Treger, "Spintronics - a retrospective and perspective," *IBM Journal of Research and Development*, vol. 50, pp. 101–110, Jan 2006.

[86] D. Nikonov, G. Bourianoff, and P. Gargini, "Power dissipation in spintronic devices out of thermodynamic equilibrium," *Journal of Superconductivity and Novel Magnetism*, vol. 19, no. 6, pp. 497–513, 2006.

[87] B. K. Nikolić, L. P. Zarbo, and S. Souma, "Spin currents in semiconductor nanostructures: A nonequilibrium green-function approach," *ArXiv e-prints*, July 2009.

[88] B. K. Nikolić, S. Souma, L. P. Zarbo, and J. Sinova, "Nonequilibrium spin hall accumulation in ballistic semiconductor nanostructures," *Phys. Rev. Lett.*, vol. 95, p. 046601, Jul 2005.

[89] M. Scheid, D. Bercioux, and K. Richter, "Zeeman ratchets: pure spin current generation in mesoscopic conductors with non-uniform magnetic fields," *New Journal of Physics*, vol. 9, no. 11, p. 401, 2007.

[90] P.-H. Chang, H. Liu, and B. Nikolic, "First-principles versus semi-empirical modeling of global and local electronic transport properties of graphene nanopore-based sensors for dna sequencing," *Journal of Computational Electronics*, vol. 13, no. 4, pp. 847–856, 2014.

[91] C.-L. Chen, C.-R. Chang, and B. K. Nikolić, "Quantum coherence and its dephasing in the giant spin hall effect and nonlocal voltage generated by magnetotransport through multiterminal graphene bars," *Phys. Rev. B*, vol. 85, p. 155414, Apr 2012.

[92] A. Soumyanarayanan, N. Reyren, A. Fert, and C. Panagopoulos, "Emergent phenomena induced by spin-orbit coupling at surfaces and interfaces," *Nature*, vol. 539, no. 7630, pp. 509–517, 2016.

[93] A. Cresti, B. K. Nikolić, J. H. Garcia, and S. Roche, "Charge, spin and valley hall effects in disordered graphene," *La Rivista del Nuovo Cimento*, no. 12, pp. 587–667, 2016.

[94] E. I. Rashba, "Properties of semiconductors with an extremum loop. 1. cyclotron and combinational resonance in a magnetic field perpendicular to the plane of the loop," *Sov. Phys. Solid State*, vol. 2, pp. 1224–1238, 1960.

[95] V. Edelstein, "Spin polarization of conduction electrons induced by electric current in two-dimensional asymmetric electron systems," *Solid State Communications*, vol. 73, no. 3, pp. 233 – 235, 1990.

[96] C. L. Kane and E. J. Mele, "Quantum spin hall effect in graphene," *Phys. Rev. Lett.*, vol. 95, p. 226801, Nov 2005.

[97] J. Balakrishnan, G. K. W. Koon, M. Jaiswal, A. H. C. Neto, and B. Ozyilmaz, "Colossal enhancement of spin-orbit coupling in weakly hydrogenated graphene," *Nat Phys*, vol. 9, no. 5, pp. 284–287, 2013.

[98] D. V. Tuan, F. Ortmann, D. Soriano, S. O. Valenzuela, and S. Roche, "Pseudospin-driven spin relaxation mechanism in graphene," *Nat Phys*, vol. 10, no. 11, pp. 857–863, 2014.

[99] P.-H. Chang, T. Markussen, S. Smidstrup, K. Stokbro, and B. K. Nikolić, "Nonequilibrium spin texture within a thin layer below the surface of current-carrying topological insulator bi_2se_3: A first-principles quantum transport study," *Phys. Rev. B*, vol. 92, p. 201406, Nov 2015.

[100] S. Manipatruni, D. E. Nikonov, and I. A. Young, "Spin-orbit logic with magnetoelectric nodes: A scalable charge mediated nonvolatile spintronic logic," *arXiv preprint arXiv:1512.05428*, 2015.

[101] A. Azman, Z. Johari, and R. Ismail, "Performance evaluation of dual-channel armchair graphene nanoribbon field-effect transistor," in *Semiconductor Electronics (ICSE), 2014 IEEE International Conference on*, pp. 138–141, Aug 2014.

[102] Y.-Y. Chen, A. Sangai, M. Gholipour, and D. Chen, "Schottky-barrier-type graphene nano-ribbon field-effect transistors: A study on compact modeling, process variation, and circuit performance," in *Nanoscale Architectures (NANOARCH), 2013 IEEE/ACM International Symposium on*, pp. 82–88, July 2013.

[103] Y. Khatami, J. Kang, and K. Banerjee, "Graphene nanoribbon based negative resistance device for ultra-low voltage digital logic applications," *Applied Physics Letters*, vol. 102, no. 4, p. 043114, 2013.

[104] N. Ghobadi and M. Pourfath, "A comparative study of tunneling fets based on graphene and gnr heterostructures," *Electron Devices, IEEE Transactions on*, vol. 61, pp. 186–192, Jan 2014.

[105] L.-T. Tung, M. Mateus, and E. Kan, "Tri-gate graphene nanoribbon transistors with transverse-field bandgap modulation," *Electron Devices, IEEE Transactions on*, vol. 61, pp. 3329–3334, Sept 2014.

[106] P. Zhao, R. Feenstra, G. Gu, and D. Jena, "Symfet: A proposed symmetric graphene tunneling field-effect transistor," *Electron Devices, IEEE Transactions on*, vol. 60, no. 3, pp. 951–957, 2013.

[107] A. Kumar, V. Kumar, S. Agarwal, A. Basak, N. Jain, A. Bulusu, and S. Manhas, "Nitrogen-terminated semiconducting zigzag gnr fet with negative differential resistance," *Nanotechnology, IEEE Transactions on*, vol. 13, pp. 16–22, Jan 2014.

[108] Q. Zhang, Y. Lu, C. Richter, D. Jena, and A. Seabaugh, "Optimum bandgap and supply voltage in tunnel fets," *Electron Devices, IEEE Transactions on*, vol. 61, pp. 2719–2724, Aug 2014.

[109] H. Mohamadpour and A. Asgari, "Graphene nanoribbon tunneling field effect transistors," *Physica E: Low-dimensional Systems and Nanostructures*, vol. 46, no. 0, pp. 270 – 273, 2012.

[110] M. Gholipour, N. Masoumi, Y.-Y. Chen, D. Chen, and M. Pourfath, "Asymmetric gate schottky-barrier graphene nanoribbon fets for low-power design," *Electron Devices, IEEE Transactions on*, vol. 61, pp. 4000–4006, Dec 2014.

[111] W. Mehr, J. Dabrowski, J. Scheytt, G. Lippert, Y.-H. Xie, M. Lemme, M. Ostling, and G. Lupina, "Vertical graphene base transistor," *Electron Device Letters, IEEE*, vol. 33, pp. 691 –693, may 2012.

[112] J. Knoch and M. Muller, "Electrostatic doping - controlling the properties of carbon-based fets with gates," *Nanotechnology, IEEE Transactions on*, vol. 13, pp. 1044–1052, Nov 2014.

[113] M. Muller, A. Gumprich, F. Schutte, K. Kallis, U. Kunzelmann, S. Engels, C. Stampfer, N. Wilck, and J. Knoch, "Buried triple-gate structures for advanced field-effect transistor devices," *Microelectronic Engineering*, vol. 119, no. 0, pp. 95 – 99, 2014. Micro/Nano Devices and Systems 2013.

[114] J. Yu, G. Liu, A. V. Sumant, V. Goyal, and A. A. Balandin, "Graphene-on-diamond devices with increased current-carrying capacity: Carbon sp2-on-sp3 technology," *Nano Letters*, vol. 12, no. 3, pp. 1603–1608, 2012.

[115] A. E. Moutaouakil, H.-C. Kang, H. Handa, H. Fukidome, T. Suemitsu, E. Sano, M. Suemitsu, and T. Otsuji, "Room temperature logic inverter on epitaxial graphene-on-silicon device," *Japanese Journal of Applied Physics*, vol. 50, no. 7, p. 070113, 2011.

[116] L.-T. Tung and E. Kan, "Sharp switching by field-effect bandgap modulation in all-graphene side-gate transistors," *Electron Devices Society, IEEE Journal of the*, vol. PP, no. 99, pp. 1–1, 2015.

[117] H. Wang, S. Chang, Y. Hu, H. He, J. He, Q. Huang, F. He, and G. Wang, "A novel barrier controlled tunnel fet," *Electron Device Letters, IEEE*, vol. 35, pp. 798–800, July 2014.

[118] V. Hung Nguyen, J. Saint-Martin, D. Querlioz, F. Mazzamuto, A. Bournel, Y.-M. Niquet, and P. Dollfus, "Bandgap nanoengineering of graphene tunnel diodes

and tunnel transistors to control the negative differential resistance," *Journal of Computational Electronics*, vol. 12, no. 2, pp. 85–93, 2013.

[119] N. Hasegawa, R. Sako, H. Tsuchiya, and M. Ogawa, "Band structure and electron transport in multi-junction graphene nanoribbons," in *Silicon Nanoelectronics Workshop (SNW), 2012 IEEE*, pp. 1 –2, june 2012.

[120] C. Pan and A. Naeemi, "Device- and system-level performance modeling for graphene p-n junction logic," in *Quality Electronic Design (ISQED), 2012 13th International Symposium on*, pp. 262 –269, march 2012.

[121] D. Unluer, F. Tseng, and A. Ghosh, "Physics-based gnrfet compact model for digital circuit design," in *Semiconductor Device Research Symposium (ISDRS), 2011 International*, pp. 1 –2, dec. 2011.

[122] C. Gomes da Rocha, R. Tuovinen, R. van Leeuwen, and P. Koskinen, "Curvature in graphene nanoribbons generates temporally and spatially focused electric currents," *Nanoscale*, pp. –, 2015.

[123] J. Cai, C. A. Pignedoli, L. Talirz, P. Ruffieux, H. Sode, L. Liang, V. Meunier, R. Berger, R. Li, X. Feng, K. Mullen, and R. Fasel, "Graphene nanoribbon heterojunctions," *Nat Nano*, vol. 9, pp. 896–900, Nov 2014. Letter.

[124] H. Hosokawa, R. Sako, H. Ando, and H. Tsuchiya, "Performance comparisons of bilayer graphene and graphene nanoribbon field-effect transistors under ballistic transport," *Japanese Journal of Applied Physics*, vol. 49, no. 11, p. 110207, 2010.

[125] R. Sako, H. Tsuchiya, and M. Ogawa, "Influence of band-gap opening on ballistic electron transport in bilayer graphene and graphene nanoribbon fets," *Electron Devices, IEEE Transactions on*, vol. 58, no. 10, pp. 3300–3306, 2011.

[126] H. Karamitaheri, M. Pourfath, R. Faez, and H. Kosina, "Atomistic study of the lattice thermal conductivity of rough graphene nanoribbons," *Electron Devices, IEEE Transactions on*, vol. 60, pp. 2142–2147, July 2013.

[127] K. Tahy, H. Xing, and D. Jena, "Graphene nanoribbon fets for digital electronics: experiment and modeling," *International Journal of Circuit Theory and Applications*, vol. 41, no. 6, pp. 603–607, 2013.

[128] S. S. Datta, D. R. Strachan, S. M. Khamis, and A. T. C. Johnson, "Crystallographic etching of few-layer graphene," *Nano Letters*, vol. 8, no. 7, pp. 1912–1915, 2008. PMID: 18570483.

[129] W. S. Hwang, K. Tahy, X. Li, H. G. Xing, A. C. Seabaugh, C. Y. Sung, and D. Jena, "Transport properties of graphene nanoribbon transistors on chemical-vapor-deposition grown wafer-scale graphene," *Applied Physics Letters*, vol. 100, no. 20, p. 203107, 2012.

[130] C.-H. Huang, C.-Y. Su, T. Okada, L.-J. Li, K.-I. Ho, P.-W. Li, I.-H. Chen, C. Chou, C.-S. Lai, and S. Samukawa, "Ultra-low-edge-defect graphene nanoribbons patterned by neutral beam," *Carbon*, vol. 61, no. 0, pp. 229 – 235, 2013.

[131] I. Martin-Fernandez, D. Wang, and Y. Zhang, "Direct growth of graphene nanoribbons for large-scale device fabrication," *Nano Letters*, vol. 12, no. 12, pp. 6175–6179, 2012.

[132] R. M. Jacobberger, B. Kiraly, M. Fortin-Deschenes, P. L. Levesque, K. M. McElhinny, G. J. Brady, R. Rojas Delgado, S. Singha Roy, A. Mannix, M. G. Lagally, P. G. Evans, P. Desjardins, R. Martel, M. C. Hersam, N. P. Guisinger, and M. S. Arnold, "Direct oriented growth of armchair graphene nanoribbons on germanium," *Nat Commun*, vol. 6, Aug 2015. Article.

[133] G. Xue, Q. Tang, Y. Tong, and Y. Liu, "Size-controlled ambipolar graphene nanoribbon transistors by an all-dry mask method," *Synthetic Metals*, vol. 205, pp. 6 – 10, 2015.

[134] J. Cai, P. Ruffieux, R. Jaafar, M. Bieri, T. Braun, S. Blankenburg, M. Muoth, A. P. Seitsonen, M. Saleh, X. Feng, K. Mullen, and R. Fasel, "Atomically precise bottom-up fabrication of graphene nanoribbons," *Nature*, vol. 466, pp. 470–473, Jul 2010.

[135] T. H. Vo, M. Shekhirev, D. A. Kunkel, M. D. Morton, E. Berglund, L. Kong, P. M. Wilson, P. A. Dowben, A. Enders, and A. Sinitskii, "Large-scale solution synthesis of narrow graphene nanoribbons," *Nat Commun*, vol. 5, Feb 2014. Article.

[136] C. Sung, "Post si cmos graphene nanoelectronics," in *VLSI Technology, Systems and Applications (VLSI-TSA), 2011 International Symposium on*, pp. 1–2, 2011.

[137] D. Wang, H. Tian, I. Martin-Fernandez, Y. Yang, T.-L. Ren, and Y. Zhang, "Large-scale fabrication of graphene-based electronic and mems devices," in *Electron Devices Meeting (IEDM), 2014 IEEE International*, pp. 15.2.1–15.2.4, Dec 2014.

[138] A. D. Liao, J. Z. Wu, X. Wang, K. Tahy, D. Jena, H. Dai, and E. Pop, "Thermally limited current carrying ability of graphene nanoribbons," *Phys. Rev. Lett.*, vol. 106, p. 256801, Jun 2011.

[139] C. Bronner, F. Leyssner, S. Stremlau, M. Utecht, P. Saalfrank, T. Klamroth, and P. Tegeder, "Electronic structure of a subnanometer wide bottom-up fabricated graphene nanoribbon: End states, band gap, and dispersion," *Phys. Rev. B*, vol. 86, p. 085444, Aug 2012.

[140] C. Bronner, M. Utecht, A. Haase, P. Saalfrank, T. Klamroth, and P. Tegeder, "Electronic structure changes during the surface-assisted formation of a graphene nanoribbon," *The Journal of Chemical Physics*, vol. 140, no. 2, pp. –, 2014.

[141] P. B. Bennett, Z. Pedramrazi, A. Madani, Y.-C. Chen, D. G. de Oteyza, C. Chen, F. R. Fischer, M. F. Crommie, and J. Bokor, "Bottom-up graphene nanoribbon field-effect transistors," *Applied Physics Letters*, vol. 103, no. 25, pp. –, 2013.

[142] K. T. Kim, J. W. Jung, and W. H. Jo, "Synthesis of graphene nanoribbons with various widths and its application to thin-film transistor," *Carbon*, vol. 63, no. 0, pp. 202 – 209, 2013.

[143] K. T. Kim, J. W. Lee, and W. H. Jo, "Charge-transport tuning of solution-processable graphene nanoribbons by substitutional nitrogen doping," *Macromolecular Chemistry and Physics*, vol. 214, no. 23, pp. 2768–2773, 2013.

[144] D. E. Nikonov and I. A. Young, "Benchmarking of beyond-cmos exploratory devices for logic integrated circuits," *IEEE Journal on Exploratory Solid-State Computational Devices and Circuits*, vol. 1, pp. 3–11, Dec 2015.

[145] M. Lemme, "Graphene for microelectronics: Can it make a difference?," in *ESSCIRC (ESSCIRC), 2012 Proceedings of the*, pp. 25 –27, sept. 2012.

[146] M. Lemme, S. Vaziri, A. Smith, and M. Ostling, "Alternative graphene devices: beyond field effect transistors," in *Device Research Conference (DRC), 2012 70th Annual*, pp. 24a –24b, june 2012.

[147] L. Britnell, R. V. Gorbachev, R. Jalil, B. D. Belle, F. Schedin, A. Mishchenko, T. Georgiou, M. I. Katsnelson, L. Eaves, S. V. Morozov, N. M. R. Peres, J. Leist, A. K. Geim, K. S. Novoselov, and L. A. Ponomarenko, "Field-effect tunneling transistor based on vertical graphene heterostructures," *Science*, vol. 335, no. 6071, pp. 947–950, 2012.

[148] D. Reddy, L. Register, E. Tutuc, A. MacDonald, and S. K. Banerjee, "Bilayer pseudospin field effect transistor (bisfet): A proposed logic device and circuits," in *Device Research Conference, 2009. DRC 2009*, pp. 67–68, 2009.

[149] X. Yang and K. Mohanram, "Ambipolar electronics," tech. rep., Rice University ECE Department Technical Report, 03 2010.

[150] H. Li, Q. Zhang, C. Liu, S. Xu, and P. Gao, "Ambipolar to unipolar conversion in graphene field-effect transistors," *ACS Nano*, vol. 5, no. 4, pp. 3198–3203, 2011.

[151] R. Sordan, F. Traversi, and V. Russo, "Logic gates with a single graphene transistor," *Applied Physics Letters*, vol. 94, no. 7, p. 073305, 2009.

[152] S.-L. Li, H. Miyazaki, A. Kumatani, A. Kanda, and K. Tsukagoshi, "Low operating bias and matched input-output characteristics in graphene logic inverters," *Nano Letters*, vol. 10, no. 7, pp. 2357–2362, 2010.

[153] F. Traversi, V. Russo, and R. Sordan, "Integrated complementary graphene inverter," *Applied Physics Letters*, vol. 94, no. 22, p. 223312, 2009.

[154] L. G. Rizzi, M. Bianchi, A. Behnam, E. Carrion, E. Guerriero, L. Polloni, E. Pop, and R. Sordan, "Cascading wafer-scale integrated graphene complementary inverters under ambient conditions," *Nano Letters*, vol. 12, no. 8, pp. 3948–3953, 2012.

[155] G. Saha, A. Saha, and A. Harun-ur Rashid, "Low power dissipation logic inverter design using atomic-level width controlled gnr-fets," in *Electrical and Computer Engineering (ICECE), 2014 International Conference on*, pp. 160–163, Dec 2014.

[156] G. Vignale, "Ten years of spin hall effect," *Journal of Superconductivity and Novel Magnetism*, vol. 23, no. 1, p. 3, 2009.

[157] J. Sinova, S. O. Valenzuela, J. Wunderlich, C. H. Back, and T. Jungwirth, "Spin hall effects," *Rev. Mod. Phys.*, vol. 87, pp. 1213–1260, Oct 2015.

[158] Y. K. Kato, R. C. Myers, A. C. Gossard, and D. D. Awschalom, "Observation of the spin hall effect in semiconductors," *Science*, vol. 306, no. 5703, pp. 1910–1913, 2004.

[159] J. Wunderlich, B. Kaestner, J. Sinova, and T. Jungwirth, "Experimental observation of the spin-hall effect in a two-dimensional spin-orbit coupled semiconductor system," *Phys. Rev. Lett.*, vol. 94, p. 047204, Feb 2005.

[160] S. O. Valenzuela and M. Tinkham, "Direct electronic measurement of the spin hall effect," *Nature*, vol. 442, pp. 176–179, Jul 2006.

[161] E. Saitoh, M. Ueda, H. Miyajima, and G. Tatara, "Conversion of spin current into charge current at room temperature: Inverse spin-hall effect," *Applied Physics Letters*, vol. 88, no. 18, p. 182509, 2006.

[162] W. Han, R. K. Kawakami, M. Gmitra, and J. Fabian, "Graphene spintronics," *Nat Nano*, vol. 9, pp. 794–807, Oct 2014. Review.

[163] S. Roche, J. Akerman, B. Beschoten, J.-C. Charlier, M. Chshiev, S. P. Dash, B. Dlubak, J. Fabian, A. Fert, M. GuimarÃ£es, F. Guinea, I. Grigorieva, C. SchÃ¶nenberger, P. Seneor, C. Stampfer, S. O. Valenzuela, X. Waintal, and B. van Wees, "Graphene spintronics: the european flagship perspective," *2D Materials*, vol. 2, no. 3, p. 030202, 2015.

[164] D. Huertas-Hernando, F. Guinea, and A. Brataas, "Spin-orbit coupling in curved graphene, fullerenes, nanotubes, and nanotube caps," *Phys. Rev. B*, vol. 74, p. 155426, Oct 2006.

[165] M. Gmitra, S. Konschuh, C. Ertler, C. Ambrosch-Draxl, and J. Fabian, "Band-structure topologies of graphene: Spin-orbit coupling effects from first principles," *Phys. Rev. B*, vol. 80, p. 235431, Dec 2009.

[166] A. H. Castro Neto and F. Guinea, "Impurity-induced spin-orbit coupling in graphene," *Phys. Rev. Lett.*, vol. 103, p. 026804, Jul 2009.

[167] V. K. Dugaev, E. Y. Sherman, and J. Barnaś, "Spin dephasing and pumping in graphene due to random spin-orbit interaction," *Phys. Rev. B*, vol. 83, p. 085306, Feb 2011.

[168] N. Tombros, C. Jozsa, M. Popinciuc, H. T. Jonkman, and B. J. van Wees, "Electronic spin transport and spin precession in single graphene layers at room temperature," *Nature*, vol. 448, pp. 571–574, Aug 2007.

[169] K. Pi, W. Han, K. M. McCreary, A. G. Swartz, Y. Li, and R. K. Kawakami, "Manipulation of spin transport in graphene by surface chemical doping," *Phys. Rev. Lett.*, vol. 104, p. 187201, May 2010.

[170] B. Dlubak, M.-B. Martin, C. Deranlot, B. Servet, S. Xavier, R. Mattana, M. Sprinkle, C. Berger, W. A. De Heer, F. Petroff, A. Anane, P. Seneor, and A. Fert, "Highly efficient spin transport in epitaxial graphene on sic," *Nat Phys*, vol. 8, pp. 557–561, Jul 2012.

[171] M. H. D. Guimarães, P. J. Zomer, J. Ingla-Aynés, J. C. Brant, N. Tombros, and B. J. van Wees, "Controlling spin relaxation in hexagonal bn-encapsulated graphene with a transverse electric field," *Phys. Rev. Lett.*, vol. 113, p. 086602, Aug 2014.

[172] M. Droegeler, F. Volmer, M. Wolter, B. TerrÃ©s, K. Watanabe, T. Taniguchi, G. GÃŒntherodt, C. Stampfer, and B. Beschoten, "Nanosecond spin lifetimes in single- and few-layer graphene-hbn heterostructures at room temperature," *Nano Letters*, vol. 14, no. 11, pp. 6050–6055, 2014. PMID: 25291305.

[173] M. V. Kamalakar, C. Groenveld, A. Dankert, and S. P. Dash, "Long distance spin communication in chemical vapour deposited graphene," *Nature Communications*, vol. 6, pp. 6766 EP –, Apr 2015. Article.

[174] B. Raes, J. E. Scheerder, M. V. Costache, F. Bonell, J. F. Sierra, J. Cuppens, J. Van de Vondel, and S. O. Valenzuela, "Determination of the spin-lifetime anisotropy in graphene using oblique spin precession," *Nature Communications*, vol. 7, pp. 11444 EP –, May 2016. Article.

[175] J. Balakrishnan, G. K. W. Koon, A. Avsar, Y. Ho, J. H. Lee, M. Jaiswal, S.-J. Baeck, J.-H. Ahn, A. Ferreira, M. A. Cazalilla, A. H. C. Neto, and B. Özyilmaz, "Giant spin hall effect in graphene grown by chemical vapour deposition," *Nature Communications*, vol. 5, pp. 4748 EP –, Sep 2014. Article.

[176] A. Ferreira, T. G. Rappoport, M. A. Cazalilla, and A. H. Castro Neto, "Extrinsic spin hall effect induced by resonant skew scattering in graphene," *Phys. Rev. Lett.*, vol. 112, p. 066601, Feb 2014.

[177] H.-Y. Yang, C. Huang, H. Ochoa, and M. A. Cazalilla, "Extrinsic spin hall effect from anisotropic rashba spin-orbit coupling in graphene," *Phys. Rev. B*, vol. 93, p. 085418, Feb 2016.

[178] Y. Wang, X. Cai, J. Reutt-Robey, and M. S. Fuhrer, "Neutral-current hall effects in disordered graphene," *Phys. Rev. B*, vol. 92, p. 161411, Oct 2015.

[179] A. A. Kaverzin and B. J. van Wees, "Electron transport nonlocality in monolayer graphene modified with hydrogen silsesquioxane polymerization," *Phys. Rev. B*, vol. 91, p. 165412, Apr 2015.

[180] D. A. Abanin, A. V. Shytov, L. S. Levitov, and B. I. Halperin, "Nonlocal charge transport mediated by spin diffusion in the spin hall effect regime," *Phys. Rev. B*, vol. 79, p. 035304, Jan 2009.

[181] D. Van Tuan, F. Ortmann, A. W. Cummings, D. Soriano, and S. Roche, "Spin dynamics and relaxation in graphene dictated by electron-hole puddles," *Scientific Reports*, vol. 6, pp. 21046 EP –, Feb 2016. Article.

[182] D. Van Tuan and S. Roche, "Spin manipulation in graphene by chemically induced pseudospin polarization," *Phys. Rev. Lett.*, vol. 116, p. 106601, Mar 2016.

[183] C.-L. Chen, C.-R. Chang, and B. K. Nikolić, "Quantum coherence and its dephasing in the giant spin hall effect and nonlocal voltage generated by magnetotransport through multiterminal graphene bars," *Phys. Rev. B*, vol. 85, p. 155414, Apr 2012.

[184] P. Streda, "Quantised hall effect in a two-dimensional periodic potential," *Journal of Physics C: Solid State Physics*, vol. 15, no. 36, p. L1299, 1982.

[185] N. A. Sinitsyn, J. E. Hill, H. Min, J. Sinova, and A. H. MacDonald, "Charge and spin hall conductivity in metallic graphene," *Phys. Rev. Lett.*, vol. 97, p. 106804, Sep 2006.

[186] I. A. Ado, I. A. Dmitriev, P. M. Ostrovsky, and M. Titov, "Anomalous hall effect in a 2d rashba ferromagnet," *Phys. Rev. Lett.*, vol. 117, p. 046601, Jul 2016.

[187] M. Milletarı and A. Ferreira, "Crossover to the anomalous quantum regime in the extrinsic spin hall effect of graphene," *Phys. Rev. B*, vol. 94, p. 201402, Nov. 2016.

[188] M. Milletarı and A. Ferreira, "Quantum diagrammatic theory of the extrinsic spin hall effect in graphene," *Phys. Rev. B*, vol. 94, p. 134202, Oct. 2016.

[189] E. Sutter, P. Albrecht, B. Wang, M.-L. Bocquet, L. Wu, Y. Zhu, and P. Sutter, "Arrays of ru nanoclusters with narrow size distribution templated by monolayer graphene on ru," *Surface Science*, vol. 605, no. 17-18, pp. 1676 – 1684, 2011. Graphene Surfaces and Interfaces.

[190] K. Pi, K. M. McCreary, W. Bao, W. Han, Y. F. Chiang, Y. Li, S.-W. Tsai, C. N. Lau, and R. K. Kawakami, "Electronic doping and scattering by transition metals on graphene," *Phys. Rev. B*, vol. 80, p. 075406, Aug 2009.

[191] M. I. Katsnelson, F. Guinea, and A. K. Geim, "Scattering of electrons in graphene by clusters of impurities," *Phys. Rev. B*, vol. 79, p. 195426, May 2009.

[192] K. M. McCreary, K. Pi, A. G. Swartz, W. Han, W. Bao, C. N. Lau, F. Guinea, M. I. Katsnelson, and R. K. Kawakami, "Effect of cluster formation on graphene mobility," *Phys. Rev. B*, vol. 81, p. 115453, Mar 2010.

[193] A. Cresti, D. Van Tuan, D. Soriano, A. W. Cummings, and S. Roche, "Multiple quantum phases in graphene with enhanced spin-orbit coupling: From the quantum spin hall regime to the spin hall effect and a robust metallic state," *Phys. Rev. Lett.*, vol. 113, p. 246603, Dec 2014.

[194] M. Büttiker, "Four-terminal phase-coherent conductance," *Phys. Rev. Lett.*, vol. 57, pp. 1761–1764, Oct 1986.

[195] G. Mihajlović, J. E. Pearson, M. A. Garcia, S. D. Bader, and A. Hoffmann, "Negative nonlocal resistance in mesoscopic gold hall bars: Absence of the giant spin hall effect," *Phys. Rev. Lett.*, vol. 103, p. 166601, Oct 2009.

[196] Z. Wang, H. Liu, H. Jiang, and X. C. Xie, "Numerical study of the giant nonlocal resistance in spin-orbit coupled graphene," *Phys. Rev. B*, vol. 94, p. 035409, Jul 2016.

[197] C. Weeks, J. Hu, J. Alicea, M. Franz, and R. Wu, "Engineering a robust quantum spin hall state in graphene via adatom deposition," *Phys. Rev. X*, vol. 1, p. 021001, Oct 2011.

[198] A. Avsar, J. H. Lee, G. K. W. Koon, and B. Ozyilmaz, "Enhanced spin-orbit coupling in dilute fluorinated graphene," *2D Materials*, vol. 2, no. 4, p. 044009, 2015.

[199] A. Weisse, G. Wellein, A. Alvermann, and H. Fehske, "The kernel polynomial method," *Rev. Mod. Phys.*, vol. 78, pp. 275–306, Mar 2006.

[200] S. Roche and D. Mayou, "Conductivity of quasiperiodic systems: A numerical study," *Phys. Rev. Lett.*, vol. 79, pp. 2518–2521, Sep 1997.

[201] S. Roche, "Quantum transport by means of O(n) real-space methods," *Phys. Rev. B*, vol. 59, pp. 2284–2291, Jan 1999.

[202] A. Ferreira and E. R. Mucciolo, "Critical delocalization of chiral zero energy modes in graphene," *Phys. Rev. Lett.*, vol. 115, p. 106601, Aug 2015.

[203] F. Ortmann and S. Roche, "Splitting of the zero-energy landau level and universal dissipative conductivity at critical points in disordered graphene," *Phys. Rev. Lett.*, vol. 110, p. 086602, Feb 2013.

[204] F. Ortmann, N. Leconte, and S. Roche, "Efficient linear scaling approach for computing the kubo hall conductivity," *Phys. Rev. B*, vol. 91, p. 165117, Apr 2015.

[205] J. H. García, L. Covaci, and T. G. Rappoport, "Real-space calculation of the conductivity tensor for disordered topological matter," *Phys. Rev. Lett.*, vol. 114, p. 116602, Mar 2015.

[206] T. L. van den Berg, L. Raymond, and A. Verga, "Dynamical spin hall conductivity in a magnetic disordered system," *Phys. Rev. B*, vol. 84, p. 245210, Dec 2011.

[207] A. Dyrdał, V. K. Dugaev, and J. Barnaś, "Spin hall effect in a system of dirac fermions in the honeycomb lattice with intrinsic and rashba spin-orbit interaction," *Phys. Rev. B*, vol. 80, p. 155444, Oct 2009.

[208] B. K. Nikolić, L. P. Zârbo, and S. Souma, "Mesoscopic spin hall effect in multiprobe ballistic spin-orbit-coupled semiconductor bridges," *Phys. Rev. B*, vol. 72, p. 075361, Aug 2005.

[209] L. Sheng, D. N. Sheng, and C. S. Ting, "Spin-hall effect in two-dimensional electron systems with rashba spin-orbit coupling and disorder," *Phys. Rev. Lett.*, vol. 94, p. 016602, Jan 2005.

[210] B. K. Nikolić, L. P. Zârbo, and S. Souma, "Imaging mesoscopic spin hall flow: Spatial distribution of local spin currents and spin densities in and out of multiterminal spin-orbit coupled semiconductor nanostructures," *Phys. Rev. B*, vol. 73, p. 075303, Feb 2006.

[211] C. W. Groth, M. Wimmer, A. R. Akhmerov, and X. Waintal, "Kwant: a software package for quantum transport," *New Journal of Physics*, vol. 16, no. 6, p. 063065, 2014.

[212] K. Kazymyrenko and X. Waintal, "Knitting algorithm for calculating green functions in quantum systems," *Phys. Rev. B*, vol. 77, p. 115119, Mar 2008.

[213] M. Wimmer and K. Richter, "Optimal block-tridiagonalization of matrices for coherent charge transport," *Journal of Computational Physics*, vol. 228, no. 23, pp. 8548 – 8565, 2009.

[214] B. K. Nikolić, L. P. Zârbo, and S. Welack, "Transverse spin-orbit force in the spin hall effect in ballistic semiconductor wires," *Phys. Rev. B*, vol. 72, p. 075335, 2005.

[215] B. K. Nikolić and R. L. Dragomirova, "What can we learn about the dynamics of transported spins by measuring shot noise in spin-orbit-coupled nanostructures?," *Semiconductor Science and Technology*, vol. 24, no. 6, p. 064006, 2009.

[216] J. Tworzydło, B. Trauzettel, M. Titov, A. Rycerz, and C. W. J. Beenakker, "Sub-poissonian shot noise in graphene," *Phys. Rev. Lett.*, vol. 96, p. 246802, Jun 2006.

[217] P.-H. Chang, F. Mahfouzi, N. Nagaosa, and B. K. Nikolić, "Spin-seebeck effect on the surface of a topological insulator due to nonequilibrium spin-polarization

parallel to the direction of thermally driven electronic transport," *Phys. Rev. B*, vol. 89, p. 195418, May 2014.

[218] M. Titov, "Impurity-assisted tunneling in graphene," *EPL (Europhysics Letters)*, vol. 79, no. 1, p. 17004, 2007.

[219] J. H. Garcia and T. G. Rappoport, "Kubo-bastin approach for the spin hall conductivity of decorated graphene," *2D Materials*, vol. 3, no. 2, p. 024007, 2016.

[220] A. Ferreira, "private communication.".

[221] L. Sheng, D. N. Sheng, and C. S. Ting, "Spin-hall effect in two-dimensional electron systems with rashba spin-orbit coupling and disorder," *Phys. Rev. Lett.*, vol. 94, p. 016602, Jan 2005.

[222] D. Xiao, W. Yao, and Q. Niu, "Valley-contrasting physics in graphene: Magnetic moment and topological transport," *Phys. Rev. Lett.*, vol. 99, p. 236809, Dec 2007.

[223] Y. D. Lensky, J. C. W. Song, P. Samutpraphoot, and L. S. Levitov, "Topological valley currents in gapped dirac materials," *Phys. Rev. Lett.*, vol. 114, p. 256601, Jun 2015.

[224] J. C. W. Song, P. Samutpraphoot, and L. S. Levitov, "Topological bloch bands in graphene superlattices," *Proceedings of the National Academy of Sciences*, vol. 112, no. 35, pp. 10879–10883, 2015.

[225] M. Beconcini, F. Taddei, and M. Polini, "Nonlocal topological valley transport at large valley hall angles," *Phys. Rev. B*, vol. 94, p. 121408, Sep 2016.

[226] D. A. Abanin, S. V. Morozov, L. A. Ponomarenko, R. V. Gorbachev, A. S. Mayorov, M. I. Katsnelson, K. Watanabe, T. Taniguchi, K. S. Novoselov, L. S. Levitov, and A. K. Geim, "Giant nonlocality near the dirac point in graphene," *Science*, vol. 332, p. 328, 2011.

[227] J. Renard, M. Studer, and J. A. Folk, "Origins of nonlocality near the neutrality point in graphene," *Phys. Rev. Lett.*, vol. 112, p. 116601, Mar 2014.

[228] P. Wei, S. Lee, F. Lemaitre, L. Pinel, D. Cutaia, W. Cha, F. Katmis, Y. Zhu, D. Heiman, J. Hone, J. S. Moodera, and C.-T. Chen, "Strong interfacial exchange field in the graphene/eus heterostructure," *Nat Mater*, vol. advance online publication, pp. –, Mar. 2016.

[229] D. Van Tuan, J. M. Marmolejo-Tejada, X. Waintal, B. K. Nikolić, S. O. Valenzuela, and S. Roche, "Spin hall effect and origins of nonlocal resistance in adatom-decorated graphene," *Phys. Rev. Lett.*, vol. 117, p. 176602, Oct 2016.

[230] G. Giovannetti, P. A. Khomyakov, G. Brocks, P. J. Kelly, and J. van den Brink, "Substrate-induced band gap in graphene on hexagonal boron nitride: *Ab initio* density functional calculations," *Phys. Rev. B*, vol. 76, p. 073103, Aug 2007.

[231] T. Ando, "Theory of valley hall conductivity in graphene with gap," *Journal of the Physical Society of Japan*, vol. 84, no. 11, p. 114705, 2015.

[232] S. Adam, P. W. Brouwer, and S. Das Sarma, "Crossover from quantum to boltzmann transport in graphene," *Phys. Rev. B*, vol. 79, p. 201404, May 2009.

[233] J. W. Kłos and I. V. Zozoulenko, "Effect of short- and long-range scattering on the conductivity of graphene: Boltzmann approach vs tight-binding calculations," *Phys. Rev. B*, vol. 82, p. 081414, Aug 2010.

[234] G. Kirczenow, "Valley currents and nonlocal resistances of graphene nanostructures with broken inversion symmetry from the perspective of scattering theory," *Phys. Rev. B*, vol. 92, p. 125425, Sep 2015.

[235] H. U. Baranger and A. D. Stone, "Electrical linear-response theory in an arbitrary magnetic field: A new fermi-surface formation," *Phys. Rev. B*, vol. 40, p. 8169, 1989.

[236] P. L. McEuen, A. Szafer, C. A. Richter, B. W. Alphenaar, J. K. Jain, A. D. Stone, R. G. Wheeler, and R. N. Sacks, "New resistivity for high-mobility quantum hall conductors," *Phys. Rev. Lett.*, vol. 64, pp. 2062–2065, Apr 1990.

[237] A. Roth, C. Brüne, H. Buhmann, L. W. Molenkamp, J. Maciejko, X.-L. Qi, and S.-C. Zhang, "Nonlocal edge state transport in the quantum spin hall state," *Science*, vol. 325, p. 294, 2009.

[238] M. J. Zhu, A. V. Kretinin, M. D. Thompson, D. A. Bandurin, S. Hu, G. L. Yu, J. Birkbeck, A. Mishchenko, I. J. Vera-Marun, K. Watanabe, T. Taniguchi, M. Polini, J. R. Prance, K. S. Novoselov, A. K. Geim, and M. Ben Shalom, "Edge currents shunt the insulating bulk in gapped graphene," *Nature Communications*, vol. 8, p. 14552, Feb. 2017.

[239] W. Yao, S. A. Yang, and Q. Niu, "Edge states in graphene: From gapped flatband to gapless chiral modes," *Phys. Rev. Lett.*, vol. 102, p. 096801, Mar 2009.

[240] Y.-T. Zhang, Q. feng Sun, and X. C. Xie, "The effect of disorder on the valley-dependent transport in zigzag graphene nanoribbons," *Journal of Applied Physics*, vol. 109, no. 12, p. 123718, 2011.

[241] Y. Ren, Z. Qiao, and Q. Niu, "Topological phases in two-dimensional materials: a review," *Reports on Progress in Physics*, vol. 79, no. 6, p. 066501, 2016.

[242] M. Sui, G. Chen, L. Ma, W.-Y. Shan, D. Tian, K. Watanabe, T. Taniguchi, X. Jin, W. Yao, D. Xiao, and Y. Zhang, "Gate-tunable topological valley transport in bilayer graphene," *Nat Phys*, vol. 11, pp. 1027–1031, Dec. 2015.

[243] Y. Shimazaki, M. Yamamoto, I. V. Borzenets, K. Watanabe, T. Taniguchi, and S. Tarucha, "Generation and detection of pure valley current by electrically induced berry curvature in bilayer graphene," *Nat Phys*, vol. 11, pp. 1032–1036, Dec. 2015.

[244] X. Jia, M. Hofmann, V. Meunier, B. G. Sumpter, J. Campos-Delgado, J. Manuel, R.-H. Hyungbin, S. Ya-Ping, H. A. Reina, J. Kong, M. Terrones, and M. S. Dresselhaus, "Controlled formation of sharp zigzag and armchair edges in graphitic nanoribbons," *Science*, vol. 323, p. 1701, 2009.

[245] K. K. Saha, M. Drndić, and B. K. Nikolić, "Dna base-specific modulation of microampere transverse edge currents through a metallic graphene nanoribbon with a nanopore," *Nano Lett.*, vol. 12, p. 50, 2012.

[246] P.-H. Chang and B. K. Nikolić, "Edge currents and nanopore arrays in zigzag and chiral graphene nanoribbons as a route toward high-zt thermoelectrics," *Phys. Rev. B*, vol. 86, p. 041406(R), Jul 2012.

[247] F. Ortmann, A. Cresti, G. Montambaux, and S. Roche, "Magnetoresistance in disordered graphene: The role of pseudospin and dimensionality effects unraveled," *EPL (Europhysics Letters)*, vol. 94, no. 4, p. 47006, 2011.

[248] `http://kwant-project.org/`.

[249] K. K. Saha and B. K. Nikolić, "Negative differential resistance in graphene-nanoribbon/carbon-nanotube crossbars: A first-principles multiterminal quantum transport study," *J. Comp. Electron.*, vol. 12, p. 542, 2013.

[250] T. Christen and M. Büttiker, "Gauge-invariant nonlinear electric transport in mesoscopic conductors," *Europhys. Lett.*, vol. 35, no. 7, pp. 523–528, 1996.

[251] A. Bastin, C. Lewiner, O. Betbeder-matibet, and P. Nozieres, "Quantum oscillations of the hall effect of a fermion gas with random impurity scattering," *Journal of Physics and Chemistry of Solids*, vol. 32, no. 8, pp. 1811 – 1824, 1971.

[252] "Atomistix toolkit (atk) 2016.4, http://www.quantumwise.com."

[253] "Openmx 3.8, http://www.openmx-square.org/."

[254] T. Ozaki, "Variationally optimized atomic orbitals for large-scale electronic structures," *Phys. Rev. B*, vol. 67, p. 155108, Apr 2003.

[255] M. Brandbyge, J.-L. Mozos, P. Ordejón, J. Taylor, and K. Stokbro, "Density-functional method for nonequilibrium electron transport," *Physical Review B*, vol. 65, p. 165401, Apr. 2002.

[256] T. Ozaki and H. Kino, "Numerical atomic basis orbitals from h to kr," *Phys. Rev. B*, vol. 69, p. 195113, May 2004.

[257] L. A. Agapito, M. Fornari, D. Ceresoli, A. Ferretti, S. Curtarolo, and M. B. Nardelli, "Accurate tight-binding hamiltonians for two-dimensional and layered materials," *Phys. Rev. B*, vol. 93, p. 125137, Mar 2016.

[258] M. Schlipf and F. Gygi, "Optimization algorithm for the generation of oncv pseudopotentials," *Computer Physics Communications*, vol. 196, p. 36, 2015.

[259] T. B. Boykin, M. Luisier, G. Klimeck, X. Jiang, N. Kharche, Y. Zhou, and S. K. Nayak, "Accurate six-band nearest-neighbor tight-binding model for the pi -bands of bulk graphene and graphene nanoribbons," *Journal of Applied Physics*, vol. 109, no. 10, p. 104304, 2011.

[260] L. Brey and H. A. Fertig, "Electronic states of graphene nanoribbons studied with the dirac equation," *Physical Review B*, vol. 73, p. 235411, June 2006.

[261] L. P. Zârbo and B. K. Nikolić, "Spatial distribution of local currents of massless dirac fermions in quantum transport through graphene nanoribbons," *Europhysics Letters*, vol. 80, no. 4, p. 47001, 2007.

[262] M. J. Zhu, A. V. Kretinin, M. D. Thompson, D. A. Bandurin, S. Hu, G. L. Yu, J. Birkbeck, A. Mishchenko, I. J. Vera-Marun, K. Watanabe, T. Taniguchi, M. Polini, J. R. Prance, K. S. Novoselov, A. K. Geim, and M. Ben Shalom, "Edge currents shunt the insulating bulk in gapped graphene," *Nature Communications*, vol. 8, p. 14552, Feb. 2017.

[263] N. Marzari, A. A. Mostofi, J. R. Yates, I. Souza, and D. Vanderbilt, "Maximally localized wannier functions: Theory and applications," *Rev. Mod. Phys.*, vol. 84, pp. 1419–1475, Oct 2012.

[264] G. Kresse and J. Hafner, "*Ab initio* molecular dynamics for liquid metals," *Phys. Rev. B*, vol. 47, pp. 558–561, Jan 1993.

[265] G. Kresse and J. FurthmÃŒller, "Efficiency of ab-initio total energy calculations for metals and semiconductors using a plane-wave basis set," *Computational Materials Science*, vol. 6, no. 1, pp. 15 – 50, 1996.

[266] A. A. Mostofi, J. R. Yates, Y.-S. Lee, I. Souza, D. Vanderbilt, and N. Marzari, "wannier90: A tool for obtaining maximally-localised wannier functions," *Computer Physics Communications*, vol. 178, no. 9, pp. 685 – 699, 2008.

[267] P. E. Blöchl, "Projector augmented-wave method," *Phys. Rev. B*, vol. 50, pp. 17953–17979, Dec 1994.

[268] G. Kresse and D. Joubert, "From ultrasoft pseudopotentials to the projector augmented-wave method," *Phys. Rev. B*, vol. 59, pp. 1758–1775, Jan 1999.

[269] A. Rycerz, J. Tworzydło, and C. W. J. Beenakker, "Valley filter and valley valve in graphene," *Nature Physics*, vol. 3, p. 172, Aug. 2007.

[270] P.-H. Chang, M. S. Bahramy, N. Nagaosa, and B. K. Nikolić, "Giant thermoelectric effect in graphene-based topological insulators with heavy adatoms and nanopores," *Nano Letters*, vol. 14, no. 7, pp. 3779–3784, 2014. PMID: 24932511.

[271] X.-L. Sheng and B. K. Nikolić, "Monolayer of the $5d$ transition metal trichloride $oscl_3$: A playground for two-dimensional magnetism, room-temperature quantum anomalous hall effect, and topological phase transitions," *Phys. Rev. B*, vol. 95, p. 201402, May 2017.

[272] J. Li, I. Martin, M. Buttiker, and A. F. Morpurgo, "Topological origin of subgap conductance in insulating bilayer graphene," *Nat Phys*, vol. 7, no. 1, pp. 38–42, 2011.

[273] D. Pesin and A. H. MacDonald, "Spintronics and pseudospintronics in graphene and topological insulators," *Nat Mater*, vol. 11, no. 5, pp. 409–416, 2012.

[274] F. Mahfouzi, N. Nagaosa, and B. K. Nikolić, "Spin-to-charge conversion in lateral and vertical topological-insulator/ferromagnet heterostructures with microwave-driven precessing magnetization," *Phys. Rev. B*, vol. 90, p. 115432, Sep 2014.

[275] F. Mahfouzi, B. K. Nikolić, and N. Kioussis, "Antidamping spin-orbit torque driven by spin-flip reflection mechanism on the surface of a topological insulator: A time-dependent nonequilibrium green function approach," *Phys. Rev. B*, vol. 93, p. 115419, Mar 2016.

[276] A. Bansil, H. Lin, and T. Das, "Colloquium: Topological band theory," *Rev. Mod. Phys.*, vol. 88, p. 021004, Jun 2016.

[277] W. Luo and X.-L. Qi, "Massive dirac surface states in topological insulator/magnetic insulator heterostructures," *Phys. Rev. B*, vol. 87, p. 085431, Feb 2013.

[278] A. T. Lee, M. J. Han, and K. Park, "Magnetic proximity effect and spin-orbital texture at the bi_2se_3/EuS interface," *Phys. Rev. B*, vol. 90, p. 155103, Oct 2014.

[279] E. Zhao, C. Zhang, and M. Lababidi, "Mott scattering at the interface between a metal and a topological insulator," *Phys. Rev. B*, vol. 82, p. 205331, Nov 2010.

[280] J. A. Hutasoit and T. D. Stanescu, "Induced spin texture in semiconductor/topological insulator heterostructures," *Phys. Rev. B*, vol. 84, p. 085103, Aug 2011.

[281] A. A. Soluyanov, D. Gresch, Z. Wang, Q. Wu, M. Troyer, X. Dai, and B. A. Bernevig, "Type-ii weyl semimetals," *Nature*, vol. 527, no. 7579, pp. 495–498, 2015.

[282] T. Shoman, A. Takayama, T. Sato, S. Souma, T. Takahashi, T. Oguchi, K. Segawa, and Y. Ando, "Topological proximity effect in a topological insulator hybrid," *Nature Communications*, vol. 6, pp. 6547 EP –, Mar 2015. Article.

[283] C. D. Spataru and F. m. c. Léonard, "Fermi-level pinning, charge transfer, and relaxation of spin-momentum locking at metal contacts to topological insulators," *Phys. Rev. B*, vol. 90, p. 085115, Aug 2014.

[284] J. Zhang, J. P. Velev, X. Dang, and E. Y. Tsymbal, "Band structure and spin texture of $bi_2se_3 3d$ ferromagnetic metal interface," *Phys. Rev. B*, vol. 94, p. 014435, Jul 2016.

[285] J. Velev and W. Butler, "On the equivalence of different techniques for evaluating the green function for a semi-infinite system using a localized basis," *Journal of Physics: Condensed Matter*, vol. 16, no. 21, p. R637, 2004.

[286] I. Rungger and S. Sanvito, "Algorithm for the construction of self-energies for electronic transport calculations based on singularity elimination and singular value decomposition," *Phys. Rev. B*, vol. 78, p. 035407, Jul 2008.

[287] H. H. B. Sørensen, P. C. Hansen, D. E. Petersen, S. Skelboe, and K. Stokbro, "Krylov subspace method for evaluating the self-energy matrices in electron transport calculations," *Phys. Rev. B*, vol. 77, p. 155301, Apr 2008.

[288] J. Kim, J. Sinha, M. Hayashi, M. Yamanouchi, S. Fukami, T. Suzuki, S. Mitani, and H. Ohno, "Layer thickness dependence of the current-induced effective field vector in ta|cofeb|mgo," *Nat Mater*, vol. 12, no. 3, pp. 240–245, 2013.

[289] N. Nagaosa, J. Sinova, S. Onoda, A. H. MacDonald, and N. P. Ong, "Anomalous hall effect," *Rev. Mod. Phys.*, vol. 82, pp. 1539–1592, May 2010.

[290] P. M. Haney, H.-W. Lee, K.-J. Lee, A. Manchon, and M. D. Stiles, "Current induced torques and interfacial spin-orbit coupling: Semiclassical modeling," *Phys. Rev. B*, vol. 87, p. 174411, May 2013.

[291] J. G. Checkelsky, J. Ye, Y. Onose, Y. Iwasa, and Y. Tokura, "Dirac-fermion-mediated ferromagnetism in a topological insulator," *Nat Phys*, vol. 8, no. 10, pp. 729–733, 2012.

[292] A. N. Chantis, K. D. Belashchenko, E. Y. Tsymbal, and M. van Schilfgaarde, "Tunneling anisotropic magnetoresistance driven by resonant surface states: First-principles calculations on an fe(001) surface," *Phys. Rev. Lett.*, vol. 98, p. 046601, Jan 2007.

[293] M. S. Bahramy, P. D. C. King, A. de la Torre, J. Chang, M. Shi, L. Patthey, G. Balakrishnan, P. Hofmann, R. Arita, N. Nagaosa, and F. Baumberger, "Emergent quantum confinement at topological insulator surfaces," *Nature Communications*, vol. 3, pp. 1159 EP –, Oct 2012. Article.

[294] S. Emori, T. Nan, A. M. Belkessam, X. Wang, A. D. Matyushov, C. J. Babroski, Y. Gao, H. Lin, and N. X. Sun, "Interfacial spin-orbit torque without bulk spin-orbit coupling," *Phys. Rev. B*, vol. 93, p. 180402, May 2016.

[295] B. G. Park, J. Wunderlich, D. A. Williams, S. J. Joo, K. Y. Jung, K. H. Shin, K. Olejník, A. B. Shick, and T. Jungwirth, "Tunneling anisotropic magnetoresistance in multilayer-(Co/Pt)/alo$_x$/Pt structures," *Phys. Rev. Lett.*, vol. 100, p. 087204, Feb 2008.

[296] A. Matos-Abiague and J. Fabian, "Anisotropic tunneling magnetoresistance and tunneling anisotropic magnetoresistance: Spin-orbit coupling in magnetic tunnel junctions," *Phys. Rev. B*, vol. 79, p. 155303, Apr 2009.

[297] "Virtual nanolab (vnl) 2016.4, http://www.quantumwise.com."

[298] P. Lazić "Cellmatch: Combining two unit cells into a common supercell with minimal strain," *Computer Physics Communications*, vol. 197, pp. 324 – 334, 2015.

[299] M. Dion, H. Rydberg, E. Schröder, D. C. Langreth, and B. I. Lundqvist, "Van der waals density functional for general geometries," *Phys. Rev. Lett.*, vol. 92, p. 246401, Jun 2004.

[300] F. Mittendorfer, A. Garhofer, J. Redinger, J. Klimeš, J. Harl, and G. Kresse, "Graphene on ni(111): Strong interaction and weak adsorption," *Phys. Rev. B*, vol. 84, p. 201401, Nov 2011.

[301] H. Vázquez, Y. J. Dappe, J. Ortega, and F. Flores, "Energy level alignment at metal/organic semiconductor interfaces: "pillow" effect, induced density of interface states, and charge neutrality level," *The Journal of Chemical Physics*, vol. 126, no. 14, p. 144703, 2007.